2011

Flaw detection in Multi-layer, Multi-material Composites by Resonance Imaging: utilizing Air-coupled Ultrasonics and Finite Element Modeling

Richard Livings
Iowa State University

Flaw detection in multi-layer, multi-material composites by resonance imaging: Utilizing Air-coupled Ultrasonics and Finite Element Modeling

by

Richard Andrew Livings

A thesis submitted to the graduate faculty

in partial fulfillment of the requirements for the degree of

MASTER OF SCIENCE

Major: Aerospace Engineering

Program of Study Committee:
Vinay Dayal, Major Professor
Dave K. Hsu
Dan J. Barnard
Thomas J. Rudolphi

Iowa State University

Ames, Iowa

2011

TABLE OF CONTENTS

LIST OF FIGURES

LIST OF TABLES

ABSTRACT

Ceramic tiles are the main ingredient of a multi-material, multi-layered composite being considered for the modernization of tank armors. The high stiffness, low attenuation, and precise dimensions of these uniform tiles make them remarkable resonators when driven to vibrate. Defects in the tile, during manufacture or after usage, are expected to change the resonance frequencies and resonance images of the tile. The comparison of the resonance frequencies and resonance images of a pristine tile/lay-up to a defective tile/lay-up will thus be a quantitative damage metric. By examining the vibrational behavior of these tiles and the composite lay-up with Finite Element Modeling and analytical plate vibration equations, the development of a new Nondestructive Evaluation technique is possible. This study examines the development of the Air-Coupled Ultrasonic Resonance Imaging technique as applied to a hexagonal ceramic tile and a multi-material, multi-layered composite.

CHAPTER 1.
THESIS INTRODUCTION

Multi-layer, multi-material composites with ceramic tiles at their heart are being considered for next generation armors. The multiple layers of different materials, including materials with high attenuation, make traditional Nondestructive Evaluation (NDE) difficult. Due to their brittle nature and high fracture energy the ceramic tiles at the center of these composites provide the main ballistic resistance of the armor. The mechanical and geometric properties of the tiles also provide another difference from the other materials in the lay-up, namely that the high stiffness, low attenuation, and precise dimensions of these uniform tiles make them remarkable resonators when driven to vibrate. Any defects in the tile, during manufacture or after usage, are expected to change the resonance frequencies and resonance images of the tile. Likewise, any defects in the lay-up will affect the received signal. Thus the comparison of the resonance frequencies and resonance images of a pristine tile/lay-up to a defective tile/lay-up will be a quantitative damage metric. The purpose of this study was to develop the Air-Coupled Ultrasonic Resonance Imaging (ACURI) technique. The development of this new technique was performed by examining the vibrational behavior of the ceramic tiles and the composite lay-up with Air-Coupled Ultrasonic Testing (ACUT), analytical plate vibration equations, and Finite Element Modeling (FEM).

The second chapter of this thesis describes all of the ACUT analysis performed on the ceramic tiles and the lay-ups in the process of developing this new ACURI technique. All testing setups and their results are presented along with the conclusions drawn from the results.

The third chapter presents the development of an analytical equation to describe the transverse vibration of a hexagonal plate and its implementation. The results from the

implementation of this equation are compared with numerical (FEM) and experimental (ACURI) results and the validity of the equation is examined.

The fourth chapter of this thesis presents and describes all of the Finite Element Modeling performed on the ceramic tile and the composite lay-up. The results from the FEM cannot be completely presented due to the shear amount of the images and data, however, any and all significant data, will be presented and discussed. This chapter also examines the accuracy of using symmetric sections to reduce problem size/complexity and computation time.

CHAPTER 2.
AIR-COUPLED ULTRASONIC TESTING

Introduction

Ultrasonic testing has long been used in Nondestructive Evaluation (NDE) for flaw detection and characterization. Most of the ultrasonic testing techniques have used water or some other liquid couplant due to their relatively low attenuation. This allows for a high amount of energy to be transferred into a sample. The advent of composites and other couplant sensitive materials, as well as their subsequent integration into many industries (such as the aerospace industry) necessitated the development and use of non-contact NDE methods.

Acoustic non-contact methods have historically been very difficult to use due to the enormous loss of energy at the air-solid interface and the inefficient transfer of acoustic energy through air. Over the last two decades, more efficient transducers were developed for the generation and reception of air-borne ultrasound, thus enabling the non-contact, non-contaminating inspection of composite laminates and honeycomb structures widely used in the aerospace industry. [1.13]

Since its inception, Air-coupled Ultrasonic Testing (ACUT) has been treated as a low frequency version of water-coupled ultrasonics, and its development and uses are described in the references [1.3-1.19]. Because of this treatment almost no techniques have been developed that utilize the strengths of ACUT. Trying to use the techniques developed for Water-Coupled inspection with ACUT has provided less than spectacular results. This chapter explores a new testing method for ACUT that utilizes resonance imaging.

Literature Review

It is an undeniable fact that some materials, especially composites structures, are couplant sensitive and require some sort of non-contact inspection systems. The 1995 paper by Grandia and Fortunko [1.1] was one of the first to describe the capabilities of a commercially available air-coupled system and discus potential applications. Bhardwaj further describes the air-coupled systems (transducers and analyzers) in his 2001 paper [1.2]. The development of several different aspects (different techniques, limitations, and capabilities) of this nascent yet maturing branch of NDE is chronicled in the references [1.3-1.19].

Migliori and Darling [1.20] were the first to explore resonant ultrasound spectroscopy in 1995 to determine the natural modes of a given sample. This was done by shaking the sample ultrasonically in short bursts then recording the amplitude of the ring-down vibration of the sample. Cabrera et al [1.21] in 2003 used this technique to detect cracks and other flaws in samples. They demonstrated that a defect in a sample will change the amplitude and/or frequency of the natural modes of the sample.

Material Description

A new composite material is being considered for the modernization of tank armors. This new composite is composed of several layers of different materials and will thus be referred to as a multi-layer, multi-material composite. The overall lay-up is depicted in Fig.1.1. The layers from the bottom up are: IM7 carbon-fiber/epoxy (graphite), hexagonal Silicon Carbide (SiC) tiles, IM7 carbon-fiber/epoxy, rubber, and glass-fiber/epoxy (S2 glass).

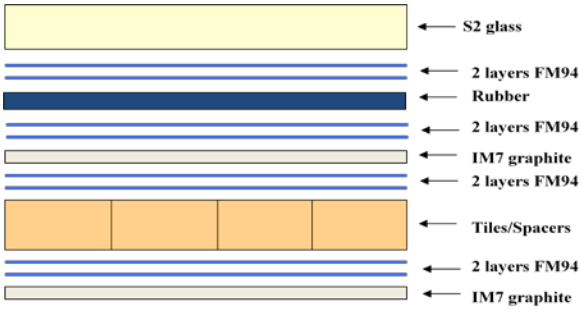

FIGURE 1.1. Depiction of the materials and layers of the Multi-layer, Multi-material Composite.

The layers are glued together with two sheets of FM94 film adhesive. Each layer is composed of a different material from its neighboring layers, and each material has very different mechanical and acoustical properties.

Several samples of this material and its constituent parts were provided for this study. Multiple SiC tiles, both hexagon and square, four lay-ups, three full lay-ups with embedded defects and one graphite-ceramic-graphic (GCG) lay-up, and small samples of the graphite, rubber, and glass layers were provided. The SiC material has an elastic modulus of 428.28 GPa, a Poison's ratio of 0.166, and a density of 3058.4 Kg/m^3.

Problems with Traditional Methods

When it comes to traditional NDE Ultrasonic Testing (UT), such as through transmission inspection and pulse-echo inspection, this type of material offers some difficulties, namely high attenuation and impedance mismatches at the layer interfaces.

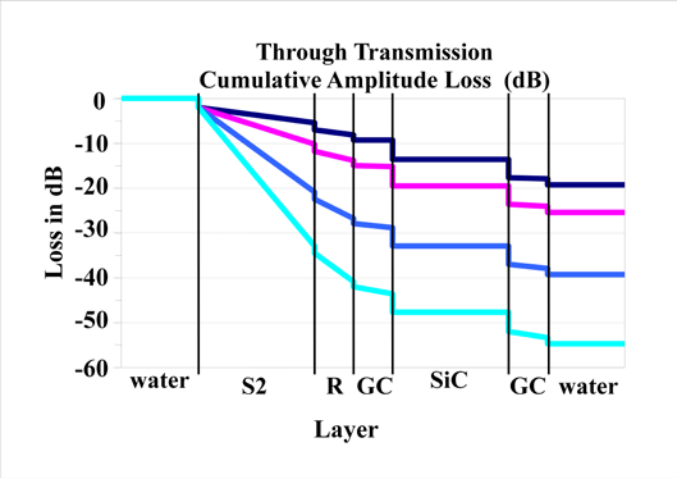

FIGURE 1.2. Plot of the approximate signal losses in dB based on the reflection coefficients for each interface and the transmission coefficients for each layer. The thickness of each layer is proprietary and hence is not shown in the fgure. Courtesy of Frank Margatan, CNDE, Iowa State University.

Fig. 1.2 shows a plot of the approximate signal loss in decibels (dB) as a function of thickness calculated as the signal passes through the material. The signal loss is calculated very simply by using material properties obtained from Water-Coupled UT (immersion scanning), which dictate the reflection coefficients of each layer interface and the transmission coefficients through each layer. It can be seen from the figure that the signal loss increases drastically with increase in frequency. It is also noteworthy to mention that Air-Coupled UT operates below the frequencies plotted and Water-Coupled UT typically operates above.

The results of an immersion pulse-echo inspection attempted on a multi-layer, multi-material composite is shown in Fig. 1.3. The signal is very convoluted due to all of the layers which make it difficult to analyze. When the ultrasonic wave strikes the interface between layer 1 and layer 2, part of the wave is reflected back into layer 1 and part of the wave is transmitted into layer 2. The wave that was reflected back into layer 1 strikes the interface between layer 1 and the coupling medium and part of the wave is reflected while the other part is transmitted. This means that part of the original reflected wave is reflected back into the material. This

reflected wave just keeps bouncing between the two interfaces and transmits part of its energy each time it strikes an interface. Meanwhile the wave transmitted into layer 2 strikes the interface between layer 2 and layer 3, again there is reflection and transmission and the process of the wave bouncing between the two interfaces of layer 2 is initiated. This happens in each and every layer and each transmission at each interface starts another series of signals bouncing. The reflecting waves in each layer yield a very convoluted signal and the result is Fig. 1.3.

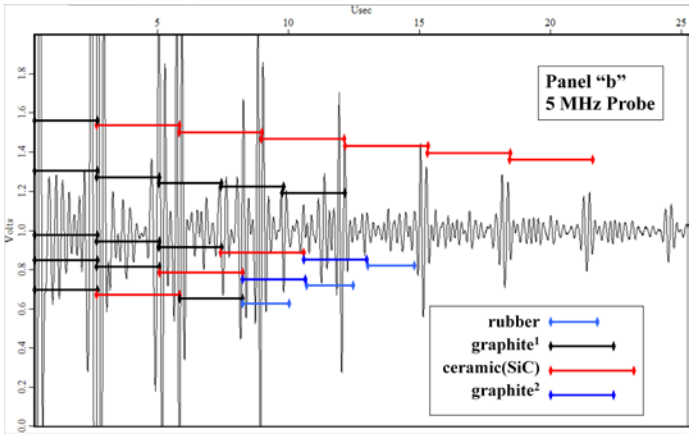

FIGURE 1.3. Immersion UT pulse-echo inspection plot of voltage versus time.

Traditional immersion scans suffer drastic signal loss in through transmission inspections and are forced to operate at the very low end of their operating frequencies. In pulse-echo inspections, the signal is so complicated that no useful information can be easily extracted. These facts, combined with the necessity of a water tank large enough to contain the sample, make the immersion scan difficult to perform and an unviable option as a fieldable NDE technique. With that in mind, and the fact that Fig. 1.2 indicates the operating frequencies of ACUT experience much less signal loss through the lay-up, Air-Coupled Ultrasound is the obvious choice for continued ultrasonic inspection of this material.

Initial ACUT Inspection

The preliminary Air-Coupled inspection of one of the samples yielded some surprising results. Fig. 1.4 shows two separate through scans of the same sample at the frequencies of 120 kHz and 225 kHz. The most noticeable things from these scans are the very prominent hexagon shapes and the very bright dots that form, what has been termed to be, “snowflake” patterns centered on the hexagon shapes. There is only one component of the lay-up that could account for the presence of these hexagon shapes in the above scans. These hexagonal patterns are the same size, shape, location, and orientation as the SiC tiles in the center of the lay-up. The snowflake patterns are centered on the hexagon shapes and appear to line up with the hexagons as if the hexagon shape and the snowflake image were part of the same pattern. Because of this, it is safe to assume the hexagon and the snowflake patterns are caused by the vibration of the ceramic tiles.

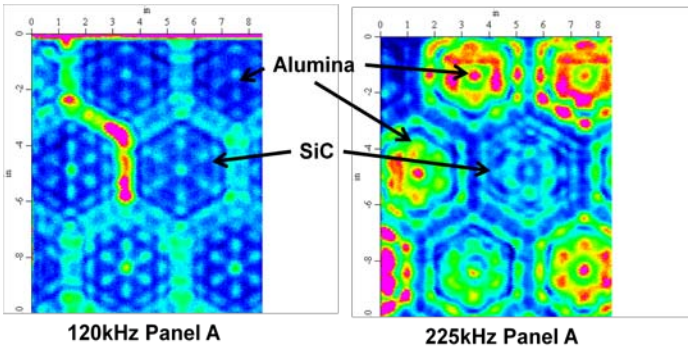

FIGURE 1.4. Preliminary through scans of a sample layup at the frequencies of 120 kHz and 225 kHz. The images are produced by taking the amplitude maximum of the received waveform over the entire time gate.

If it is true that the snowflake patterns are caused by the vibration of the ceramic tiles, then they must be resonance patterns of the tiles. If they are resonance patterns of the tiles, then they should vary with both material and frequency. A closer inspection of the images in Fig. 1.4 shows that the snowflake patterns for the 120 kHz scan are different for the different

materials. The SiC tile has more of a “spoke-like” pattern while the alumina tiles have more of a separated dot pattern, which is significantly different. When comparing the 120 kHz scan image to the 225 kHz scan image (the SiC tile specifically), it can be seen that the pattern is significantly different at the different frequencies. Since the snowflake patterns vary with both material and frequency it is safe to assume that the results from the preliminary through scans are due to the resonance of the ceramic tiles embedded in the lay-up.

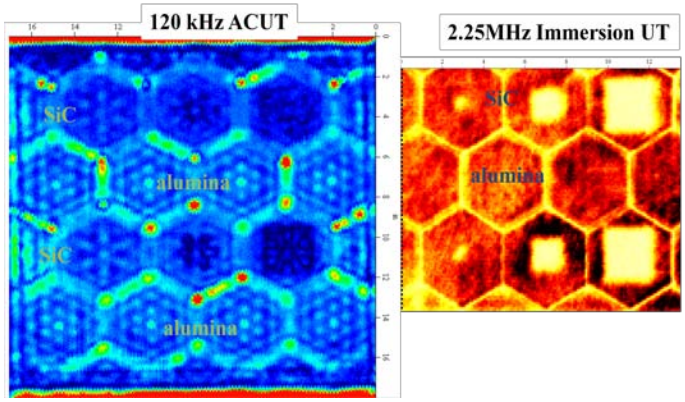

FIGURE 1.5. Comparison of preliminary through scan of a sample layup with defects at a frequency of 120 kHz with an immersion scan at a frequency of 2.25 MHz. The Air-Coupled image is produced by taking the amplitude maximum of the received waveform over the entire time gate.

In a quick comparison of a preliminary through scan using Air-Coupled UT at a frequency of 120 kHz and an Immersion UT through scan at a frequency of 2.25 MHz (Fig. 1.5) it is obvious that the six flaws are more easily detected with the Immersion scan. The differences in the tile materials, however, could not be detected with Immersion UT. This shows that the different inspection methods have different strengths and give different information.

SiC Tile Characterization

The first step in developing an NDE technique is to characterize the SiC tile. Two different types of scans were performed on the SiC tile in order to better understand the behavior of the tile and to search for several strong resonances, their frequencies, and their visual patterns.

The first technique used to characterize the tiles is to perform a through transmission scan on the tile, where both the transmitter and receiver are scanning. This is exactly the same type of inspection used in the full lay-ups. Fig 1.6 shows a comparison between a through transmission scan of the bare SiC tile and a full lay-up with no known defect. In these images blue is low amplitude while red is high amplitude. Since the plate is vibrating the high and low amplitude regions will alternate in sign, and hence color, in a cyclical manor. Because of this the colors are interchangeable. This is true for all of the ACUT images in this study. As can be seen, the resonance patterns match quite well when damping from the other layers is taken into account (and the colors reversed).

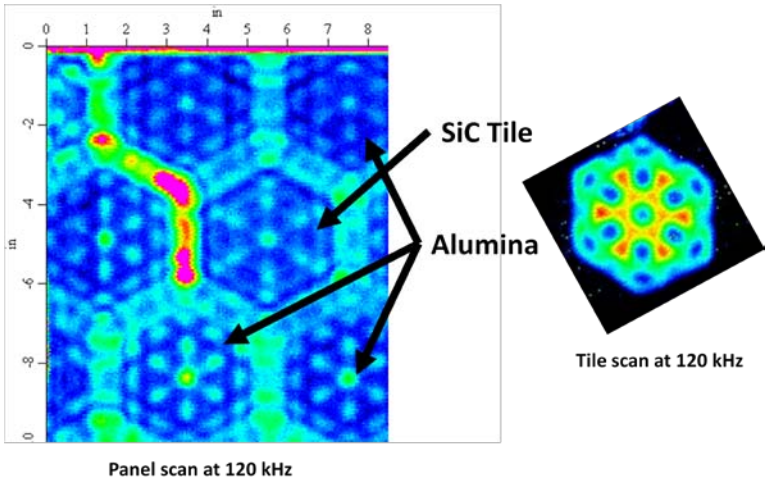

FIGURE 1.6. Comparison of through transmission scans of a layup with no known defects and a bare SiC tile at 120 kHz. The images are produced by taking the amplitude maximum of the received waveform over the entire time gate.

The second technique used to characterize the SiC tiles uses a constant frequency sine wave (CW) signal, which was impinged on the bare tile at low voltage and hence low amplitude. The amplitude of the received wave was stored, then the frequency was increased by a specified amount, df, and the whole process was repeated. This technique identifies all of the natural frequencies of the tile, and is very similar to the method used by Cabrera et al [1.20].

Fig. 1.7 and 1.8 show the results from this type of scan. The blue plot is the transducer amplitude through air at each frequency. The red plot is the amplitude of the received signal from the tile. In this case the transmitter is impinging on the center of the tile and the receiver is far enough away from the tile to hopefully capture most of the surface.

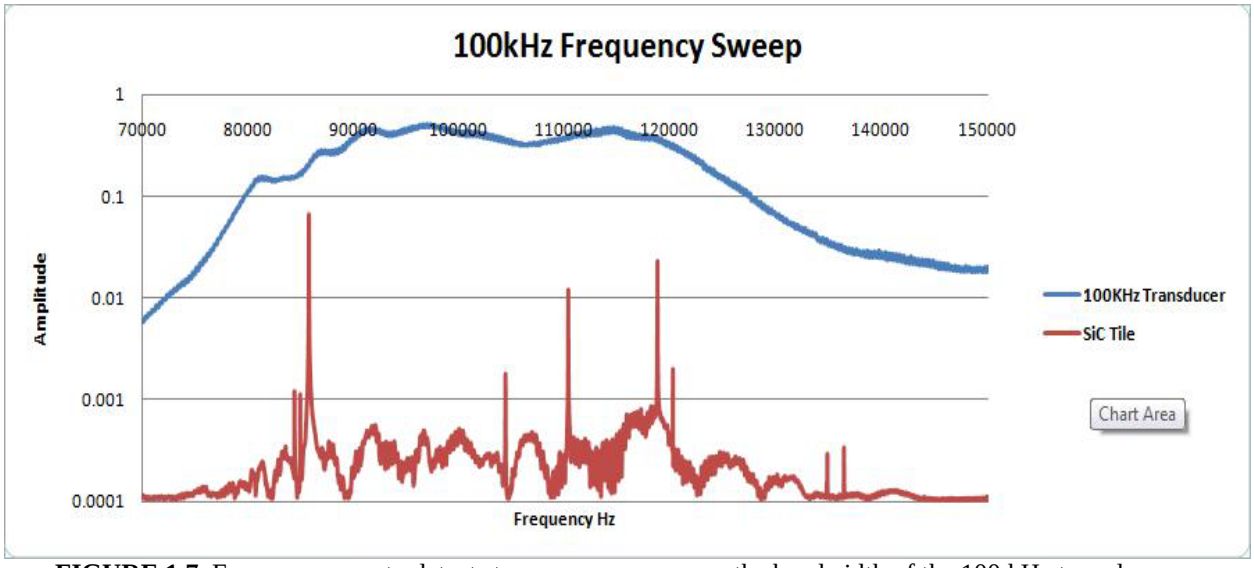

FIGURE 1.7. Frequency scan to detect strong resonances over the bandwidth of the 100 kHz transducer.

The 100 kHz plot shows quite a few high amplitude resonances. These high amplitude resonances could be used to detect flaws after the resonance images for each resonant peak are determined. It is interesting to note here that the quality factors (Q value), which measure how well a system oscillates, for these scans are in excess of 10,000. The highest Q value observed

is ~47,000. This means that these SiC tiles are remarkable resonators when driven to vibrate, and explains why the resonance patterns can be seen through the entire lay-up.

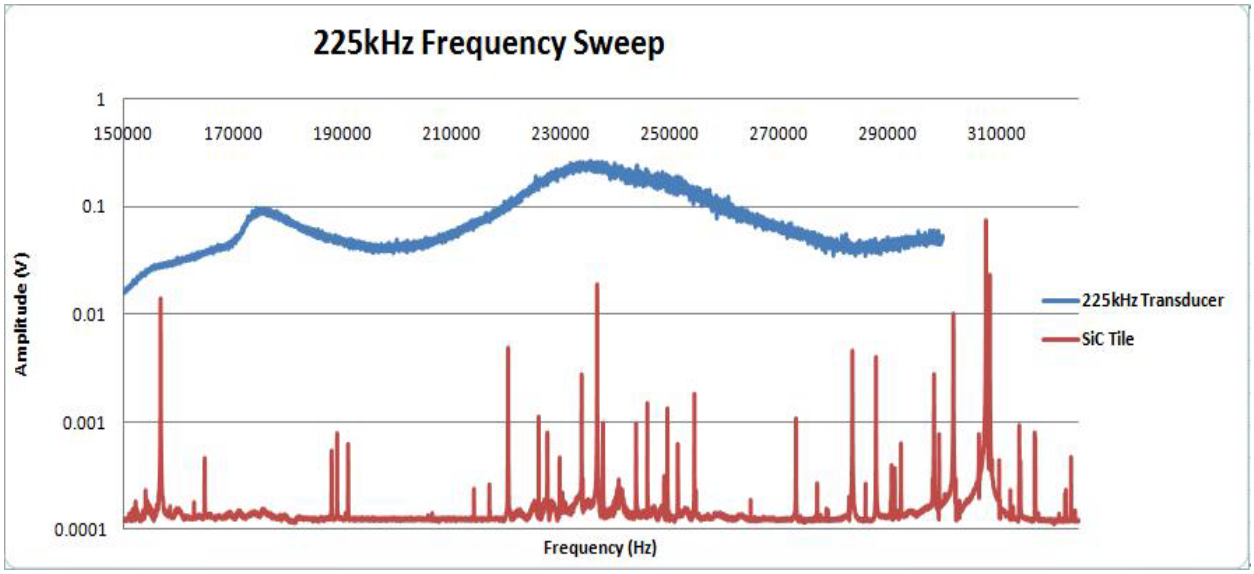

FIGURE 1.8. Frequency scan to detect strong resonances over the bandwidth of the 225 kHz transducer.

Also notice that there are many more resonant peaks within the 225 kHz transducer bandwidth than within the 100 kHz transducer bandwidth. This is because the number of resonant modes a given shape is able to support increases (as well as the complexity of the resonance patterns) with increasing frequency. Having multiple resonance peaks within the transducer bandwidth means that each of the resonance peaks will be excited when the first type of scans discussed above is used. This causes a superposition of resonance patterns which is discussed in the next section.

These scans were performed at low voltages so as not to damage the transducers. Unfortunately the voltage used was not high enough to overcome the damping effects from the other layers when they were added to the tiles and no signal was received. It was conjectured that a tone-burst system would be able to recreate the effects of the CW system but in small

enough bursts that more voltage could be put through the transducers without damaging them and thus a signal would be strong enough to propagate through the lay-up. No credible results were obtained using the tone-burst system. It seems that at this time, using the currently available transducers, isolating a frequency with which to scan the lay-up is not possible.

An Air-Coupled pulse-echo inspection was also attempted on a SiC tile without success. This is due to the long ring-down time and noise level of the transducer. When the back-wall echo reaches the transducer the transducer is still ringing from the initial pulse. Normally these two signals could be separated with a Fast Fourier Transform (FFT) (assuming the back-wall echo is not the same frequency as the initial pulse) but in this case the signal from the back-wall is of lower amplitude than the transducer noise.

Resonance Pattern Superposition

The images in this study are made by applying a time gate to the received signal and plotting the maximum amplitude of the waveform inside this time gate. Smaller sub-gates can also be applied to the signal so that images can be produced that correspond to specific portions of the waveform. This process allows for the observation of how the vibrations of the sample change with time.

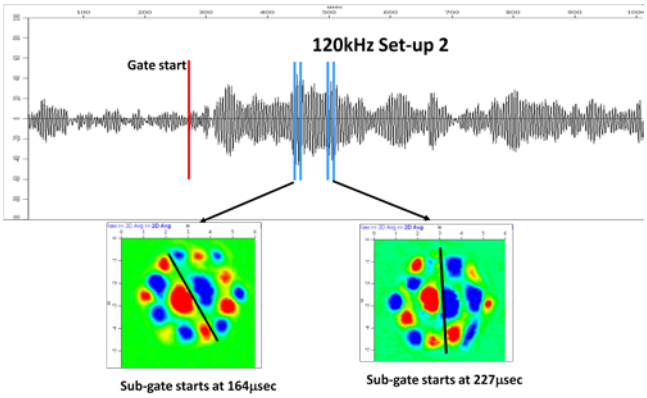

FIGURE 1.9. Different resonance patterns obtained from a through transmission scan of a bare SiC tile at 120 kHz. The images are produced by taking the amplitude maximum of the received waveform over the time sub-gate.

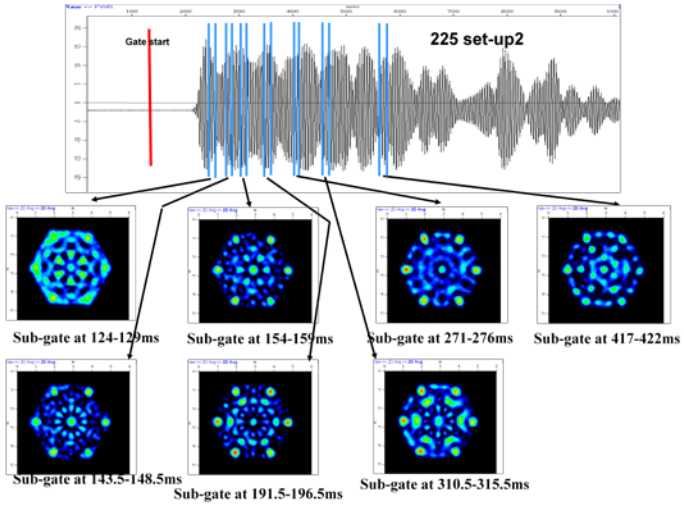

FIGURE 1.10. Different resonance patterns obtained from a through transmission scan of a bare SiC tile at 225 kHz. The images are produced by taking the amplitude maximum of the received waveform over the time sub-gate.

Fig. 1.9 shows several distinct resonance patterns observed in the bare SiC tile with through transmission at a frequency of 120 kHz. Likewise, Fig 1.10 shows several distinct resonance patterns observed in the bare tile with through transmission at a frequency of 225 kHz. The different images in each figure come from the same scan but from different times in the received signal. This shows that as the tile is allowed to ring down, it experiences several different resonant modes. The two images from the 120 kHz scan are actually a repeated mode.

Transducers have a finite, non-zero bandwidth that encompasses many resonances which occur at very specific, discrete frequencies. This means that each and every one of the resonances that is within the transducer bandwidth is excited by the transducer during a scan of type one discussed above. When a multitude of these resonances are excited at the same time the resonance images are superimposed in the scan results. It may also lead to constructive and destructive interference. This, in part, accounts for the complexity of the resonance images observed. Consider the implications of Fig. 1.7 and 1.8 on the results from the through transmission scans shown in Fig. 1.9 and 1.10 respectively. This superposition can be reversed

somewhat by stepping through the received signal, from the through scan of type one described above, with a small time-gate.

This indicates that resonance modes of different frequencies will travel through the material at different speeds which would mean there are different phase velocities and that the material is dispersive. It is not as simple as that however. Because of the large reflection coefficient of the SiC-air interface even a short ultrasonic pulse will produce a long ring down. The presence of multiple resonances within the bandwidth of the transducer will produce a superposition, yet there will be dominant resonance modes that may need to die down before the other resonance modes become apparent.

New ACUT Scanning Method

As mentioned previously, traditional ACUT tries to mimic the inspection techniques and capabilities of Immersion UT, but due to the high attenuation of the ambient air and the incredible impedance (ρc: density * wave velocity) mismatch between the material and air, pulse-echo inspection is extremely improbable with ACUT. Pitch-catch inspection is usually unavailable as well because of the inhomogeneous nature of the materials with which ACUT tends to operate (this does not hold true for surface waves). Through transmission is the only inspection technique that can be used to any great affect with ACUT.

Traditional ACUT has both drawbacks and benefits when compared to Immersion UT. The main drawbacks are: the difficulty in getting energy into the sample (due to the attenuation and impedance mismatch problems described above) and the minimum detectable flaw size is dependent on the wavelength of the particular frequency in the particular material (the same holds true for immersion), and with the low frequencies used in ACUT, this makes the

minimum flaw size fairly large (~1in in graphite/epoxy at 120 kHz). The benefits include the incredible penetration depth due to lower attenuation through materials at lower frequencies and the fact that this type of inspection is non-contact.

Based on this evidence, a new technique could be created (for this problem specifically and possibly for many others) that would utilize the strengths of ACUT. The preliminary scans (Fig. 1.4) demonstrated that the ceramic tiles vibrate so strongly that their resonances can be seen through all of the other layers and they actually suppress the vibrations of the other layers and force them to vibrate with the same pattern as the tiles.

It is proposed that since these tiles vibrate so strongly that their resonances are clearly visible and the minimum flaw size is fairly large, these resonances be used to detect and characterize flaws in the lay-up during the manufacturing process or after possible damage during combat or handling. Comparing the resonance patterns of the ceramic tiles in a lay-up with no defect to those of lay-ups with known defects at several frequencies should provide a good damage metric with which to develop this technique. Any flaws or damage in the tiles themselves should result in a change in the resonance pattern or the resonance frequency of the tile which will make the flaws and damage apparent. Likewise, any damage or flaws in the path of the propagating wave will affect the appearance of the resonance amplitude, or eliminating high amplitude regions of the resonance pattern. This technique is called Air-Coupled Ultrasonic Resonance Imaging (ACURI).

Flaw Detection Using ACURI Method

The question for this new flaw detection method is whether or not flaws can be detected and characterized in a multi-layer, multi-material composite lay-up using ACUT. Three

samples were used to explore this question. These three samples will be referred to as Panel A, Panel B, and Panel C and have the following characteristics: Panel A has the rough dimensions of 14 in x 15 in x 1.5 in, is composed mostly of hexagonal alumina tiles with one hexagonal SiC, and has no known defect in the materials or the lay-up; Panel B has the rough dimensions of 16 in x 18 in x1.5 in, is composed mostly of hexagonal alumina tiles with six complete hexagonal SiC tiles, and has six simulated disbonds; finally, Panel C has the rough dimensions of 21 in x 25 in x 1.5 in, is composed of ten complete hexagonal alumina tiles and eighteen complete hexagonal SiC tiles, and has 30 embedded defects, 12 inclusions and 18 simulated disbonds.

All of the tests performed on the three panels are ACUT through scans with both the transmitter and receiver scanning together (C-scan). The transducers used were Quality Material Inspection (QMI) <http://www.qmi-inc.com/> spherically focused probes with center frequencies of ~120 kHz and ~225 kHz with bandwidths of ~25%. The transducers were held ~2 in from both the front and back surfaces. The signal was impinged on the graphite side of the lay-up and was received on the S2 glass side of the lay-up.

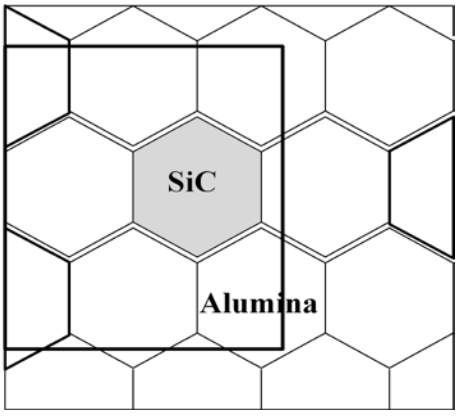

FIGURE 1.11. Layout of Panel A showing the approximate size and location of the ceramic tiles. The box indicates the portion of the scan considered in the images of Panel A.

The approximate size and location of both the hexagonal alumina tiles and the solitary hexagonal SiC tile of Panel A are shown in Fig. 1.11. The square outline over part of the figure outlines the area of interest for this panel and the scan images of Panel A are cropped to this approximate size.

The scans of Panel A, for both frequencies mentioned above, are shown in Fig. 1.12. The SiC tile can be easily distinguished from the alumina tiles due to a difference in the resonance patterns of the tiles. In the 120 kHz image, the SiC tile exhibits a series of high amplitude dots that form a spoke-like pattern where the alumina tiles show a series of separated dots that, while showing the same symmetry as the SiC tile, form a different pattern.

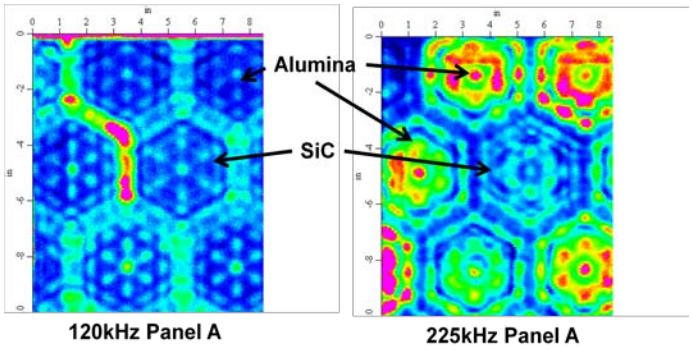

FIGURE 1.12. C-scan images of Panel A at 120 kHz (left) and 225 kHz (right). The images are produced by taking the amplitude maximum of the received waveform over the entire time gate.

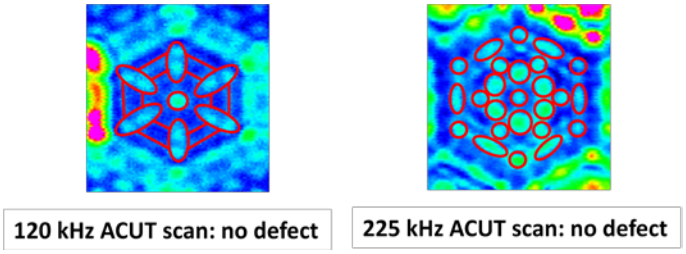

FIGURE 1.13. C-scan images of the SiC tile in Panel A at 120 kHz (left) and 225 kHz (right) with resonance patterns highlighted. The images are produced by taking the amplitude maximum of the received waveform over the entire time gate.

In the 225 kHz image, both the alumina tiles and the SiC tile have the same (or very similar) resonance patterns, however, the amplitude of the resonance patterns is different for the different material, and the SiC tile can still be easily distinguished.

Since there are no known defects over the SiC tile in this panel (Panel A), these resonance images will be used as a basis for comparison for the panels with defects to determine whether the defects can be visually detected. The resonance patterns have been outlined in Fig. 1.13 to make comparisons easier. The 225 kHz pattern is too intricate to use the entire pattern and since the defects are primarily over the center of the tiles only the inner part of the pattern will be used.

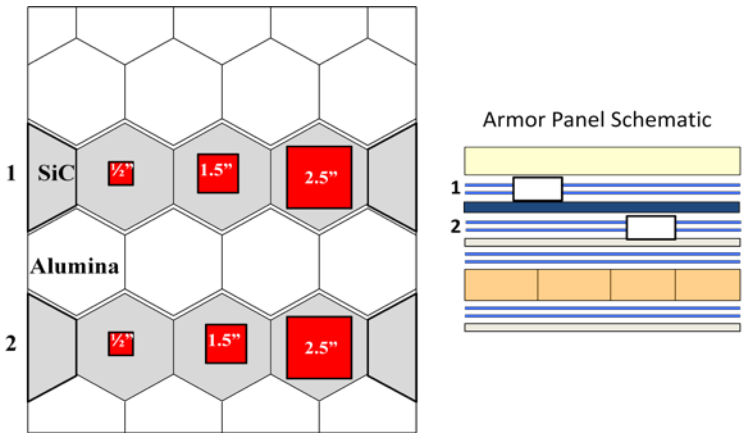

FIGURE 1.14. Layout of Panel B showing the approximate size and location of the ceramic tiles. The approximate size, shape, and locations of the 6 simulated disbonds are shown. The disbonds are located between different layers in the layup as indicated by the right part of the figure.

The approximate size and location of both the hexagonal alumina tiles and the hexagonal SiC tiles of Panel B are shown in Fig. 1.14. The approximate size, shape, and locations of the six engineered disbonds are also indicated. The disbonds are square, centered over the center of the SiC tiles, and come in the sizes of 0.5 in, 1.5 in, and 2.5 in. They were engineered by cutting the appropriately sized and shaped holes in both layers of the film

adhesive between two layers of the lay-up as indicated in the figure. This gives “void disbonds” instead of “kissing disbonds,” which makes it more difficult for an ultrasonic signal to pass through. As indicated in the figure, the two rows of disbonds are located between different material layers. The top row, labeled as row 1, has the disbonds between the rubber and S2 glass layers while the bottom row, labeled as row 2, has the disbonds between the graphite and rubber layers.

The defects in Panel B were created to simulate the effect of the inclusion of air during the manufacture of the lay-up. The square disbond shape is merely for ease of fabrication and serves no scientific purpose. The choice of the 0.5 in, 1.5 in, and 2.5 in sizes for these disbonds is not due to any mechanical significance, but merely to test the detection limits of this technique. We can term these sizes as small, medium, and large, based on detection capabilities in composites, for the purpose of detection.

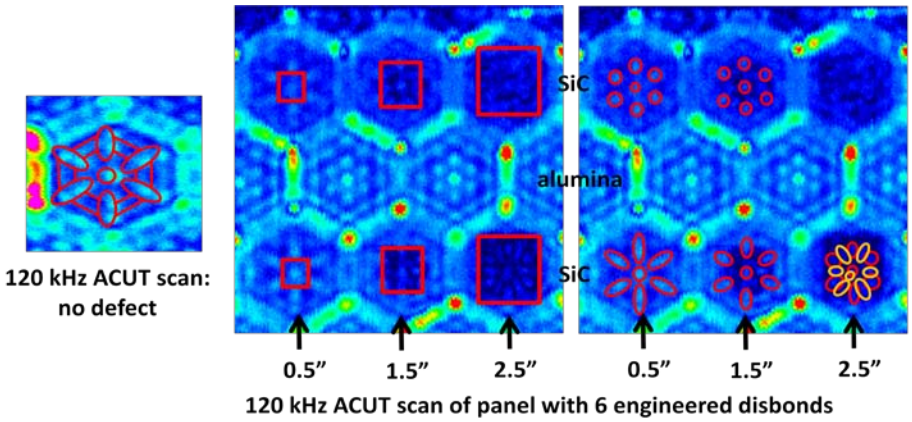

FIGURE 1.15. C-scan of Panel B at 120 kHz. (a) Resonance image of the bare SiC with 120 kHz resonance pattern outlined. (b) 120 kHz scan of full layup panel with six engineered disbands outlined. (c) 120 kHz scan of full layup panel with six engineered disbands and the resonance patterns outlined. The images are produced by taking the amplitude maximum of the received waveform over the entire time gate.

Fig. 1.15 shows the scan results for Panel B as well as the undamaged SiC tile from Panel A for the frequency of 120 kHz. In Fig. 1.15-b the approximate size, shape, and location

of the disbonds are outlined. A casual glance at Fig. 1.15-b shows that the 1.5 in and 2.5 in disbonds are clearly visible as dark cloudy areas in both the top and bottom rows in this scan. Furthermore, the 0.5 in disbond in the top row can be detected via a disruption of the resonance pattern when compared to the pattern of the tile with no known defect (Fig. 1.15-a) due to a large change in the amplitude and clarity of the resonance image. A slightly closer inspection of the image in Fig 1.15-b shows that a significant difference between the top and bottom rows can be observed. This means the difference in the disbond locations can be distinguished with through transmission due to these resonance patterns.

In Fig. 1.15-c the resonance patterns have been highlighted for easier comparison. If the top row of images is visually compared to the bottom row, the differences in the resonances are apparent. The bottom 0.5 in defect pattern matches very closely with the pattern of the tile with no known defect (Fig. 1.15-a) while the top 0.5 in defect pattern has a significantly different amplitude and seems to have been disrupted by something. Comparison of the 1.5 in defect patterns shows that they are basically the same as the 0.5 in defect patterns, that they show the same relation, but with a very low amplitude region in the approximate location of the disbonds. The top 1.5 in defect pattern is fairly chaotic and even though some of the resonance pattern is detectable it has been disrupted by the disbond significantly more than the bottom pattern. The top 2.5 in defect pattern is very chaotic and there is no detectable resonance pattern though the pattern is evident in the bottom row. The pattern in the bottom row matches the pattern of the tile with no known defect quite well (though much lower amplitude). There is also a secondary pattern (outlined in yellow-orange), though what causes this is unknown.

It is clear from these comparisons that 5 out of 6 of the disbonds are detectable with ACURI at a frequency 120 kHz and that there is a significant and noticeable difference

between the resonance images of the disbonds located between the rubber and glass layers and the disbonds located between the graphite and the rubber layers.

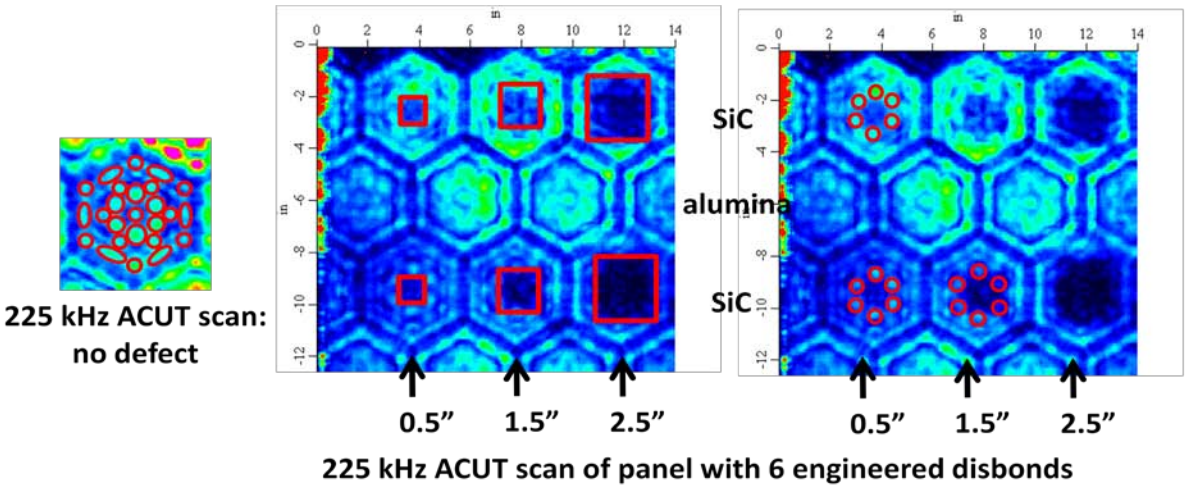

FIGURE 1.16. C-scan of Panel B at 225 kHz. (a) Resonance image of the bare SiC with 225 kHz resonance pattern outlined. (b) 225 kHz scan of full layup panel with six engineered disbands outlined. (c) 225 kHz scan of full layup panel with six engineered disbonds and the resonance patterns outlined. The images are produced by taking the amplitude maximum of the received waveform over the entire time gate.

Fig. 1.16 shows the same two panels shown in Fig. 1.15, but using a 225 kHz transducer instead of a 120 kHz transducer. Again the first image (Fig. 1.16-a) shows the resonance pattern of the tile in the lay-up with no known defects, the second image (Fig. 1.16-b) outlines the six engineered defects, and the third (Fig. 1.16-c) highlights some of the resonance patterns. A quick glance at the scan image shows that all 6 of the disbonds can be seen. Also evident is the difference between the top and bottom rows, namely that two of the three bottom disbonds have discernable resonance patterns while only one of the top disbonds has a discernable resonance pattern.

Looking at the 0.5 in disbonds, the top and bottom patterns are very similar and match well with the no defect pattern, however, the high amplitude center, clearly visible in the no defect pattern, is not present. This indicates that both of the 0.5 in disbonds are detectable. The

resonance pattern is still detectable for the bottom 1.5 in disbond, but not for any of the rest of the disbonds.

From these comparisons it is evident that 6 out of 6 of the disbonds are detectable with ACURI at a frequency of 225 kHz and that there is a significant and noticeable difference between the resonance images of the disbonds located between the rubber and glass layers and the disbonds located between the graphite and rubber layers. All six of the disbonds were easily detectable by comparing the defective resonance patterns with the non-defective patterns. Moreover, a difference in flaw location (which layers the flaw is between) can also be seen by comparing resonance patterns.

A possible explanation for the different disbond locations affecting the resonance patterns differently lies in the way in which the disbonds were engineered. Essentially there is a void for each disbond. Consider the vibrational displacement of the layers. The SiC tiles have the largest displacement (due to the vibration) of all of the layers. If the void/disbond is located between the second graphite layer and the rubber layer, the displacement of the graphite layer due to the SiC vibration may be larger than the thickness of the void/disbond and the displacement can be transferred to the subsequent layers. If the void/disbond is located between the rubber layer and the S2-glass layer, the displacement of the rubber layer due to the vibration of the SiC tile may be smaller than the thickness of the void/disbond and the displacement cannot be transferred to the S2-glass layer. This is because the rubber has a low modulus and high damping that will absorb a significant portion of the displacement of the graphite layer.

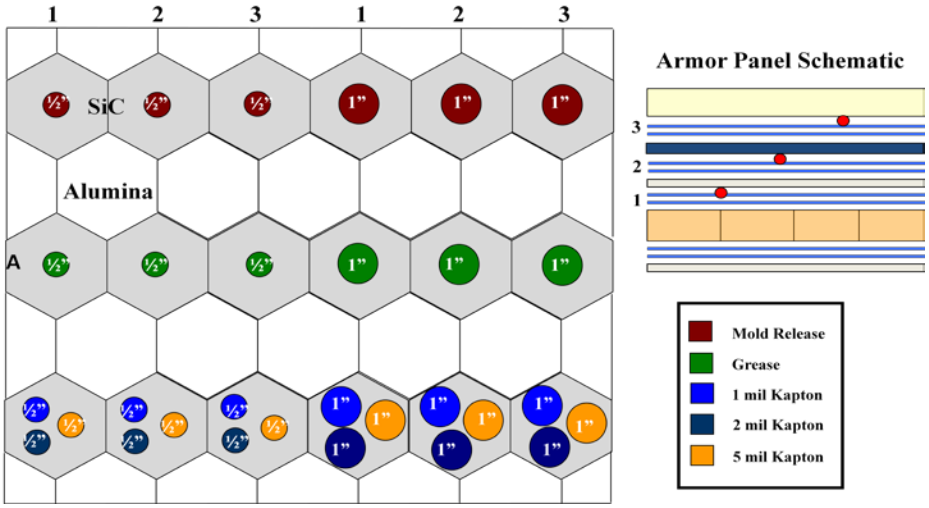

FIGURE 1.17. Layout of Panel C showing the approximate size and location of the ceramic tiles. The approximate size, shape, and locations of the 30 defects are shown. The defects are located between different layers in the layup as indicated by the right part of the figure.

The approximate size and location of both the hexagonal alumina tiles and the hexagonal SiC tiles of Panel C are shown in Fig 1.17. The approximate size, shape, and locations of the 30 engineered defects are also indicated. The materials included in the lay-up (mold release and grease) and their locations are indicated in the figure and as indicated the inclusions are circular, centered over the center of the Sic tiles, and come in the sizes of 0.5 in and 1 in. The disbonds are circular with each group of three centered over the center of the SiC tile and are made by including two circular layers of kapton of different thicknesses. Including two layers of kapton will create a “kissing” disbond that will transmit the signal when in compression but not in tension. As indicated in the figure, the six columns have two different sizes of defects and the defects are located between different material layers. The defects are between the SiC tiles and the graphite layer in the first and fourth columns, labeled as column 1, the second and fifth columns, labeled as column 2, have the defects between the graphite and rubber layers, and the third and sixth columns, labeled as column 3, have the defects between the rubber and S2-glass layers. The defects in Panel C were created to simulate the effect of

different types of possible inclusions during the manufacture of the lay-up and disbonds that may occur. Again the sizes are arbitrary and are merely to test the detection limits.

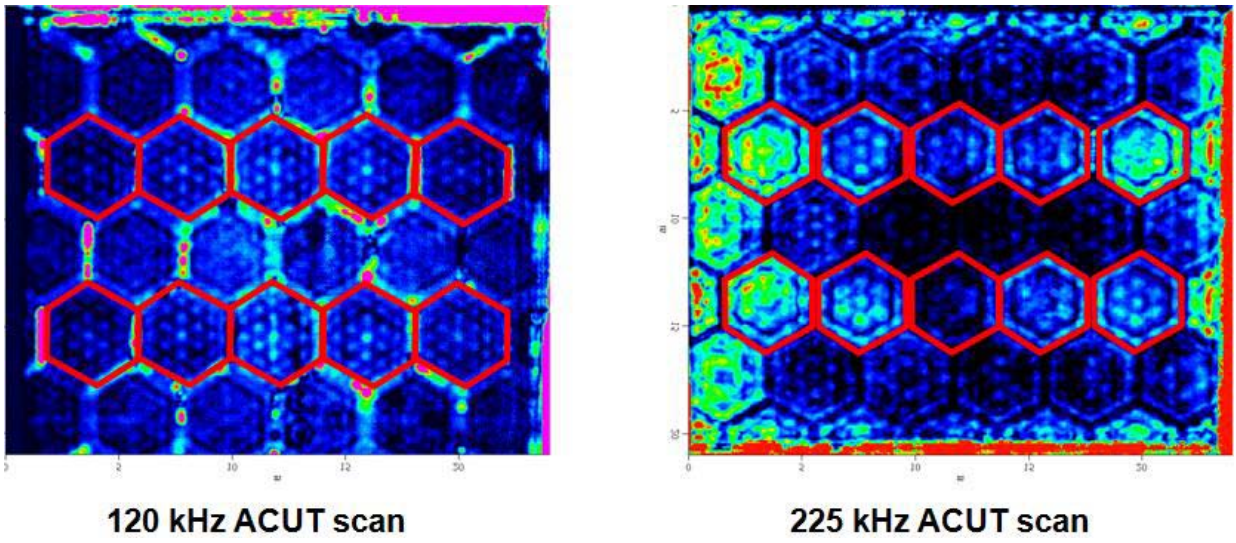

FIGURE 1.18. C-scan of Panel C. (a) 120 kHz scan of full lay-up with Alumina tiles outlined. (b) 225 kHz scan of full lay-up with Alumina tiles outlined. The images are produced by taking the amplitude maximum of the received waveform over the entire time gate.

Figure 1.18 shows the results from two resonance scans of Panel C, the first at 120 kHz and the second at 225 kHz. A comparison of all of the alumina tiles outlined in the figure shows a drastic difference in the amplitude and clarity of the resonance patterns, especially in the 225 kHz scan. Neither the scans of Panel A or Panel B show a similar issue. This indicates some deviation in the manufacture or handling with respect to Panels A and B. ACUT signals are sensitive to variations in the lay-up not caused by engineered defects, variations such as dry patches or delaminations. These variations can cloud or mask the actual engineered defects, which means that the presence of both engineered and accidental defects could make flaw detection difficult with this technique. Even though any results from Panel C cannot be

considered valid, a comparison of Panel A and Panel C yields some indications of flaw detection.

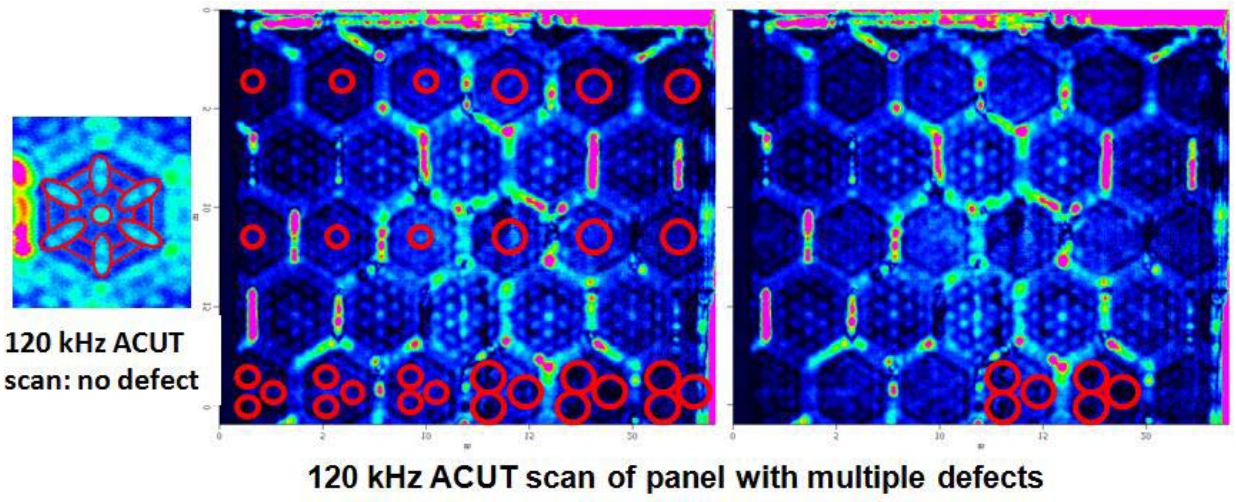

FIGURE 1.19. C-scan of Panel C at 120 kHz. (a) Resonance image of the bare SiC with 120 kHz resonance pattern outlined. (b) 120 kHz scan of full layup panel with engineered defects outlined. (c) 120 kHz scan of full layup panel with engineered defects and the difference in the resonance patterns outlined. The images are produced by taking the amplitude maximum of the received waveform over the entire time gate.

Fig. 1.19 shows the scan results for Panel C as well as the undamaged SiC tile from Panel A for the frequency of 120 kHz. In Fig 1.19-b the approximate size, shape, and location of the defects are outlined. Although the scan does not have very defined or consistent resonance patterns on the SiC tiles, due to a possible problem in the lay-up during the manufacture, two SiC tiles show indications of defects. Fig 1.19-c highlights six dark, cloudy, circular shapes in the fourth and fifth tiles of the bottom row of SiC tiles. These six dark areas correspond with six of the simulated kapton disbonds. The lack of indication of any other defect is probably due to problems with the lay-up.

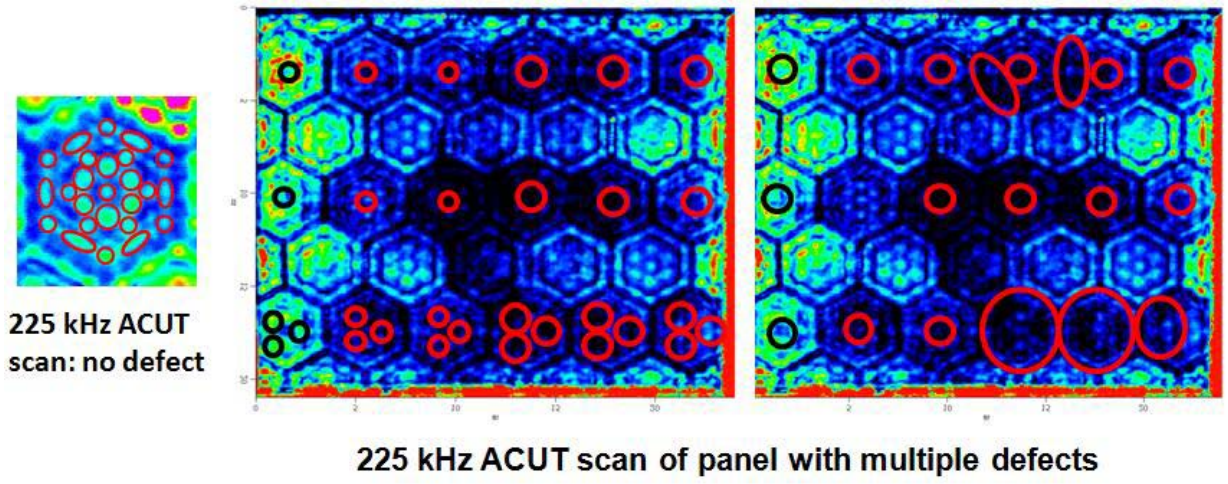

FIGURE 1.20. C-scan of Panel C at 225 kHz. (a) Resonance image of the bare SiC with 225 kHz resonance pattern outlined. (b) 225 kHz scan of full layup panel with six engineered disbands outlined. (c) 225 kHz scan of full layup panel with engineered defects and the difference in the resonance patterns outlined. The images are produced by taking the amplitude maximum of the received waveform over the entire time gate.

Fig. 1.20 shows the scan results for Panel C as well as the undamaged SiC tile from Panel A for the frequency of 225 kHz. In Fig 1.20-b the approximate size, shape, and location of the defects are outlined. Again the scan shows signs of some sort of unknown problem. Fig 1.20-c highlights differences in the resonance patterns between Panel A with no defect and Panel C. It is easier to highlight the differences because of the complexity of the resonance pattern. The highlighted differences in the top two rows of SiC tiles correspond with the grease and mold release inclusions and eleven of the twelve are detected because the high amplitude center in the resonance pattern is absent. The high amplitude center is again absent in the first three resonance patterns of the bottom row of the SiC tiles. This indicates a flaw of some kind but does not indicate the three simulated disbonds. The resonance patterns in the fourth and fifth SiC tiles in the bottom row are completely disrupted with possible indications of the circular disbonds. The sixth resonance pattern in the bottom row also shows evidence of disruption in locations that correspond with the locations of the disbonds.

Although the scans of Panel C did not produce very clear images and any conclusions can only be treated as conjectures, there is good evidence that the flaws would have been detectable in a better constructed sample. Eleven of the twelve inclusions and six of the eighteen disbonds were detectable with some certainty.

Future Work

The work presented in this thesis is only a beginning in the study of the ACURI technique and more work needs to be done to validate the results and conclusions of this study. More experiments need to be performed on a variety of samples with different types of defects and more modeling with FE should be performed to simulate different defects. Image processing should also be performed to determine whether the differences in resonance images between a non-defective tile/lay-up and a tile/lay-up with known defects can be detected with an automated or semi-automated program.

Some initial image processing was performed as part of this study. The resonance image of the SiC tile in Panel A (with no known defect) and the resonance image from one of the SiC tiles in Panel B (with six engineered disbonds) were compared. Several easily identifiable high amplitude regions on the image with no defect were selected along with the corresponding regions on the image with known defect. From the relative positions of these selected points a transform matrix was created and applied to the known defect image in order to rotate and align it with the no defect image. A cross-correlation was then performed to ensure that the images were properly aligned. The images were then subtracted and divided in several combinations to see if the defects were apparent.

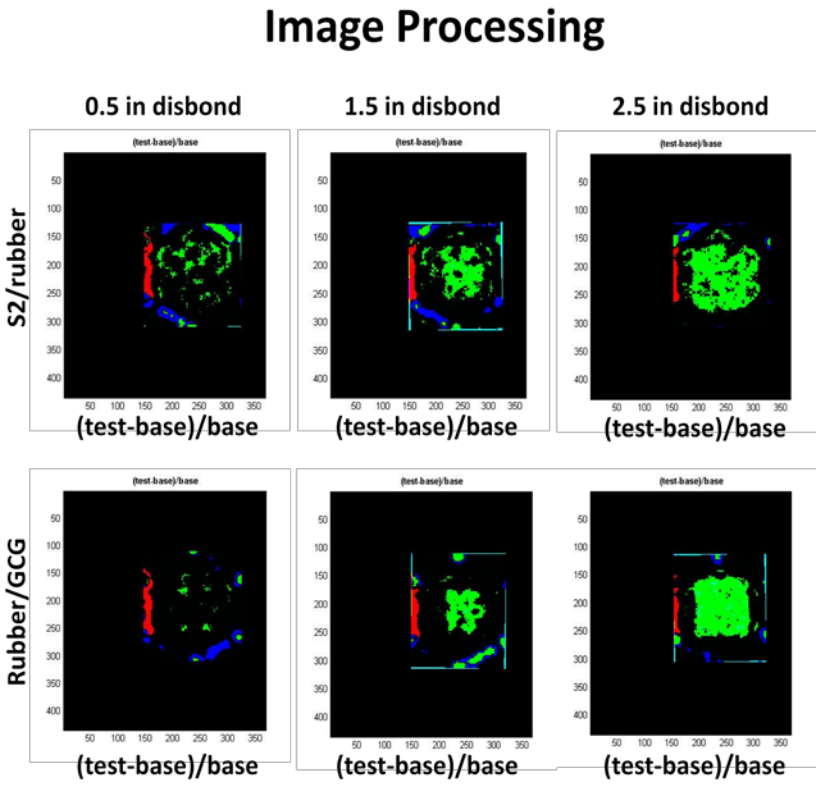

FIGURE 1.21. Results from preliminary image processing on Panel B.

The results from the initial attempt at image processing to detect the flaws in Panel B at 120 kHz are shown in Fig. 1.21. The 1.5 in and 2.5 in disbonds are clearly visible as bright green shapes. There are no shapes apparent for the 0.5 in disbonds, but there is some indication of an image difference. There is also an apparent difference between the top and bottom rows. This image processing technique has corroborated the conclusions drawn from visual comparison in the section Flaw Detection Using Proposed Method.

Since the images show a strong periodicity the next image processing technique to try utilizes 2D FFT's. Essentially the FFT of the no defect image is subtracted from the FFT of the known defect image with some preprocessing to reduce the noise of the images. Any residual data present after this subtraction process should indicate the presence of a defect and possibly allow for flaw characterization.

Conclusion

The multi-layer, multi-material composite armor considered in this study provides some difficulties for many traditional NDE techniques. The ceramic tiles at the center of this composite material have special properties that can and should be utilized when creating an optimized detection technique. These SiC are remarkable resonators when driven to vibrate, and there are many distinct natural resonances with distinctive resonance patterns within the bandwidth of the transducers used. Several of these resonances are very strong and have a resonance sharpness, or Q factor, comparable to or above that of quartz. It has been shown that these resonance patterns can be used to detect and characterize flaws. All six of the engineered disbonds in Panel B were detectable along with information indicating between which two layers the disbonds were located. Even with the poor scan results from Panel C eleven of the twelve inclusions and six of the eighteen disbonds were detectable.

The ACURI technique developed in this study shows great promise for this material specifically and for several different types of materials in general. More work needs to be done by scanning samples containing different defects, using frequency scans (cw scans at specific frequencies), and using image processing to detect flaws.

References

1.1. Grandia, W., Fortunko, C., "NDE Applications of Air-Coupled Ultrasonic Transducers," *Proceedings, IEEE Ultrasonics Symposium*, 1995

1.2. Bhardwai, M., "Non-Contact Ultrasound: The Final Frontier in Nondestructive Testing and Evaluation," *Encyclopedia of Smart Materials*, 2001 John Wiley & Sons, New York

1.3. Hsu, D. K., Barnard, D. J., Peters, J. J., Dayal, V., "Development of Nondestructive Inspection Methods for Composite Repair," *Proceedings, Review of Progress in Quantitative Nondestructive Evaluation*, 2003, Vol. 657, pp. 1019-1025

1.4. Peters, J., Kommareddy, V., Liu, Z., Fei, D., Hsu, D., "Non-contact Inspection of Composites Using Air-Coupled Ultrasound," *Proceedings, Review of Progress in Quantitative Nondestructive Evaluation*, 2003, Vol. 657, pp. 973-980

1.5. Holland, S. D., Teles, S. V., Chimenti, D. E., "Quantitative Air-Coupled Ultrasonic Materials Characterization with Highly Focussed Acoustic Beams," *Proceedings, Review of Progress in Quantitative Nondestructive Evaluation*, 2004, Vol. 700, pp. 1376-1381

1.6. Hsu, D. K., Barnard, D. J., Peters, J. J., Polis, D. L., "Application of Air-Coupled in NDE of composite Space Structures," *Proceedings, Review of Progress in Quantitative Nondestructive Evaluation*, 2004, Vol. 700, pp. 851-858

1.7. Hsu, D. K., Kommareddy, V., Barnard, D. J., Peters, J. J., Dayal, V., "Aerospace NDT Using Piezoceramic Air-Coupled Transducers," *Proceedings, World Conference on NDT*, 2004

1.8. Hsu, D. K., Peters, J. J., Barnard, D. J., Kommareddy, V., Dayal, V., "Experience with Air-Coupled Ultrasonic Inspection of Aerospace Composites," *Review of Progress in Quantitative Nondestructive Evaluation*, 2004

1.9. Kommareddy, V., Peters, J. J., Dayal, V., Hsu, D. K., "Air-Coupled Measurements in Composites," *Proceedings, Review of Progress in Quantitative Nondestructive Evaluation*, 2004, Vol. 700, pp. 859-866

1.10. Peters, J. J., Barnard, D. J., Hsu, D. K., "Development of a Fieldable Air-Coupled Ultrasonic Inspection System," *Proceedings, Review of Progress in Quantitative Nondestructive Evaluation*, 2004, Vol. 700, pp. 1368-1375

1.11. Peters, J. J., Dayal, V., Barnard, D. J., Hsu, D. K., "Resonant Transmision of Air-Coupled Ultrasound Through Metallic Inserts in Honeycomb Sandwich Structures," *Proceedings, Review of Progress in Quantitative Nondestructive Evaluation*, 2005, Vol. 760, pp. 1026-1032

1.12. Barnard, D. J., Hsu, D. K., "Development of Practical NDE Methods for Composite Aircraft Structures," *Proceedings, Review of Progress in Quantitative Nondestructive Evaluation*, 2006, Vol. 820, pp. 1019-1026

1.13. Hsu, D. K., "Nondestructive Testing using Air-Bourne Ultrasound," *Ultrasonics*, 2006, Vol. 44, sup. 1, pp. 1019-1024

1.14. Hsu, D. K., Barnard, D. J., "Inspecting Composites with Airborne Ultrasound : Through Thick and Thin," *Proceedings, Review of Progress in Quantitative Nondestructive Evaluation*, 2006, Vol. 820, pp. 991-998

1.15. Dayal, V, Hsu, D. K., Kite, A. H., "Air-Coupled Ultrasound-A New Paradigm in NDE," in *Proceedings, ASME 2007 International Mechanical Engineering Congress and Exposition*, Seattle, WA, 2007, Vol. 13, pp. 153-155

1.16. Hsu, D. K., Barnard, D. J., Dayal, V., "NDE of damage in Aircraft Flight Control Surfaces," *Proceedings, Review of Progress in Quantitative Nondestructive Evaluation*, 2007, Vol. 894, pp. 975-982

1.17. Im, K. H., Chang, M., Hsu, D. K., Song, S. J., Cho, H., Park, J. W., Kweon, Y. S., Sim, J. K., Yang, I. Y., "Feasibility on Ultrasonic Velocity using Contact and Non-Contact Nondestructive Techniques for Carbon/Carbon Composites," *Proceedings, Review of Progress in Quantitative Nondestructive Evaluation*, 2007, Vol. 894, pp. 1013-1020

1.18. Dayal, V., Hsu, D. K., Kite, A. H., "Damage Modelling in Composites for NDE," *Proceedings, Review of Progress in Quantitative Nondestructive Evaluation*, 2008, Vol. 975, pp. 927-933

1.19. Dayal, V., Hsu, D. K., "Air-coupled Ultrasound for the NDE of Composites," *World Journal of Engineering*, 2010, Sup. 2, pp. 381

1.20. Migliori, A., Darling, T. W., "Resonant Ultrasound Spectroscopy for Materials Studies and Non-destructive Testing," *Ultrasonics*, 1995, Vol. 34, Issues 2-5, pp. 473-476

1.21. Cabrera, M., Castell, X., Montoliu, R., "Crack Detection System Based on Spectral Analysis of a Ultrasonic Reference Signals," in *IEEE International Conference on Acoustics, Speech, and Signal Processing, 2003 Proceedings*, 2003, Vol. 2, pp. 605-6

CHAPTER 3.
ANALYTICAL EQUATION OF THE TRANSVERSE VIBRATION OF A HEXAGONAL PLATE

Introduction

Analytical equations describing the transverse deflection and vibration of rectilinear and triangular plates are well known and have been a topic of inquiry for the past hundred years. These equations are fairly straight forward and solvable. Conversely, the equations describing the transverse deflection and vibration of higher order polygonal shapes are difficult to formulate and to solve. A solution to this problem was proposed in 1961 and has been accepted by the academic community. During the course of this research the use of the 1961 analytical solution was attempted. The results were compared with the experimental results and the results from a numerical solution, and it was observed that there are some inherent limitations with the analytical solution. The analytical results and the inherent limitations observed are presented and discussed in this chapter.

Literature Review

In 1820 Navier presented a paper to the French Academy of Science on the solution of a simply supported rectangular plate in the form of a double trigonometric series [2.4]. In his 1899 paper to the French Academy of Science, M. Maurice Lévy presented a solution to the biharmonic equation that describes the equilibrium of a rectangular plate [2.6]. This solution is an alternate solution to that proposed by Navier. It suggests a form of a single trigonometric series and was readily accepted by the academic community.

Kaczkowski utilizes Lévy's proposed solution in a 1961 paper to analytically determine the transverse vibration of regular polygonal plates by applying the solution to a triangular section of the plate created by the plate symmetry lines [2.2]. The results from the analysis performed by Kaczkowski was used by Leissa in his 1969 publication [2.1] and subsequently in several papers and publications such as K. Chauncey Wu's 1991 paper, "Free Vibration of Hexagonal Panels Simply Supported at Discrete Points," which analyses hexagonal plates for space craft.

Solution Proposed by Kaczkowski

In his 1961 paper [2.2], Von Zbigniew Kaczkowski presents and explores a unique approach to the solution of the transverse vibration of regular polygonal figures (Fig. 2.1). He proposed that applying the well known equation for the transverse vibrational displacement to a triangular section of the plate makes the solution for shapes with more than four sides easier to obtain. The triangular sections are chosen by using the symmetry lines of the polygon, and when the solution for the triangular section is calculated the solution for the full plate can be found by mirroring the triangular solution. The development of Kaczkowski's solution is given briefly below and is given in its entirety in Appendix A1. To test the validity and accuracy of this analytical model, it will be compared to the results of a Finite Element Model (FEM: numerical model) and to the results of Air-Coupled Ultrasonic Resonance Imaging (ACURI: experiment).

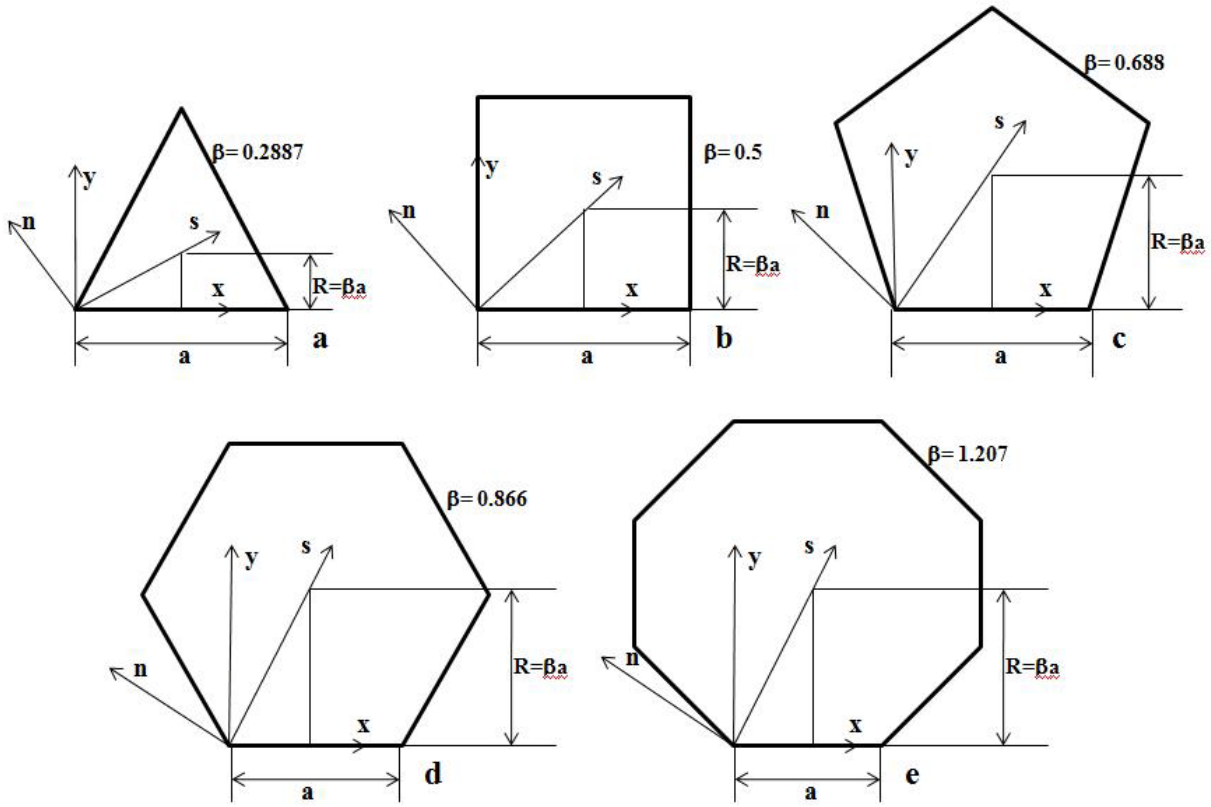

FIGURE 2.1. Several polygonal figures with Cartesian coordinate systems and new coordinate systems used in the development of the analytical equation.

Kaczkowski considers an isotropic plate with a regular n-sided polygonal shape and thickness h. The plate is on an elastic base with Winkler coefficient K and has a time-independent clamping force, N, applied evenly on the entire periphery and normal to the edges. Thin, ideal, elastic plate theory is valid. The equation for the transverse vibrational displacement, w, for the natural frequencies of the plate takes the well-known form:

$$D\nabla^2\nabla^2 w(x,y) + N\nabla^2 w(x,y) - (\mu\omega^2 - K)w(x,y) = 0 \qquad (2.1)$$

Where D is the plate bending stiffness, μ is the plate area mass, and ∇^2 is the Laplacian operator. He then applies this equation to the triangular section described in Fig.2.2.

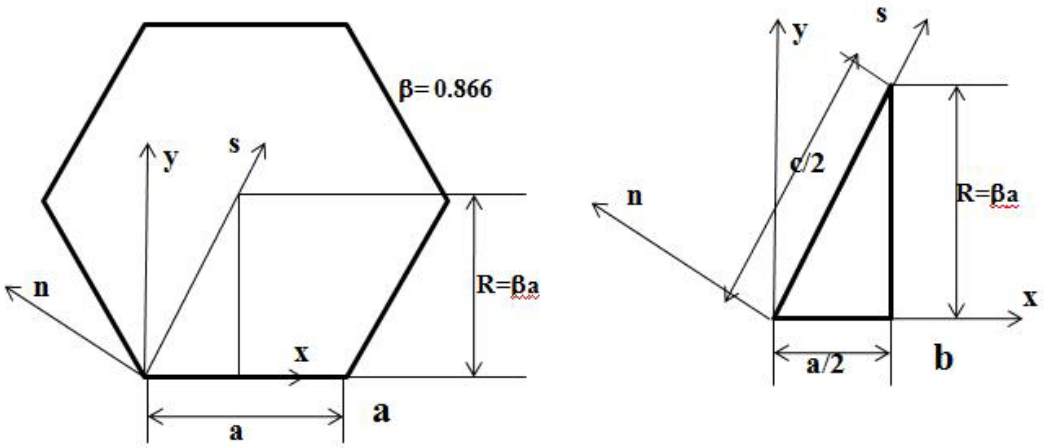

FIGURE 2.2. The regular hexagon and the triangular section used in the development of the analytical equation.

The differential equation (2.1) can be difficult to solve. Kaczkowski utilizes a solution proposed by M. Lévy for bi-harmonic equations. The simple series (2.2), fulfills (2.1) when the function $Y_m(\eta)$ satisfies the ODE (2.3) with the substitutions (2.4) and (2.5).

$$w(x,y) = \sum_{m=1,3,5,\dots}^{\infty} Y_m(\eta)\sin(m\pi\xi) \qquad (\xi = {}^{x}/_{a},\ \eta = {}^{y}/_{a}) \tag{2.2}$$

$$\frac{d^4Y_m}{d\eta^4} - 2\gamma_m \frac{d^2Y_m}{d\eta^2} + \delta_m^2 Y_m = 0 \tag{2.3}$$

$$\gamma_m = (m\pi)^2\left(1 - \frac{\Lambda}{m^2}\right), \qquad \delta_m^2 = (m\pi)^4\left(1 - 2\frac{\Lambda}{m^2} - \frac{\Omega}{m^4}\right) \tag{2.4}$$

$$\Lambda = \frac{Na^2}{2\pi^2 D}, \qquad \Omega = \frac{\mu\omega^2 - K}{\pi^4 D}a^4 \tag{2.5}$$

The general integral of the differential equation (2.1), which fulfills the symmetric boundary condition on the line x = a/2 (due to the sine function) has the following form:

$$w(x,y) = \sum_{m=1,3,5,\dots}^{\infty}(A_m\cosh(m\pi\varphi_m\eta) + B_m\sinh(m\pi\varphi_m\eta) + C_m\cosh(m\pi\psi_m\eta) + D_m\sinh(m\pi\psi_m\eta))\sin(m\pi\xi) \tag{2.6}$$

$$\varphi_m = \sqrt{1 - \frac{\Phi}{m^2}}, \quad \psi_m = \sqrt{1 - \frac{\Psi}{m^2}} \tag{2.7}$$

$$\Phi = \Lambda - \sqrt{\Lambda^2 + \Omega}, \quad \Psi = \Lambda + \sqrt{\Lambda^2 + \Omega} \tag{2.8}$$

Of the four coefficients in the above equation, two can be calculated by considering the boundary conditions on the edge y=0. This edge is where the clamping force is applied. According to Kaczkowski the coefficients for the free and fixed boundary conditions are defined, respectively, as the following:

$$\left.\begin{array}{c} A_m = C_m = 0 \\ C_m = -A_m, \qquad D_m = -\frac{\varphi_m}{\psi_m} B_m \end{array}\right\} \tag{2.9}$$

Where the coefficients A_m and C_m, in the case of a freely held plate, have most likely been chosen not because they are the solutions to the boundary conditions but because the plate is not symmetric about the x-axis and the even functions of y are discarded. The coefficients for the fixed plate come from the solutions for the boundary conditions on the edge y=0 as described in Appendix A1. These coefficient equations can then be combined with the equations resulting from the boundary conditions on the line y=2βx to explicitly solve for the coefficients.

Kaczkowski goes on to formulate the boundary conditions for the line y=2βx by implementing the new coordinate system below,

$$\left.\begin{array}{c} x = s\frac{a}{c} - n\frac{2\beta a}{c}, \qquad y = s\frac{2\beta a}{c} + n\frac{a}{c}, \\ \xi = \sigma - 2\beta\zeta, \quad \eta = 2\beta\sigma + \zeta, \quad \sigma = \frac{s}{c}, \quad \zeta = \frac{n}{c} \end{array}\right\} \tag{2.10}$$

This rotates the axes so they are normal and tangent to the line y=2βx just as the original coordinate system was normal and tangent to the line y=0. Doing this makes the boundary equations easier to handle. He uses this and some mathematical manipulation to obtain equations for the boundary conditions, but does not explicitly solve for the four coefficients of the differential equation.

Applying the proposed solution to the four boundary conditions yields a system of homogeneous equations that can be solved explicitly. The two boundary conditions on the line $y=2\beta x$ yield equations that are hyperbolic functions of the line length. This means that the equations are nonlinear in the tangent coordinate (s) of the line but linear in the coefficients. Because of this, we were able to solve the system of equations using Singular Value Decomposition at discrete values of s, the results of which are shown in Fig 2.3 and 2.4.

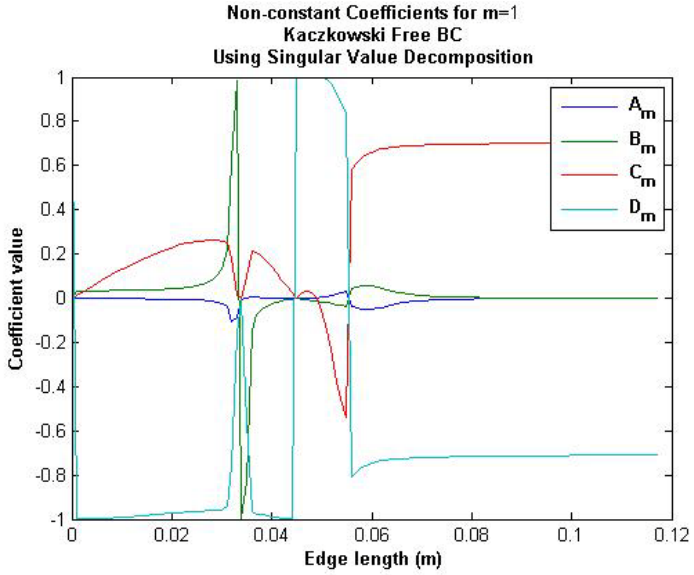

FIGURE 2.3. Plot of the Kaczkowski coefficients for the vibration of a freely held hexagonal plate as a function of line length.

Due to the hyperbolic nature of two of the four coefficient equations, all four coefficients vary drastically with increasing side length as is evidenced by the plots. If the determinant of the system is calculated for each of the values of s, it can be found that the system only has exact solutions for the value s=0. With this consideration the transverse vibration can be calculated over the face of the plate section.

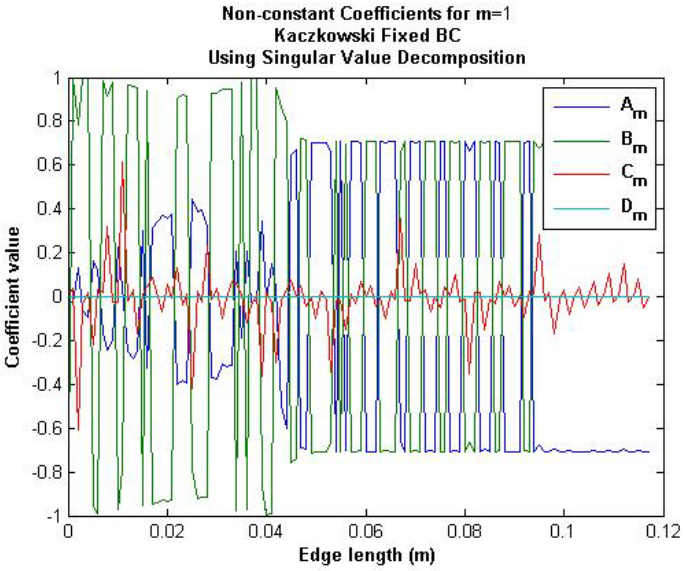

FIGURE 2.4. Plot of the Kaczkowski coefficients for the vibration of a freely held hexagonal plate as a function of line length.

Kaczkowski obtains the fundamental frequency of a freely bound plate with the following equation:

$$\omega = \frac{X\pi^2}{R^2}\sqrt{\frac{D}{\mu}}\sqrt{1 - \frac{NR^2}{X\pi^2 D} + \frac{KR^2}{X^2\pi^4 D}} \tag{2.11}$$

Where R comes from (Fig 2.1) and X = 0.529 for a hexagon. This gives the fundamental frequency of a freely bound hexagonal Silicon Carbide (SiC) plate with the following dimensions as:

$$R = 0.0508m, \quad D = 0.25373MPa, \quad \mu = 58.2625\,\frac{kg}{m^2} \tag{2.12}$$

$$f_{fundamental} = 21.248\,kHz$$

Examination of Solution

In order to examine the validity and accuracy of the solution proposed by Kaczkowski, three cases are compared. The first case takes the equations from Kaczkowski's paper and plots

the results using Matlab. The second case uses the results from a FEM modal analysis performed using ANSYS, which extracts the natural modes and frequencies. The third case uses results from ACURI testing of the hexagonal SiC tile modeled, as described in Chapter 1.

Kaczkowski's Solution

In his paper Kaczkowski fails to explain how to determine any resonance frequencies above the fundamental. Because of this the only test frequencies available are those from the FEM results. These were put into the analytical equation and the results were plotted. The first image in the following two plots is the fundamental frequency provided in Kaczkowski's paper.

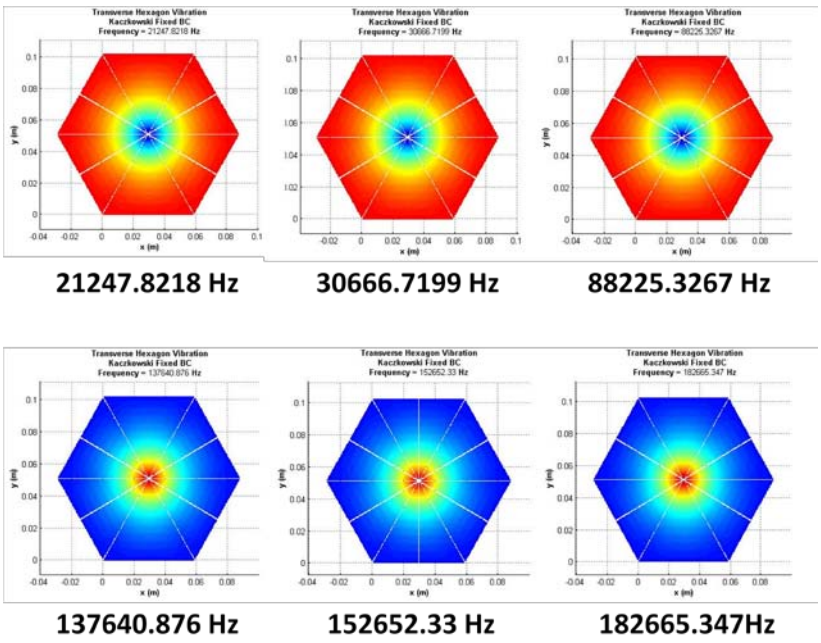

FIGURE 2.5. Results from Kaczkowski's solution with fixed boundaries.

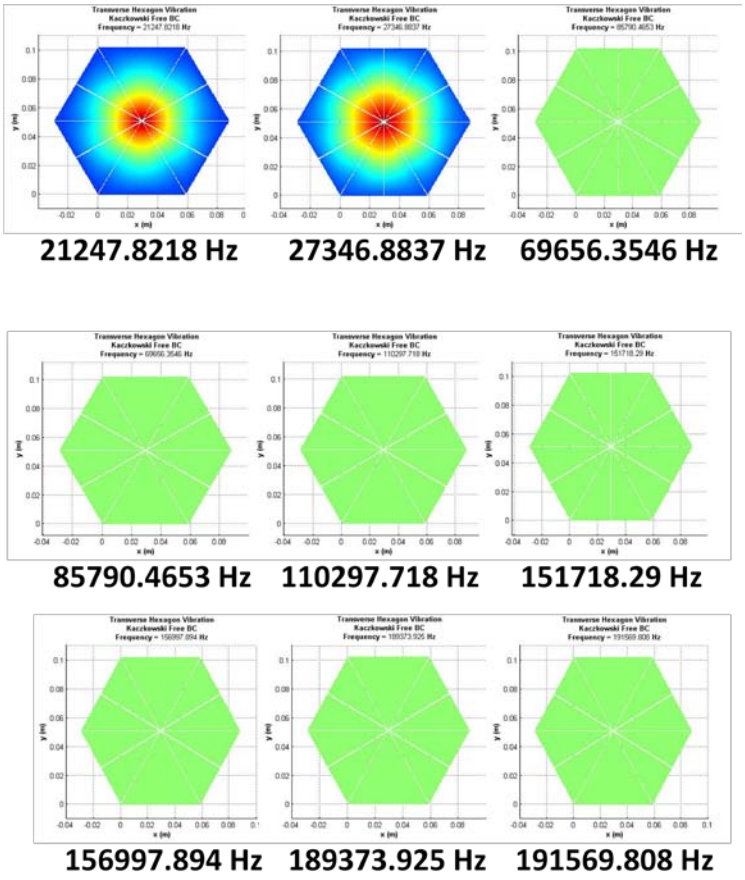

FIGURE 2.6. Results from Kaczkowski's solution with free boundaries.

Fig. 2.5 and 2.6 show the results from Kaczkowski's equation for several frequencies. In these images blue is low amplitude while red is high amplitude. Since the plate is vibrating the high and low amplitude regions will alternate in sign, and hence color, in a cyclical manor. Because of this the colors are interchangeable. It is easy to see from these two figures that Kaczkowski's solution does not vary with frequencies above those of the fundamental frequency. This suggests that the solution does not fully articulate the transverse vibration of the hexagonal plate and that it is possible that this solution is only valid for the prediction of the fundamental frequency.

FEM Solution

Since Kaczkowski's solution only considers a case where both interior edges are subject to a symmetric boundary condition the FE model used similar boundary conditions. The results from the modal analysis are presented in Fig. 2.7 and Fig. 2.8. In these images blue is negative displacement while red is positive displacement. Again since the plate is vibrating the high and low amplitude regions will alternate in sign, and hence color, in a cyclical manor. Because of this the colors are interchangeable.

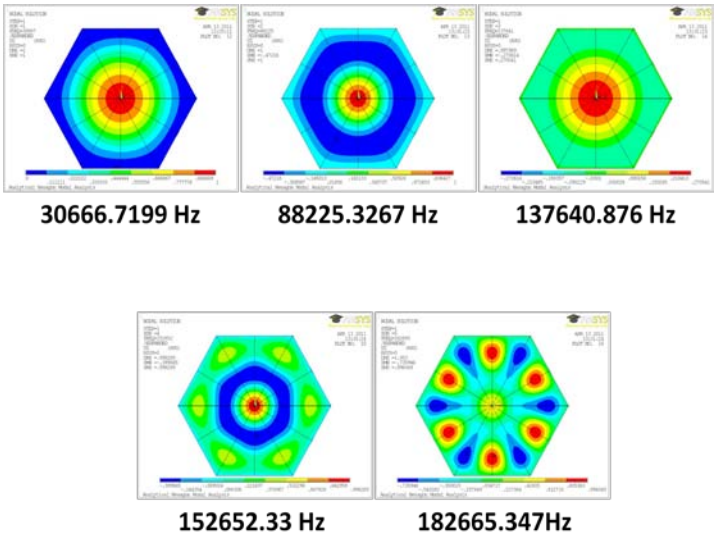

FIGURE 2.7. FEM modal results for a 1/12 section of the hexagonal plate with fixed external boundary.

The analytical solution does not match well, or at all, with the numerical FEM solution. Only the first resonance pattern and frequency from the FEM results find a match in the analytical solution and that is the fundamental mode. Though the fundamental resonance pattern matches well between the analytical solution and the FEM solution, the fundamental resonance frequency differs by ~22% between the two for the free boundary condition.

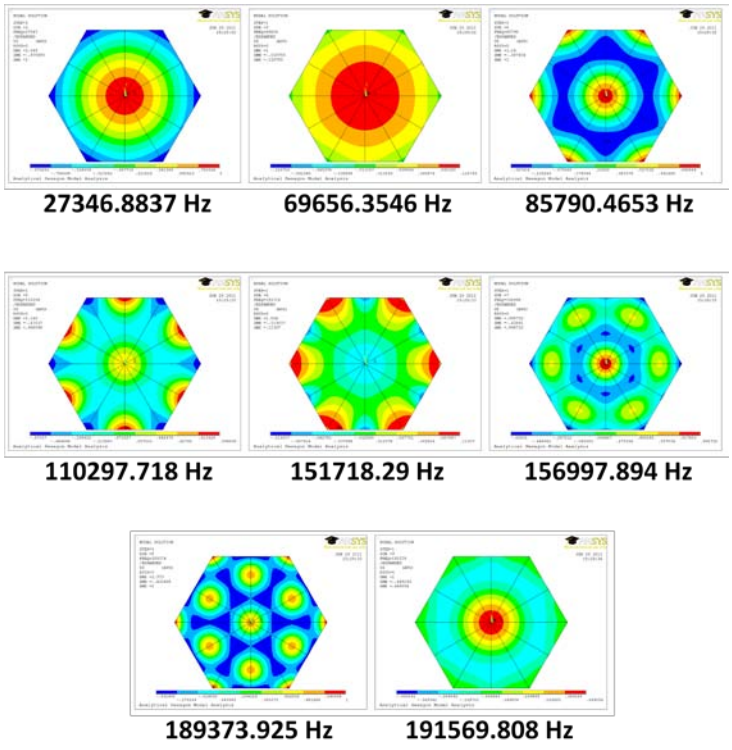

FIGURE 2.8. FEM modal results for a 1/12 section of the hexagonal plate with free external boundary.

ACURI Solution

The ACURI testing of the shape and material modeled with Kaczkowski's equation and FEM could not completely replicate the conditions in the two models. There is no way to ensure the periphery of the plate is completely free or fixed. Also there is no way to ensure that all of the lines of symmetry of the plate are symmetric boundaries. Furthermore, the specific frequencies predicted by FEM and used in the Kaczkowski model could not be impinged on the plate. Instead several transducers with bandwidths were employed, none of which were able to capture the fundamental frequency of the plate.

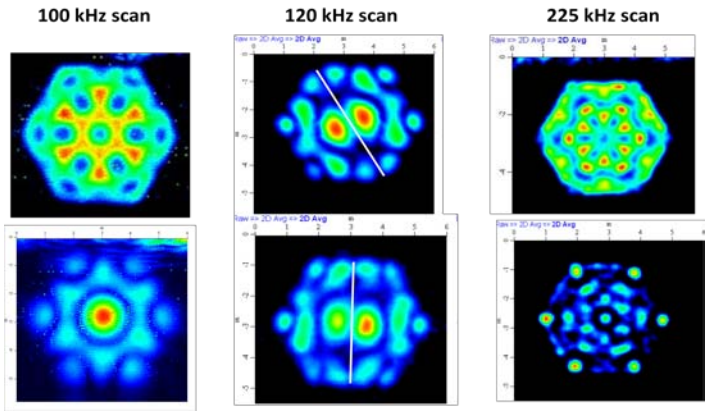

FIGURE 2.9. ACURI scan results of SiC tile at 100 kHz, 120 kHz, 225 kHz. The images are produced by taking the amplitude maximum of the received waveform either over the entire time gate or a smaller sub-gate.

Fig. 2.9 shows the results from several ACURI scans at several frequencies. In these images blue is low amplitude while red is high amplitude. Again since the plate is vibrating the high and low amplitude regions will alternate in sign, and hence color, in a cyclical manor. Because of this the colors are interchangeable. The analytical solution does not match with any of the observed ACURI results of the plate, though several of the FEM and RCURI results match.

Examination of Solution Formulation

The above comparison of the analytical solution, numerical solution, and experimental results demonstrates that the solution developed by Kaczkowski does not accurately describe the vibrational behavior of a regular hexagonal plate. An examination of the formulation of Kaczkowski's solution shows some differences from the plate equation derivation detailed in literature as well as some discrepancies.

Compare equation (A1.1) and equation (A2.20).

$$D\nabla^4 w(x,y) + N\nabla^2 w(x,y) - (\mu\omega^2 - K)w(x,y) = 0 \qquad \text{(A1.1)}$$

$$D\nabla^4 w - \mathrm{N_x}\frac{\partial^2 \mathrm{w}}{\partial x^2} - 2\mathrm{N_{xy}}\frac{\partial^2 \mathrm{w}}{\partial x \partial y} - \mathrm{N_y}\frac{\partial^2 \mathrm{w}}{\partial y^2} - (\mu\omega^2 - \mathrm{K})\mathrm{w} = 0 \qquad \text{(A2.20)}$$

The mid plane force term in the equation used by Kaczkowski is significantly different from the equation presented in the literature. Kaczkowski never discusses the force N except to say that it is the clamping force. Since N is the clamping force it is applied normal to the periphery of the full plate. The top of the plate was free and the bottom was subject to the Winkler Stiffness, K. When a section of the plate is considered, as in Fig 2.2b, the force N should be applied solely in the positive y direction on the line y=0. All boundary conditions on the lines x=a/2 and y=2βx will take into account the resultant forces from the clamping force applied to the other sides of the full plate.

It can be argued that Eq. A1.1 is just a special case of Eq. A2.20 where the equation is applied on a thin film (N_{xy}=0) and the stress is homogeneous (N_x =N_y). If this were the case then N could not be applied to the Laplacian of w as Kaczkowski does in Eq. A1.1 because the middle term $\partial^2 w/\partial x \partial y$ would still be present in the equation.

The first boundary condition used by Kaczkowski is from the symmetry line x=a/2. He states that since the condition on the line is symmetric, the solution can only contain solutions that are even functions of x with respect to the line and thus retains the $\sin(m\pi\xi)$ term.

The free boundary condition on the line y=0 seems to be processed in a similar manor. Kaczkowski assumes that since the plate boundary is free, it is not symmetric about the line and the even functions of y can be discarded. This idea will duplicate the condition stated in the first line of Eq. 2.7. There is nothing about the coefficients B_m and D_m. This is not the typical treatment of a free boundary condition in literature and applying the equations for a free boundary does not yield the same coefficient equations. (See Appendix A2).

The fixed boundary conditions used by Kaczkowski on the line y=0 seem to be consistent with the fixed boundary condition discussed in literature.

The symmetric boundary conditions used by Kaczkowski on the line y=2βx are

$$\left(\frac{\partial w}{\partial \zeta}\right)_{\zeta=0} = 0 \qquad \text{(A1.10a)}$$

$$\left(\frac{\partial \nabla^2 w}{\partial \zeta}\right)_{\zeta=0} = 0 \qquad \text{(A1.11a)}$$

The fist condition, Eq (A1.10a), matches with the condition in literature, Eq (A1.14a). The second condition, Eq (A1.11a), differs by (2-ν) in the second term.

$$\left(\frac{\partial w}{\partial n}\right)_{y=2\beta x} = 0 \qquad \text{(A1.14a)}$$

$$V_n = \left(Q_n + \frac{\partial M_{nt}}{\partial t}\right) = 0 \implies \left(\frac{\partial^3 w}{\partial n^3} + (2-\nu)\frac{\partial^3 w}{\partial n \partial t^2}\right)_{y=2\beta x} = 0 \qquad \text{(A1.15a)}$$

These differences between the boundary conditions used by Kaczkowski and those used in literature could drastically affect the coefficients of the displacement equation and the results. The inaccuracy of kaczkowski's solution may be partly due to the first order nature of his analysis.

The proposed solution is trigonometric in x and hyperbolic in y. This would give a displacement with periodicity in the x direction and exponential increase in the y direction. This seems inconsistent with the results from experiment and numerical simulation as well as basic physics models of vibration as all three of these show periodicity in both the x and y direction. Though it is true that certain combinations of hyperbolic functions reproduce periodicity, from these considerations it seems that any proposed solution should be trigonometric in nature.

The deflection function developed by Kaczkowski for a freely held plate can be expressed as

$$w(x,y) = \sum_{m=1,3,5,\ldots}^{\infty} \left[B_m \sinh\left(\sqrt{\left(\frac{m\pi}{a}\right)^2 + \sqrt{\frac{\rho\omega^2}{D}}}\, y \right) + D_m \sinh\left(\sqrt{\left(\frac{m\pi}{a}\right)^2 - \sqrt{\frac{\rho\omega^2}{D}}}\, y \right) \right] \sin\left(\frac{m\pi x}{a}\right) \qquad (2.13)$$

The function is only square root frequency dependent in the y direction. This combined with the hyperbolic nature in the y direction gives a deflection function that does not vary drastically with frequency as any plate vibration equation that describes the natural resonances should.

Conclusion

Kaczkowski proposed a novel approach to the derivation of the analytical expression of the transverse vibration of polygonal plates by using symmetric sections. The solution proposed works perfectly if the formulation of the differential equation of the transverse vibration and the boundary conditions is valid, but until now no one has compared the results from this solution to experimental results.

Closer inspection of the proposed solution results for a hexagon has shown that the results do not vary with frequency or approximate the different resonance modes of the hexagonal plate very accurately. The results from the analytical solution do not match well with the numerical FEM solution or the experimental ACURI solution. The reason for this may be due to several discrepancies found during the examination of Kaczkowski's solution formulation. The only part of the proposed solution that corresponds with the numerical model and the experimental results is the prediction of the fundamental frequency, which varies 22% from the numerical model and is only a first order approximation.

Even though Kaczkowski's solution has been widely accepted by the academic community the formulation and solution are inaccurate. More work needs to be done in the development of this analytical equation if this type of solution is to be used to accurately model the transverse vibration of regular polygonal shapes.

References

2.1. Leissa, A. W., "Vibration of Plates," NASA SP-160, 1969

2.2. Kaczkowski, Z., "Stabilität und Eigenschwingungen einer Platte von der Form eines regelmäßigen Polygons," 1961, Ingenieur-Archiv, Vol. 15, pp.103-109

2.3. Mansfield, E. H., "The Bending and Stretching of Plates," 1964, Pergamon Press Ltd., Oxford England

2.4. Timoshenko, S. P., Woinowsky-Krieger, S., "Theory of Plates and Shells," 1959, McGraw-Hill Book Company, Inc., New York

2.5. Timoshenko, S. P., Goodier, J. N., "Theory of Elasticity," 1970, McGraw-Hill Book Company, Inc., New York

2.6. Lévy, M. M., "Sur L'Équilibre Élastique d'une Plaque Rectangulaire," 1899, Comptes Rendus des Séances de L'Académie des Sciences, Vol. 129, pp. 535-539

2.7. Laurie, S. A., Vasiliev, V. V., "The Biharmonic Problem in the Theory of Elasticity," 1995, Gordon and Breach Publishers, ISBN 2-88449-054-X

2.8. Yu, Y. Y., "Vibrations of Elastic Plates," 1996, Springer-Verlag New York, Inc., ISBN 0-887-94514-8

2.9. Gorman, D. J., "Vibration Analysis of Plates by the Superposition Method," 1999, World Scientific Publishing Co. Pte. Ltd.

2.10. Soedel, W., "Vibrations of Shells and Plates," 2004, Marcel Dekker, New York

2.11. Qatu, M. S., "Vibrations of Laminated Shells and Plates," 2004, Elsevier Ltd.

CHAPTER 4.
ANSYS MODELING

Introduction

Finite Element Modeling (FEM) is a very useful and powerful tool for the numerical solution of a great many engineering problems. The problems range from deformation and stress analysis to wave propagation and composite analysis to fluid and heat flow. For this research, the FEM program ANSYS was used to numerically model the natural and forced vibrations of the multi-layer, multi-material composite discussed in Chapter 2 as well as the polygonal plate discussed in Chapter 3.

It is common practice, when modeling with FEM, to utilize the symmetry of the problem in order to reduce the complexity of the model and reduce the computation time. During the course of this research, the question arose of whether this common practice gives accurate results, when compared to a full model and to experiments.

This chapter describes the models used in Chapter 2 and Chapter 3 and presents the results from the analyses performed on the models. This chapter will also explore the accuracy of symmetric models.

Air-Coupled Ultrasonic Resonance Imaging Models

In this research several FE models have been made to numerically simulate the vibrational response of the different materials of the multi-layered, multi-material composite discussed in Chapter 2, as well as several different lay-ups. The specifics of each material and

the results of each model are described briefly below. The models are 4 inches from side to side.

The model for the SiC tile is made with the ANSYS element solid187. This element is a higher order 3-D, 10-node element with quadratic displacement behavior. The material has an elastic modulus of 428.28 GPa, a Poison's ratio of 0.166, and a density of 3058.4 Kg/m^3. The boundary conditions for this model are either fixed or free and are applied solely to the periphery of the hexagonal plate. Since the research in Chapter 2 deals with vibrations a modal analysis was performed to look at the natural resonance modes and frequencies of the hexagonal SiC tiles. Figures 3.1 and 3.2 show some of the resonance modes and frequencies extracted from the model with a modal analysis.

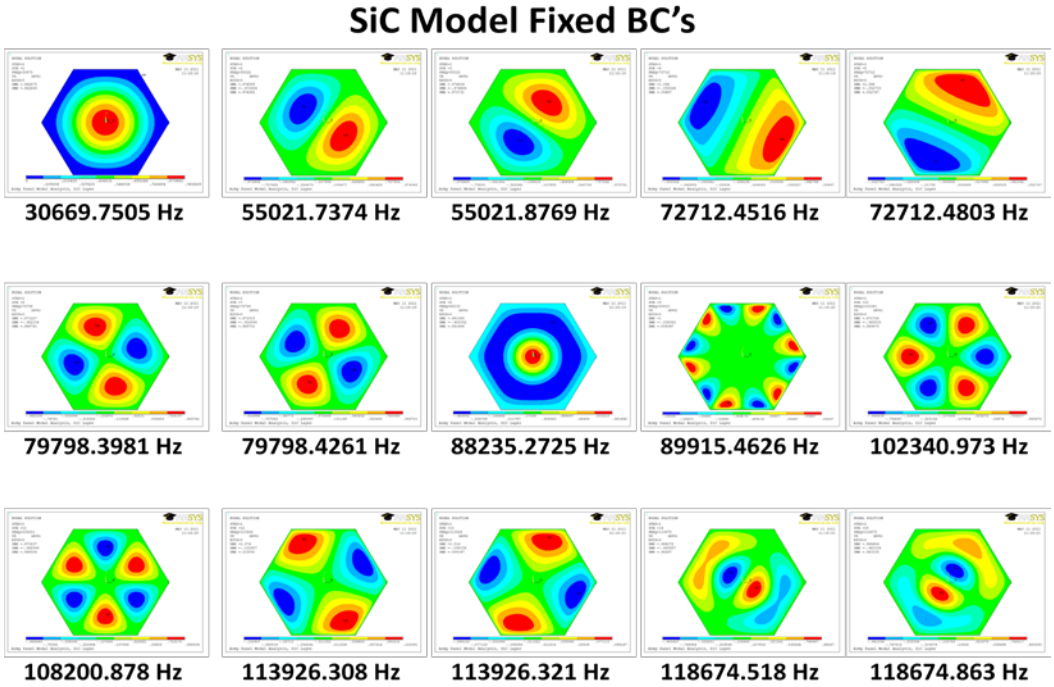

FIGURE 3.1. Here are the results from a modal analysis on the SiC model with fixed boundary conditions. There are several resonance images and corresponding resonance frequencies displayed.

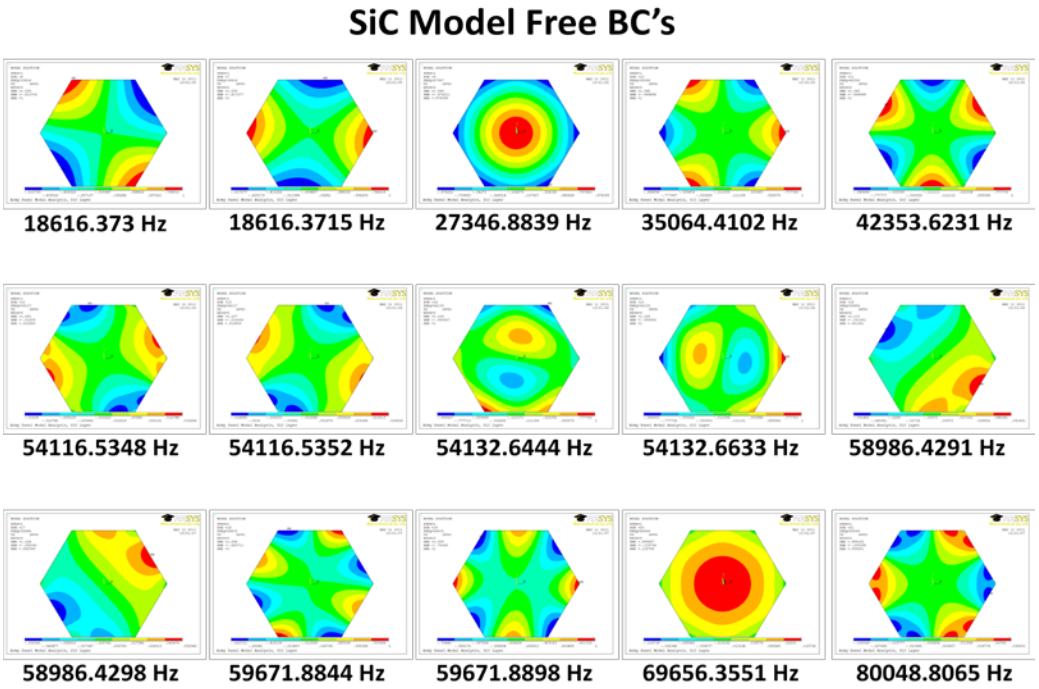

FIGURE 3.2. Here are the results from a modal analysis on the SiC model with free boundary conditions. There are several resonance images and corresponding resonance frequencies displayed.

There is a multitude of repeated resonance modes that appear in both the fixed and free models. A repeated resonance mode occurs when there is more than one mode with the same frequency to at least one decimal place. The resulting resonance patterns will be different, in this case the resonance pattern is rotated slightly, but the frequencies are the same. The resonant images from the fixed model correspond better with ACURI results from the bare SiC tile. This is not surprising because it is difficult to simulate a truly free boundary, also the boundary condition will be fixed, to some degree, inside any type of lay-up. Because of these two considerations, only fixed boundary conditions will be used in subsequent models.

The model for the Graphite-Carbon-Graphite (GCG) consists of three volumes, which are glued together so that the coincident areas become a single area. The center volume is exactly the same as the SiC model, and the other volumes have the same shape and size. The two outside volumes are models of the carbon-fiber/epoxy lay-up. These volumes are made

with the ANSYS element solid185. This element is a 3-D, 8-node element with layered structure capabilities. The material has a density of 1580.0 Kg/m^3 and the following physical properties:

$$E_x = 181\ GPa \quad E_y = 10.3\ GPa \quad E_z = 10.3\ GPa$$
$$\nu_{xy} = 0.15 \quad \nu_{yz} = 0.10 \quad \nu_{xz} = 0.15$$
$$G_{xy} = 5.50\ GPa \quad G_{yz} = 6.41\ GPa \quad G_{xz} = 5.50\ GPa$$

There are 24 layers and the thickness of each layer is approximately 132 μm. The fiber direction follows the lay-up $[\ [0,+45,90,-45]_3\ ]_{sym}$. Fixed boundary conditions are applied solely to the periphery of the hexagonal plate. Figure 3.3 shows some of the resonance modes and frequencies extracted from the model with a modal analysis.

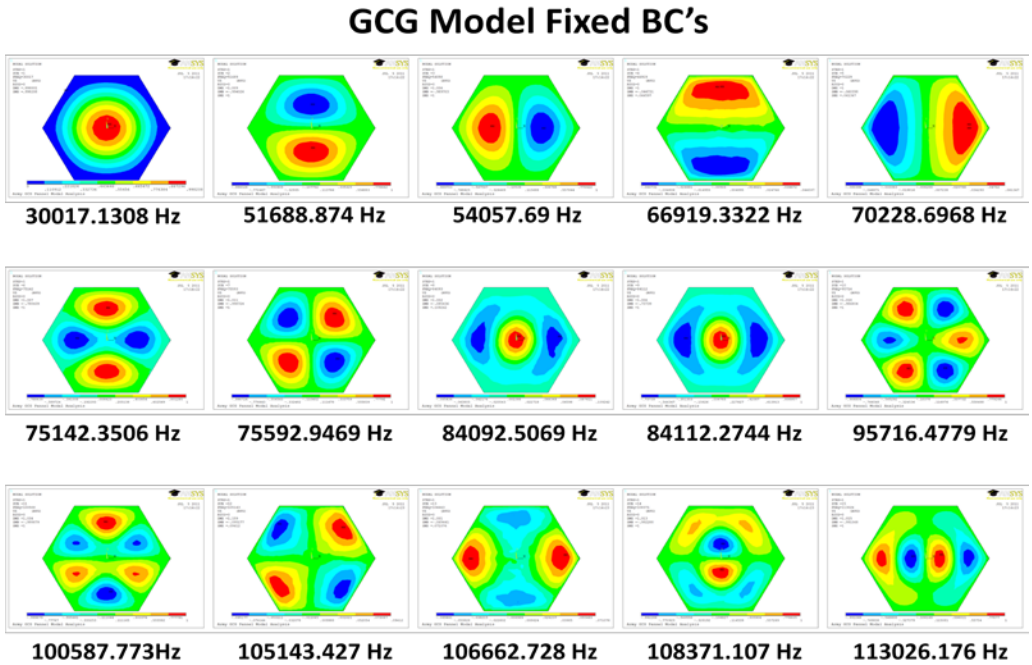

FIGURE 3.3. Here are the results from a modal analysis on the GCG model with fixed boundary conditions. There are several resonance images and corresponding resonance frequencies displayed.

The same resonance modes appear in this modal extraction as appeared in the SiC modal extraction. This indicates that the SiC tile is the strongest vibrator of the three layers and that it either overpowers the other two volumes or damps out their vibrations. There are some important differences, however. Many of the resonance patterns appear with a slightly smaller amplitude and the resonant frequencies have shifted downward. All of this is to be expected from the damping characteristics of adding layers to the SiC tile. Also note that the repeated resonances from the SiC model are now separated.

The model for the full lay-up consists of five volumes which are glued together so that the coincident areas become a single area. Two volumes are added to the GCG model; a rubber layer right next to the GCG and a S2 glass-fiber/epoxy layer next to the rubber layer. The rubber volume is made with the ANSYS element solid187. This is the same as the element used for the SiC layer and allows for large deflection. The material has the following generic rubber properties: an elastic modulus of 2.412 MPa, a Poison's ratio of 0.33, and a density of 1079 Kg/m^3. The S2 glass-fiber/epoxy volume is made with the ANSYS element solid185, which is the same element used for the carbon-fiber/epoxy layers. The material has a density of 2000.0 Kg/m^3 and the following physical properties:

$$E_x = 55\ GPa \quad E_y = 16\ GPa \quad E_z = 16\ GPa$$
$$\nu_{xy} = 0.28 \quad \nu_{yz} = 0.10 \quad \nu_{xz} = 0.28$$
$$G_{xy} = 7.6\ GPa \quad G_{yz} = 4.52\ GPa \quad G_{xz} = 7.6\ GPa$$

There are 96 layers and the thickness of each layer is approximately 132 μm. The fiber direction follows the lay-up $[\,[\,[\,[0,+45,90,-45]_3\,]_{sym}\,]_{sym}]_{sym}$. Fixed boundary conditions are applied solely to the periphery of the hexagonal plate. Figures 3.4 and 3.5 show some of the resonance modes and frequencies extracted from the model with a modal analysis.

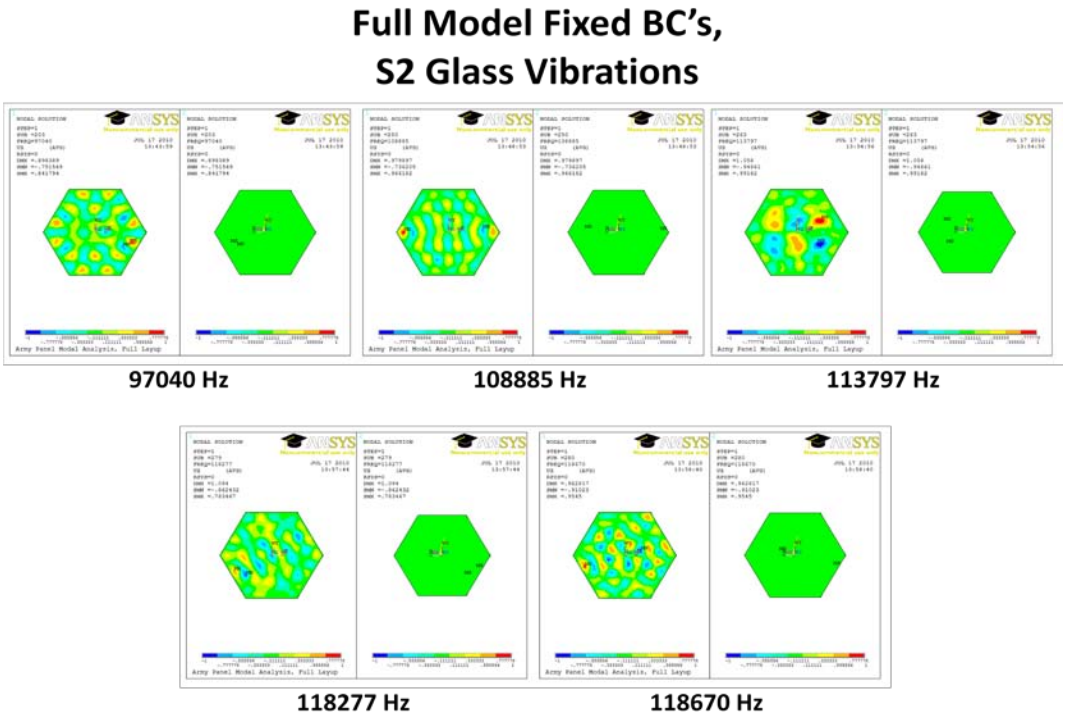

FIGURE 3.4. Here are the results from a modal analysis on the Full Lay-up Model with fixed boundary conditions. There are several resonance images and corresponding resonance frequencies displayed. Here only the S2 glass layer is vibrating.

In both of these figures, the left side of each image is the S2 glass-fiber/epoxy side of the full model and the right side of each image is the GCG side of the full model. The images of the modal results in Fig. 3.4 indicate that only the S2 glass-fiber/epoxy layer vibrates while only the GCG section vibrates in the images of Fig. 3.5. This indicates that the rubber layer acts like an impedance layer and effectively separates the vibrations from the S2 glass-fiber/epoxy layer and the GCG section. The same resonance modes appear in this modal extraction as appeared in the SiC modal extraction, but the resonance images are slightly damped and the frequencies are shifted slightly. Several of the resonance images in Fig. 3.5 match well with the ACURI results (Fig. 3.6) which indicates that both the rubber layer and the S2 glass-fiber/epoxy layer only act as damping layers to the SiC Tile vibration and do not add resonance patterns to the resulting resonance images during ACURI scanning.

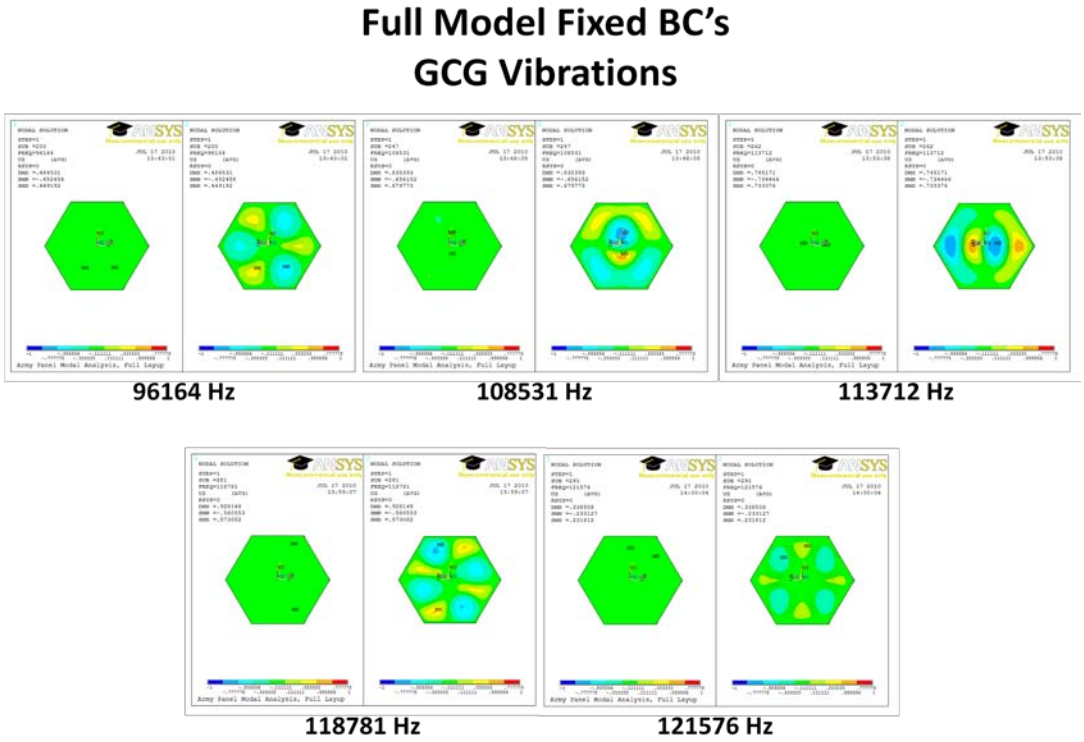

FIGURE 3.5. Here are the results from a modal analysis on the Full Lay-up Model with fixed boundary conditions. There are several resonance images and corresponding resonance frequencies displayed. Here only the GCG layer is vibrating.

In order to test the accuracy of these FE models matches between the ACURI scan results and the modal results of the SiC model were made. Fig. 3.6 shows several matches made between the ACURI and FEM modal results. Several of the ACURI images can be directly matched with a single FEM mode at a frequency close to the center frequency and within the bandwidth of the transducer. Other of the ACURI images require a superposition of FEM modes in order to make a match. These results indicate that the FE model accurately describes the behavior of the SiC tile.

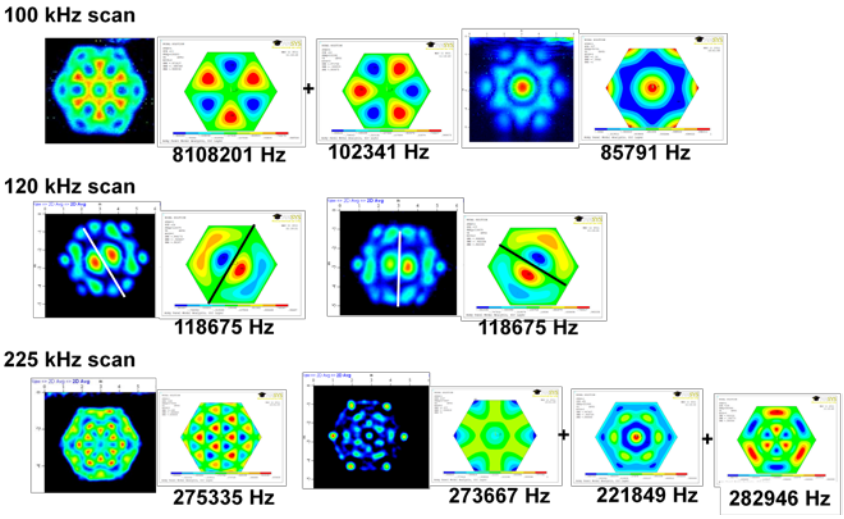

FIGURE 3.6. Matching resonance images from ACURI and FEM modal results.

Kaczkowski Plate Section Model

The model for the plate section is made with the ANSYS element solid187. This element is a higher order 3-D, 10-node element with quadratic displacement behavior. The model is roughly 2 in by 1.5 in by 0.75 in. The material has an elastic modulus of 428.28 GPa, a Poison's ratio of 0.166, and a density of 3058.4 Kg/m^3. The boundary conditions for this model are either fixed or free for the exterior edge of the plate section and symmetric or antisymmetric on the interior edges. Since the research in Chapter 2 deals with natural vibrations a modal analysis was performed to look at the natural resonance modes and frequencies of the polygonal plate section. Figures 3.7 and 3.8 show some of the resonance modes and frequencies extracted from the model with a modal analysis.

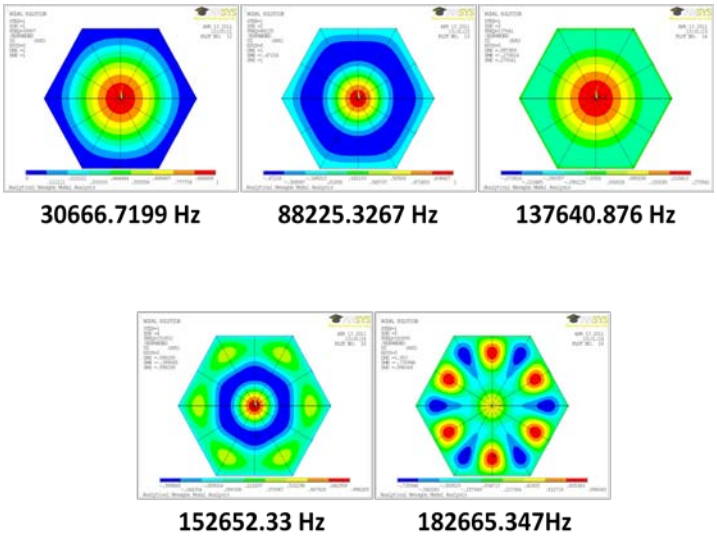

FIGURE 3.7. FEM modal results for a 1/12 section of the hexagonal plate with fixed external boundary.

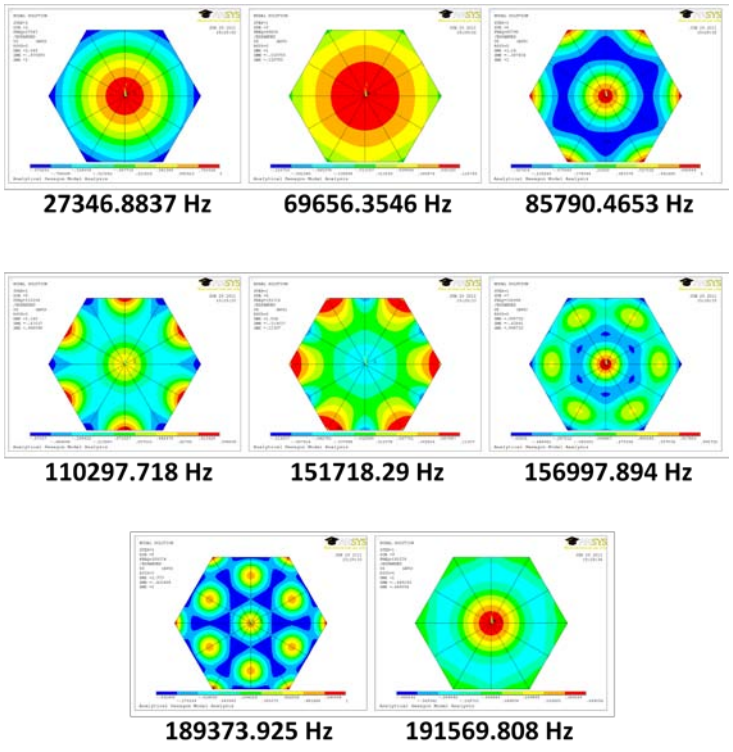

FIGURE 3.8. FEM modal results for a 1/12 section of the hexagonal plate with free external boundary.

Symmetric Modeling

The model for the material considered in this study is complex with a large number of nodes. Models of anything larger than a full lay-up the same shape and size as one of the hexagonal tiles with an appropriately small mesh size are simply too large to analyze easily. Modal and harmonic analyses are very simple analyses that usually take no time at all to run. With the full lay-up this simple analysis can take hours. A more complex analysis, such as a waveform impingement, will take much longer. An analysis of this type was performed using a computer cluster on a symmetric quarter of the SiC tile model. Even with this small model and a relatively coarse mesh, the analysis took four days to complete. It is because of these considerations; namely the complexity of modeling multiple layers and several tiles at a time, the complex analyses, and the long computation time, that the validity of symmetric modeling was considered.

In order to test the accuracy of modeling with symmetric sections two different polygonal plates, a square and a hexagon, were divided along the symmetry lines of the polygons as shown in Fig 3.9 and Fig 3.10. All possible symmetric sections are considered in this analysis. The sections of the polygons are subjected to a modal analysis and a harmonic analysis and the results compared to the results of the full models. A modal analysis shows the natural resonance modes and frequencies of the models. Comparing the natural resonances of the plate sections to those of the full plate will determine whether the plate sections have the same behavior as the full plate. The harmonic analysis will show the response of the model to a sine input at specific frequencies. Comparing the responses of the plate sections to the response of the full plate will determine whether the plate sections respond to a given impingement in

the same manner as a full plate. These two analyses can indicate whether a symmetric model can be used to recreate a full model without loss of accuracy.

The boundary conditions on the plate periphery and on the corresponding areas of the plate sections are either fixed (zero x,y, and z displacement) or free (no constraints). For the areas of the plate sections that would normally be in the interior of the full plate (interior areas) the possible boundary conditions are symmetric and antisymmetric. For a mathematical explanation of these boundary conditions see Appendix A.2. Combinations of the symmetric and antisymmetric boundary conditions on the interior areas of the plate sections should replicate all possible interactions that occur in the interior of the full plate.

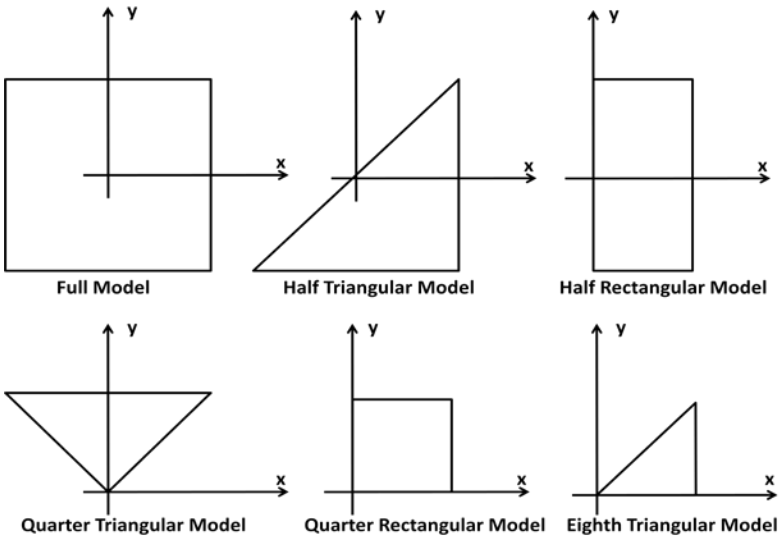

FIGURE 3.9. Square plate and possible symmetric sections.

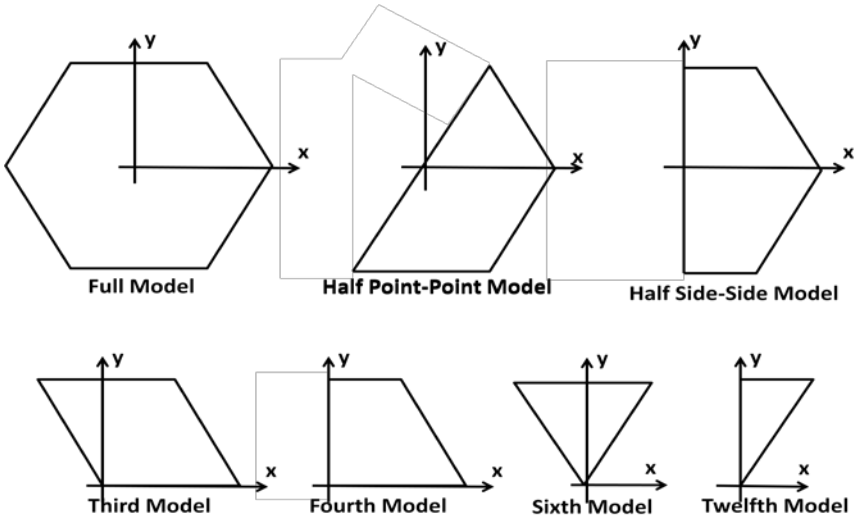

FIGURE 3.10. Hexagonal plate and possible symmetric sections.

All of the full plate ANSYS models created for this analysis are approximately 4 inches in length from side to side and 0.75 inches thick, and the symmetric section models are sized relative to the full model. The element type and material properties are the same as those listed for the SiC tile model described under the Air-Coupled Ultrasonic Resonance Imaging Models section.

Modal Analysis

A modal analysis of the plates and plate sections extracts the natural modes of the models for the given material and boundary conditions. The extracted modes were visually compared and like modes were grouped together.

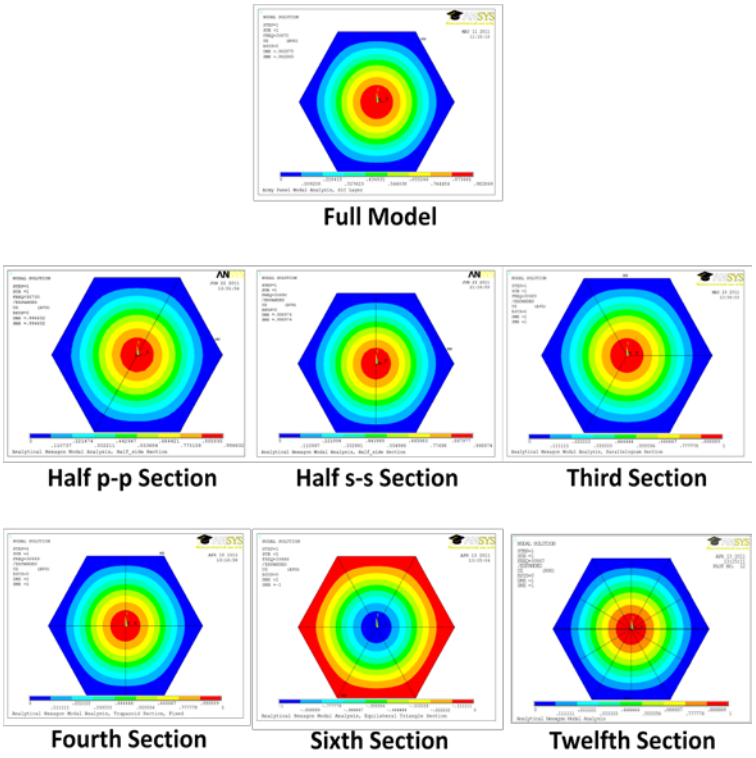

FIGURE 3.11. A comparison of the natural resonance modes of symmetry models to the resonance mode of the full plate model. A) Full Plate Model @ 30670 Hz. B) Half point-point Section Model @ 30700 Hz. C) Half side-side Section Model @ 30690 Hz. D) One Third Section Model @ 30669 Hz. E) One Fourth Section Model @ 30669 Hz. F) One Sixth Section Model @ 30668 Hz. G) One Twelfth Section Model @ 30667 Hz.

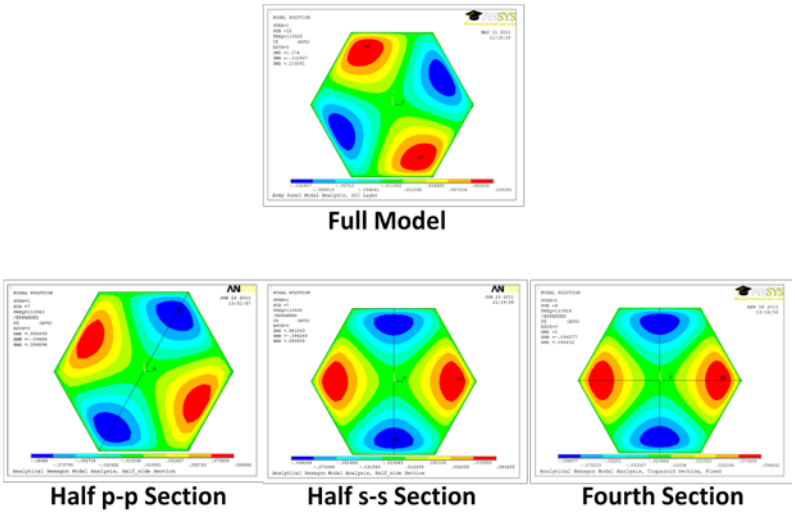

FIGURE 3.12. A comparison of the natural resonance modes of symmetry models to the resonance modes of the full plate model. A) Full Plate Model @ 113926 Hz. B) Half point-point Section Model @ 113943 Hz. C) Half side-side Section Model @113935 Hz. D) One Fourth Section Model @ 113926 Hz.

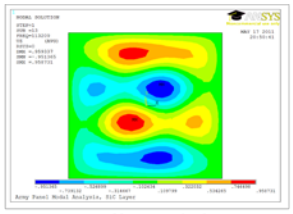

FIGURE 3.13. A comparison of the natural resonance modes of symmetry models to the resonance modes of the full plate model. A) Full Plate Model @ 113209 Hz. B) Half Triangular Section Model @ 113911 Hz. C) Half Rectangular Section Model @ 113116 Hz. D) One Fourth Rectangular Section Model @ 112939 Hz.

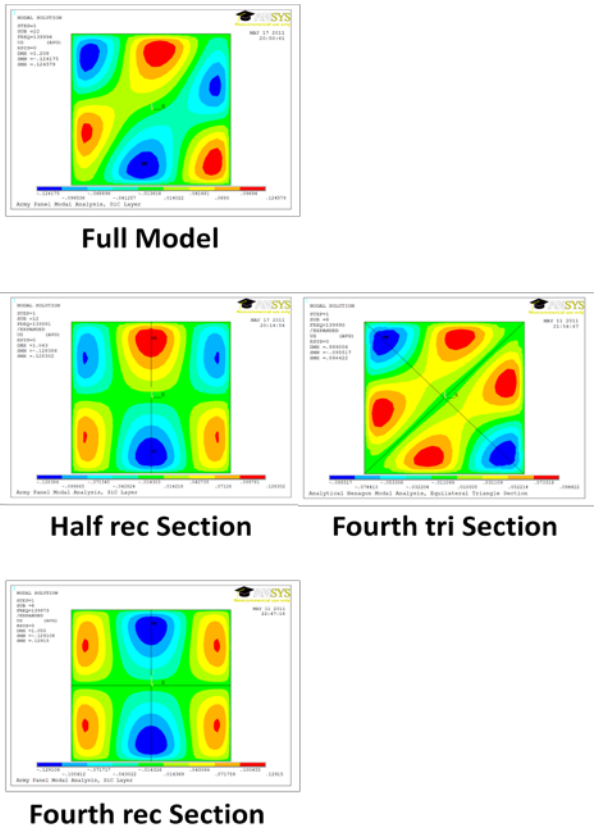

FIGURE 3.14. A comparison of the natural resonance modes of symmetry models to the resonance modes of the full plate model. A) Full Plate Model @ 139994 Hz. B) Half Triangular Section Model @ 140033 Hz. C) Half Rectangular Section Model @ 139991 Hz. D) One Fourth Triangular Section Model @ 139990 Hz. E) One Fourth Rectangular Section Model @ 139973 Hz.

The matching of resonance modes was performed by looking for distinctive features, such as high and low amplitude regions, in the resonance images of the full plate model and each symmetry model. The size, shape, and locations of these distinctive features were then compared to match the resonance images. It is important to keep in mind that in this FE analysis red is positive displacement and blue is negative displacement, but in a sinusoidal vibration positive and negative displacement change positions cyclically. Hence the blue and red colors can be interchanged; they essentially represent the maxima in a resonance image.

Figures 3.11 through 3.14 demonstrate how the extracted modes are compared and grouped. The comparisons made in Figures 3.11 and 3.12 were relatively easy to make when small discrepancies such as color variation and rotation of the resonance pattern were taken into account. The comparisons in Figures 3.13 and 3.14, on the other hand, were somewhat more difficult to make as not only were there color variations and rotations to consider but some of the maximas have changed position slightly due to the constraints of the geometry of a given plate section.

The frequency range of this study was from 0-300 kHz. This was chosen to capture both the fundamental frequencies and frequencies where ACURI can operate. For the sake of brevity, the tables below list only the natural resonance modes between 0 and 100 kHz. The resonance modes of the full plate model are listed by frequency and all the corresponding resonance modes from the plate sections are listed for each full plate resonance long with the specific model and the interior boundary conditions.

Hexagon Resonance Modes, Fixed BC			
Full Model	Symmetric Models		
Frequency (Hz)	Frequency (Hz)	Model	Interior BC's
30669.7505			
	30700.3255	half p-p	sym
	30690.1668	half s-s	sym
	30669.3626	third	sym-sym
	30669.3918	fourth	sym-sym
	30668.3595	sixth	sym-sym
	30666.7199	twelfth	sym-sym
55021.7374			
	55103.0331	half p-p	antisym
	55064.9021	half s-s	sym
	55018.6634	fourth	sym-antisym
55021.8769			
	55097.6985	half p-p	sym
	55080.0526	half s-s	antisym
	55024.2001	fourth	antisym-sym
75712.4516			
	72720.445	half p-p	antisym
	72716.6723	half s-s	sym
	72712.0422	fourth	sym-antisym
72712.4803			
	72719.642	half p-p	sym
	72718.2008	half s-s	antisym
	72712.7531	fourth	antisym-sym
79798.3981			
	79944.816	half p-p	antisym
	79904.0709	half s-s	antisym
	79799.4161	fourth	antisym-antisym
79798.4261			
	79944.6592	half p-p	sym
	79879.0981	half s-s	sym
	79798.0312	fourth	sym-sym
88235.2725			
	88414.5946	half p-p	sym
	88356.0798	half s-s	sym
	88233.9126	third	sym-sym
	88235.5451	fourth	sym-sym

	88231.1792	sixth	sym-sym
	88225.3267	twelfth	sym-sym
89915.4626			
	89917.7606	half p-p	antisym
	89916.8434	half s-s	antisym
	89915.4577	third	antisym-antisym
	89915.4912	fourth	antisym-antisym
	89915.4382	sixth	antisym-antisym
	89915.4305	twelfth	antisym-antisym

TABLE 3.1. Table of resonance frequencies between 0 and 100 kHz for a hexagonal plate with fixed boundary conditions and matched frequencies of symmetric models.

Hexagon Resonance Modes, Free BC			
Full Model	Symmetric Models		
Frequency (Hz)	Frequency (Hz)	Model	Interior BC's
18616.373			
	18619.9092	half p-p	sym
	18618.8201	half s-s	sym
	18616.4489	fourth	sym-sym
18616.3715			
	18620.4733	half p-p	antisym
	18618.1244	half s-s	antisym
	18616.3804	fourth	antisym-antisym
27346.8839			
	27350.1151	half p-p	sym
	27349.093	half s-s	sym
	27346.8937	third	sym-sym
	27346.9318	fourth	sym-sym
	27346.8909	sixth	sym-sym
	27346.8837	twelfth	sym-sym
35064.4102			
	35083.5299	half p-p	sym
	35075.125	half s-s	antisym
	35064.3862	third	sym-sym
	354.599806	fourth	antisym-sym
	35064.3812	sixth	sym-sym
	35064.0982	twelfth	sym-antisym
42353.6231			

	42364.6056	half p-p	antisym
	42359.4873	half s-s	sym
	42353.6163	third	antisym-antisym
	42653.7621	fourth	sym-antisym
	42353.6449	sixth	antisym-antisym
	42353.6087	twelfth	antisym-sym
54116.5348			
	54116.8813	half p-p	antisym
	54116.7333	half s-s	antisym
	54116.5405	fourth	antisym-antisym
54116.5352			
	54116.8924	half p-p	sym
	54116.7579	half s-s	sym
	54116.5388	fourth	sym-sym
54132.6444			
	54154.5037	half p-p	antisym
	54148.2321	half s-s	sym
	54132.867	fourth	sym-antisym
54132.6633			
	54155.0178	half p-p	sym
	54147.8749	half s-s	antisym
	54132.8515	fourth	antisym-sym
58986.4291			
	58987.3549	half p-p	antisym
	58987.0318	half s-s	sym
	58986.4393	fourth	sym-antisym
58986.4298			
	58987.3534	half p-p	sym
	58986.9903	half s-s	antisym
	58986.4445	fourth	antisym-sym
59671.8844			
	59708.5694	half p-p	sym
	596954.6375	half s-s	sym
	59672.1037	fourth	antisym-antisym
59671.8898			
	59712.5782	half p-p	antisym
	59691.9689	half s-s	antisym
	59672.6776	fourth	sym-sym
69656.3551			

	69656.495	half p-p	sym
	69656.4419	half s-s	sym
	69656.3552	third	sym-sym
	69656.3568	fourth	sym-sym
	69656.3541	sixth	sym-sym
	69656.3546	twelfth	sym-sym
80048.8065			
	80052.1805	half p-p	sym
	80050.9068	half s-s	antisym
	80048.8238	third	sym-sym
	80048.8591	fourth	antisym-sym
	80048.7882	sixth	sym-sym
	80048.7413	twelfth	sym-antisym
84360.8609			
	84438.4958	half p-p	sym
	84402.0214	half s-s	antisym
	84362.2506	fourth	antisym-sym
84360.9537			
	84438.515	half p-p	antisym
	84402.8692	half s-s	sym
	84361.8734	fourth	sym-antisym
84636.7707			
	84639.668	half p-p	antisym
	84638.5617	half s-s	sym
	84636.7706	third	antisym-antisym
	84636.7973	fourth	sym-antisym
	84636.752	sixth	antisym-antisym
	84636.7121	twelfth	antisym-sym
84987.2839			
	85050.6614	half p-p	antisym
	85031.8971	half s-s	antisym
	84988.1029	fourth	antisym-antisym
84987.3289			
	85052.1805	half p-p	sym
	85031.059	half s-s	sym
	84988.0893	fourth	sym-sym
85791.0826			
	85863.1278	half p-p	sym
	85842.007	half s-s	sym

	85790.8721	third	sym-sym
	85791.7468	fourth	sym-sym
	85790.9244	sixth	sym-sym
	85790.4653	twelfth	sym-sym
87722.195			
	877251353	half p-p	sym
	87724.0727	half s-s	sym
	87722.2293	fourth	sym-sym
87722.1897			
	87725.298	half p-p	antisym
	87723.9262	half s-s	antisym
	87722.2211	fourth	antisym-antisym

TABLE 3.2. Table of resonance frequencies between 0 and 100 kHz for a hexagonal plate with free boundary conditions and matched frequencies of symmetric models.

Several observations can be made about the hexagonal models from the data presented in the tables above.

1. Every single resonance mode in the full plate model can be replicated with the symmetry models.
2. The frequencies of the resonance modes from the symmetry models have a variance from the resonance frequencies of the full plate that is less than 0.3% of the resonance frequency. This means the symmetry models accurately replicate both the resonance pattern and the resonance frequency of the full plate.
3. For the symmetry conditions sym-antisym and antisym-sym, with both the fixed and free boundary conditions, the resonance images of the one sixth and the one third models do not appear among the resonance images of the full model.
4. Of all of the symmetric models, only the half models have resonance modes that match with every single resonance mode of the full model. This means that attempting to model a structure with symmetry models any smaller than one half the size of the full

model will not give a full solution. This is due to the fact that a smaller model cannot model the combinations of interior boundary conditions that occur in a full model. This is shown in Fig 3.15 below. Observe the symmetry conditions on the symmetry lines of the full plate specified when using a small symmetry model (in this case a one twelfth model). Changing the condition on just one of the lines of symmetry yields a possibility that the small symmetry model cannot duplicate but that can be modeled with a larger symmetry model (1/2 or 1/4) or the full model itself.

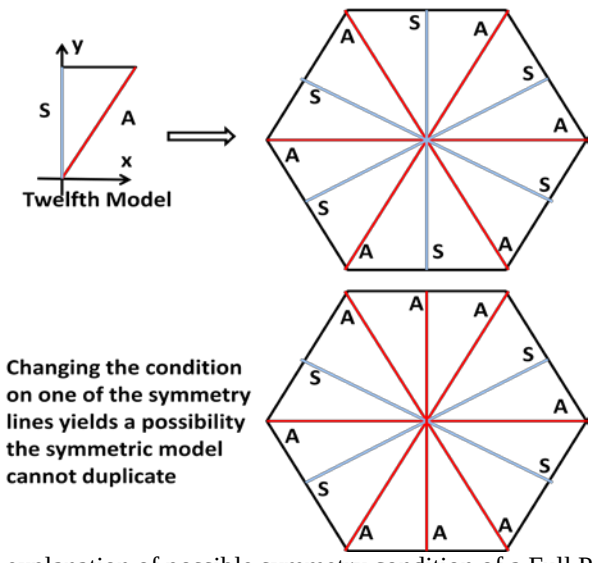

FIGURE 3.15. A graphical explanation of possible symmetry condition of a Full Plate Model where the lines represent symmetry lines. The blue lines are symmetric and the red lines are antisymmetric. A) 1/12 section with symmetric-antisymmetric boundaries. B) The 1/12 section mirrored symmetrically into a full plate. C) Possible interior boundary conditions of a Full Plate.

5. Both the half point-point model and the half side-side model have resonance modes that match the resonance modes of the full model but both of the interior boundary conditions (symmetric and antisymmetric) must be used. This means that the idea of using a smaller symmetric model to reduce the computation time is faulty since two of the half models will have to be run to replicate the results from an analysis of the full

model. This is true at least for this type of analysis. If an analysis was required in which only a symmetric interior boundary need be considered, then a half model would reduce the computation time.

It seems that the best model, both for accuracy and computation time, for the hexagonal plate is the Full Plate model.

Square Resonance Modes, Fixed BC			
Full Model	**Symmetric Models**		
Frequency (Hz)	**Frequency (Hz)**	**Model**	**Interior BC's**
28840.8035			
	28908.5353	**half tri**	**Sym**
	28834.616	**half rec**	**Sym**
	28834.8514	**fourth tri**	**sym-sym**
	28810.4538	**fourth rec**	**sym-sym**
	28819.842	**Eighth**	**sym-sym**
51511.8833			
	51511.1326	**half rec**	**Antisym**
	51441.4541	**fourth rec**	**antisym-sym**
51512.6166			
	51487.7026	**half rec**	**Sym**
	51440.5873	**fourth rec**	**sym-antisym**
69096.9259			
	69097.1229	**half rec**	**Antisym**
	69091.2126	**fourth rec**	**antisym-sym**
69097.1031			
	69094.8371	**half rec**	**Sym**
	69091.0701	**fourth rec**	**sym-antisym**
69847.0634			
	70119.8839	**half tri**	**Sym**
	69836.3458	**half rec**	**Antisym**
	69823.5377	**fourth tri**	**sym-sym**
	69746.0942	**fourth rec**	**antisym-antisym**
	69767.0002	**Eighth**	**antisym-sym**
80197.0795			

	80592.1918	half tri	Antisym
	80162.8529	half rec	Sym
	80166.4387	fourth tri	antisym-antisym
	80041.9618	fourth rec	sym-sym
	80069.4801	Eighth	sym-antisym
81222.6659			
	81597.0163	half tri	Sym
	81202.6928	half rec	Sym
	81079.1823	fourth rec	sym-sym
	81186.2997	fourth tri	sym-sym
	81115.2768	Eighth	sym-sym
86738.4232			
	86741.9071	half tri	Antisym
	86738.0156	half rec	Antisym
	86737.8797	fourth tri	antisym-antisym
	86736.3265	fourth rec	antisym-antisym
	86737.782	Eighth	antisym-antisym
95544.3988			
	95869.8707	half tri	Sym
	95536.8782	half rec	Sym
	95519.516	fourth tri	antisym-sym
	95377.898	fourth rec	sym-antisym
95550.2627			
	96212.4797	half tri	Antisym
	95528.0827	half rec	Antisym
	95509.9986	fourth tri	sym-antisym
	95376.5839	fourth rec	antisym-sym

TABLE 3.3. Table of resonance frequencies between 0 and 100 kHz for a square plate with fixed boundary conditions and matched frequencies of symmetric models.

Square Resonance Models, Free BC			
Full Model	Symmetric Models		
Frequency (Hz)	Frequency (Hz)	Model	Interior BC's
13125.0478			
	13137.9604	half tri	Sym
	13124.1726	half rec	Antisym
	13124.0035	fourth tri	sym-sym
	13121	fourth rec	antisym-antisym

	13120.9022	eighth	antisym-sym
19253.5843			
	19259.2258	half tri	Antisym
	19253.56	half rec	Sym
	19253	fourth tri	antisym-antisym
	19252.3477	fourth rec	sym-sym
	19247.0786	eighth	sym-antisym
21475.3778			
	21483.3875	half tri	Sym
	21475.2961	half rec	Sym
	21474.9901	fourth tri	sym-sym
	21473.5668	fourth rec	sym-sym
	21473.8388	eighth	sym-sym
30569.9849			
	30621.2278	half tri	Antisym
	30569.5954	half rec	Sym
	30567.5506	fourth tri	sym-antisym
	30560.0403	fourth rec	sym-antisym
30570.4431			
	30594.932	half tri	Sym
	30567.3163	half rec	Antisym
	30567.4681	fourth tri	antisym-sym
	30560.0247	fourth rec	antisym-sym
47394.8394			
	47395.2907	half tri	Sym
	47394.7932	half rec	Antisym
	47394.8115	fourth tri	sym-sym
	47395	fourth rec	antisym-antisym
	47384.9207	eighth	antisym-sym
48480.8517			
	48480.8078	half rec	Antisym
	48480.5894	fourth rec	antisym-sym
48480.8765			
	48480.8254	half rec	Sym
	48480.5894	fourth rec	sym-antisym
48782.6398			
	48780.4983	half rec	Antisym
	48769.8338	fourth rec	antisym-sym
48783.3643			

	48780.6333	half rec	Sym
	48769.8214	fourth rec	sym-antisym
50549.2038			
	50652.3	half tri	Sym
	50545.5822	half rec	Sym
	50542.5802	fourth tri	sym-sym
	50522.7034	fourth rec	sym-sym
	50528.1003	eighth	sym-sym
53931.7643			
	53931.9833	half tri	Antisym
	53931.7474	half rec	Sym
	53932	fourth tri	antisym-antisym
	53931.6636	fourth rec	sym-sym
	53902.5021	eighth	sym-antisym
54475.3399			
	54583.0686	half tri	Antisym
	54470.0764	half rec	Antisym
	54470	fourth tri	antisym-antisym
	54450	fourth rec	antisym-antisym
	54455	eighth	antisym-antisym
58104.2338			
	58208.2665	half tri	Sym
	58100.6492	half rec	Antisym
	58098.4384	fourth tri	sym-sym
	58080	fourth rec	antisym-antisym
	58081.953	eighth	antisym-sym
58156.7116			
	58157.584	half tri	Anisym
	58156.6564	half rec	Sym
	58157	fourth tri	antisym-antisym
	58156.3307	fourth rec	sym-sym
	58148.6589	eighth	sym-antisym
62591.291			
	62591.4391	half tri	Sym
	62591.2842	half rec	Sym
	62591.2878	fourth tri	sym-sym
	62591.2447	fourth rec	sym-sym
	62591.2525	eighth	sym-sym
74681.4437			

	74848.1448	half tri	Sym
	74674.5888	half rec	Sym
	74671.9474	fourth tri	antisym-sym
	74627.0347	fourth rec	sym-antisym
74682.9791			
	74954.1332	half tri	Antisym
	74676.0474	half rec	Antisym
	74668.3296	fourth tri	sym-antisym
	74627.0747	fourth rec	antisym-sym
75361.7414			
	75361.3942	half rec	Antisym
	75360.282	fourth rec	antisym-sym
75361.7652			
	75361.468	half rec	Sym
	75360.2799	fourth rec	sym-antisym
81560.6294			
	81739.1611	half tri	Antisym
	81554.8963	half rec	Sym
	81549	fourth tri	antisym-antisym
	81514.0965	fourth rec	sym-sym
	81513.5414	eighth	sym-antisym
83483.0954			
	83667.2195	half tri	Sym
	83477.3177	half rec	Sym
	83469.4256	fourth tri	sym-sym
	83433.4492	fourth rec	sym-sym
	83441.5059	eighth	sym-sym
85604.5706			
	85617.1737	half tri	Antisym
	85603.5556	half rec	Antisym
	85605	fourth tri	antisym-antisym
	85600	fourth rec	antisym-antisym
	85601	eighth	antisym-antisym
88067.8954			
	88304.0052	half tri	Sym
	88061.6559	half rec	Sym
	88058.3053	fourth tri	antisym-sym
	88010.3732	fourth rec	sym-antisym
88069.9365			

	88333.5406	**half tri**	**Antisym**
	88065.6762	**half rec**	**Antisym**
	88057.7387	**fourth tri**	**sym-antisym**
	88010.3101	**fourth rec**	**antisym-sym**
98300.806			
	98698.5347	**half tri**	**Sym**
	98284.9238	**half rec**	**Antisym**
	98275.7085	**fourth tri**	**sym-sym**
	98193	**fourth rec**	**antisym-antisym**
	98210.2637	**eighth**	**antisym-sym**
99301.1668			
	99300.0083	**half rec**	**Antisym**
	99295.0079	**fourth rec**	**antisym-sym**
99301.2124			
	99299.903	**half rec**	**Sym**
	99295.0052	**fourth rec**	**sym-antisym**

TABLE 3.4. Table of resonance frequencies between 0 and 100 kHz for a square plate with free boundary conditions and matched frequencies of symmetric models.

Several observations can be made about the square models from the data presented in the tables above.

1. Every single resonance mode in the Full Plate model can be replicated with the symmetry models.
2. The frequencies of the resonance modes from the symmetry models have a variance from the resonance frequency of the full plate that is between ~0% and 1% of the resonance frequency. Also, Fig 3.13 and Fig 3.14 show several cases where the resonance patterns of the full square plate and the patterns of the symmetry models where very difficult to match. This means the symmetry models do a decent but flawed job of replicating both the resonance patterns and the resonance frequencies of the full plate.

3. A multitude of resonance modes from several of the symmetric models with both fixed and free boundary conditions do not appear among the resonance modes of the full plate model.
4. Of all of the symmetric models only the half rectangular model has resonance modes that match every resonance mode of the full plate model. This means that only the half rectangular model could potentially be used to reduce the model complexity without a significant loss of fidelity.
5. Only by using both of the interior boundary conditions (symmetry and antisymmetry) on the half rectangular model can all of the resonance modes of the full plate model be matched. This means that the idea of using a smaller symmetric model to reduce the computation time is faulty since two of the half models will have to be run to replicate the results from an analysis of the full model. This is true at least for this type of analysis. If an analysis was required in which only a symmetric interior boundary need be considered, then a half model would reduce the computation time.

It seems that the best model, both for accuracy and computation time, for the hexagonal plate is the Full Plate model.

Harmonic Analysis

A harmonic analysis applies a pressure or force that varies sinusoidally with time at a specific forcing frequency and extracts the results of a forced vibration. For this particular analysis the Gaussian pressure distribution described in Fig 3.15 is applied to the models. The pressure distribution is centered on the origin of all of the models.

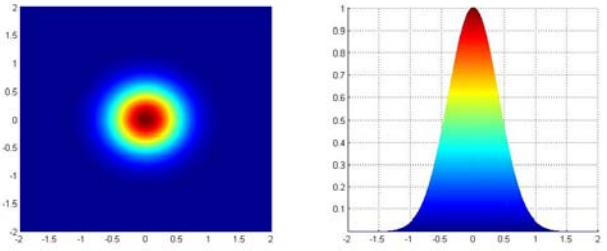

FIGURE 3.16. 2D Gaussian pressure distribution applied to the harmonic models.

This analysis was performed with 37 distinct frequencies ranging between 80 and 300 kHz and the results for the first frequency is shown in Fig. 3.17-3.20.

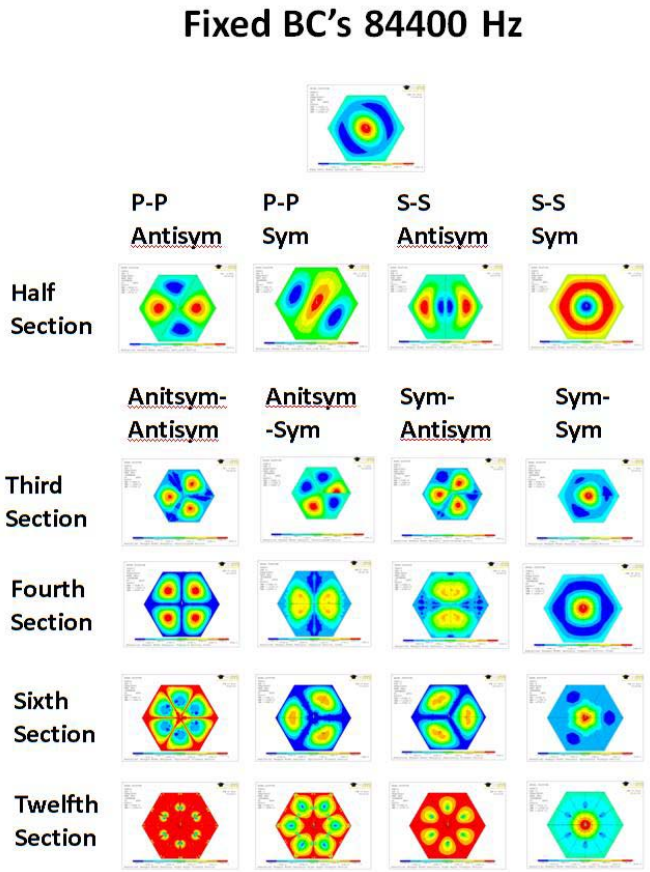

FIGURE 3.17. Harmonic results for the full plate and all of the symmetric sections with fixed boundary conditions and a frequency of 84400 Hz.

Since this analysis is a forced response it is not enough that the results from the symmetric sections match decently or closely with the results from the full plate, they must match very

closely or exactly in order for symmetric modeling to be considered valid. If the symmetric sections cannot replicate the forced response of a full model then they cannot be used to accurately model a structure and its responses to stimuli.

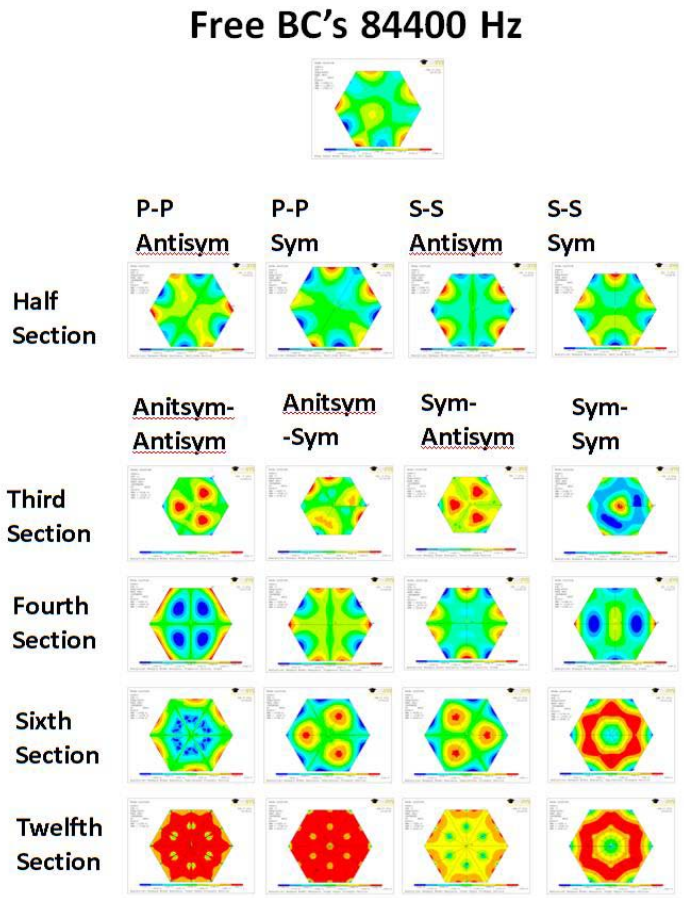

FIGURE 3.18. Harmonic results for the full plate and all of the symmetric sections with free boundary conditions and a frequency of 84400 Hz.

The results from the harmonic analysis performed on the hexagonal plate and all of the corresponding sections at a frequency of 84400 Hz are presented in Fig. 3.17 and 3.16. These are merely sample results presented for visual comparison.

The fixed boundary analysis demonstrated that very few of the results from the symmetric sections match with the results from the full model. Only two of the symmetry

models have any results that match with the results of the full model. The fourth model with symmetric-antisymmetric interior boundary conditions is able to match two of the results from the full model. The half side-side model with a symmetric interior boundary is able to match many, but not all of the results from the full model.

The free boundary analysis also demonstrated that very few of the results from the symmetric sections match with the results from the full model. Only nine of the twenty symmetry models have any results that match with the results of the full model, but no model has more than eight matches.

It is clear from this analysis that the only model of a hexagonal plate that can fully replicate the forced response is a full plate model.

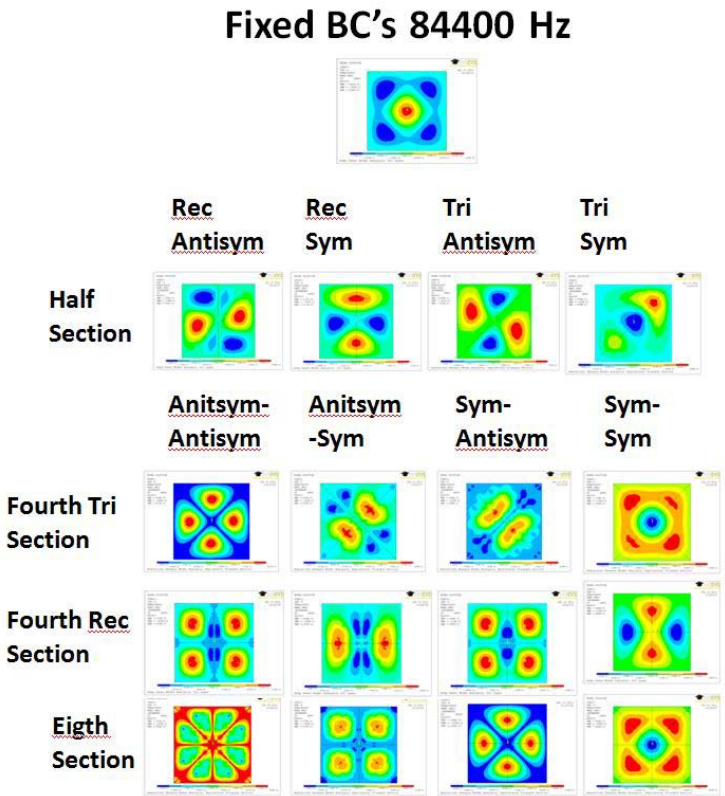

FIGURE 3.19. Harmonic results for the full plate and all of the symmetric sections with fixed boundary conditions and a frequency of 84400 Hz.

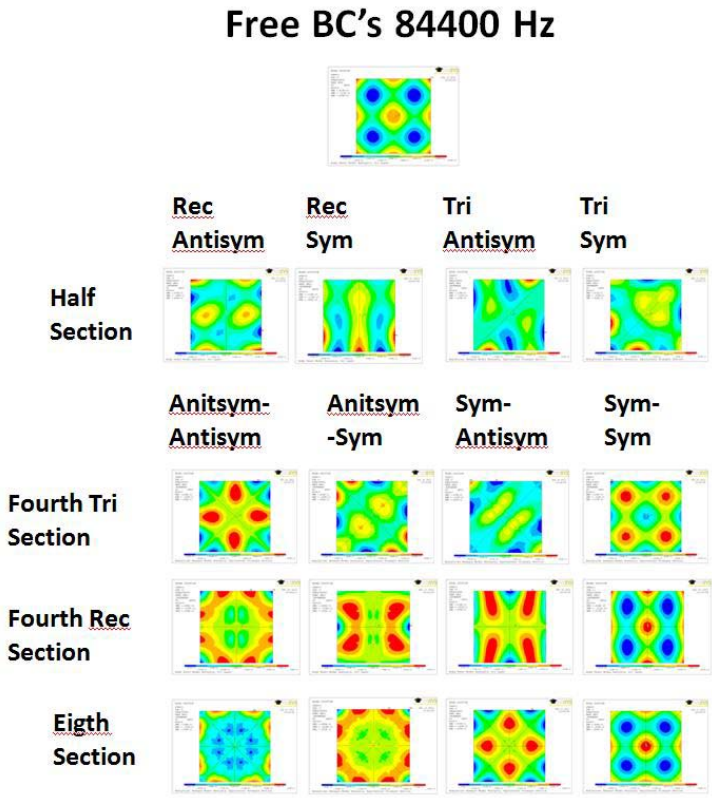

FIGURE 3.20. Harmonic results for the full plate and all of the symmetric sections with free boundary conditions and a frequency of 84400 Hz.

The results from the harmonic analysis performed on the square plate and all of the corresponding sections at a frequency of 84400 Hz are presented in Fig. 3.19 and 3.20. These are merely sample results presented for visual comparison.

The fixed boundary analysis demonstrated that very few of the results from the symmetric sections match with the results from the full model. Only three of the symmetry models have any results that match with the results of the full model. The eighth model with symmetric-symmetric interior boundary conditions is able to match seven of the results from the full model. The fourth triangular model with symmetric-symmetric interior boundary conditions is able to match two of the results from the full model. The fourth rectangular model

with symmetric-symmetric interior boundary conditions is able to match three of the results from the full model.

The free boundary analysis also demonstrated that very few of the results from the symmetric sections match with the results from the full model. The eighth model with symmetric-symmetric interior boundary conditions is able to match eight of the results from the full model. The fourth triangular model with symmetric-symmetric interior boundary conditions is able to match five of the results from the full model. The fourth rectangular model with symmetric-symmetric interior boundary conditions is able to match one of the results from the full model.

It is clear from this analysis that the only model of a square plate that can fully replicate the forced response is a full plate model.

Conclusion

Using a structure's natural symmetry has long been thought to be a valid way to reduce a model's size, complexity, and computation time. In order to test the accuracy of modeling with symmetric sections two different polygonal plates, a square and a hexagon, were divided along the symmetry lines of the polygons, and were subjected to a modal and a harmonic analysis. These two analyses can indicate whether a symmetric model can be used to recreate a full model without loss of accuracy.

The results from the modal analysis show that only half plate models can fully replicate all of the natural responses of the full plate, both the resonance frequencies and the resonance patterns. However, in order to replicate all of the resonances two half models must be run; one with a symmetric interior boundary, and one with an antisymmetric interior boundary. The

necessity of running two separate models negates the time saved by modeling with a symmetric section.

The results from the harmonic analysis show that no single model or combination of models can replicate the forced responses of the full plate.

Symmetric modeling is not accurate in many cases and should only be used very carefully. In certain cases the complexity and size of the model can be reduced but the computation time cannot.

References

3.1. Chandrupatla, T. R., Belegundu, A. D., “Introduction to Finite Elements in Engineering,” 2002, Prentice-Hall Inc., Upper Saddle River, New Jersey

3.2. Cook, R. D., Malkus, D. S., Plesha, M. E., Witt, R. J., “Concepts and Applications of Finite Element Analysis,” 2004, John Wiley & Sons

3.3. Timoshenko, S, “Vibration Problems in Engineering,” 1937, D. Van Nostrand Company Inc., New York

3.4. Denhartog, J. P., “Mechanical Vibrations,” 1985, Dover Books

3.5. Soedel, W., “Vibrations of Shells and Plates,” 2004, Marcel Dekker

APPENDIX A1
FULL DEVELOPMENT OF KACZKOWSKI'S SOLUTION

The equation of the transverse vibration of a triangular segment of a hexagonal plate and the proposed solution are given by Kaczkowski as:

$$D\nabla^4 w(x,y) + N\nabla^2 w(x,y) - (\mu\omega^2 - K)w(x,y) = 0 \tag{A1.1}$$

$$w(x,y) = \sum_{m=1,3,5,\ldots}^{\infty} \left\{ \left[A_m \cosh\left(\frac{m\pi\varphi_m}{a} y\right) + B_m \sinh\left(\frac{m\pi\varphi_m}{a} y\right) + C_m \cosh\left(\frac{m\pi\psi_m}{a} y\right) + D_m \sinh\left(\frac{m\pi\psi_m}{a} y\right) \right] \sin\left(\frac{m\pi}{a} x\right) \right\} \tag{A1.2}$$

The four coefficients require four distinct boundary conditions in order to reach an explicit solution. The solution is formulated such that symmetric boundary conditions are true on the line x=a/2 in Fig. 2.2. The equations for the boundary conditions are developed in Appendix A2.

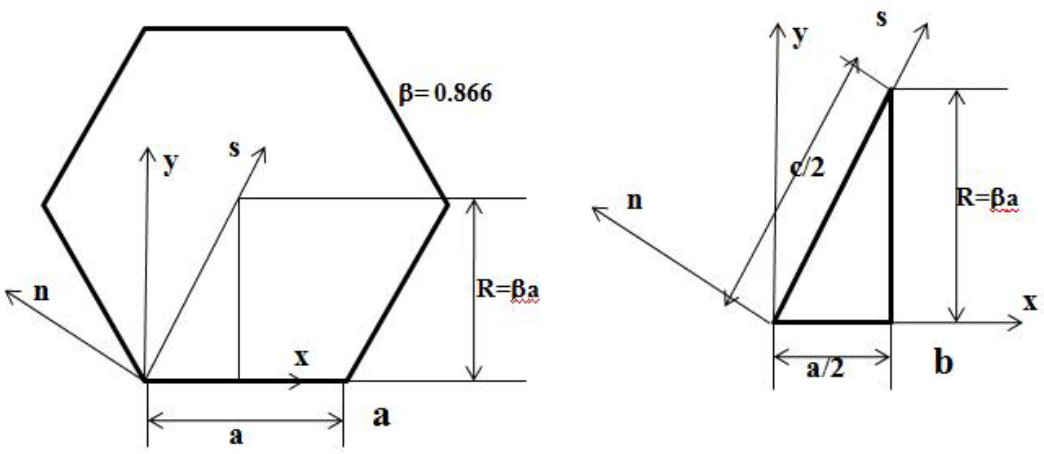

FIGURE 2.2. The regular hexagon and the triangular section used in the development of the analytical equation.

A1.1 Free Boundary Conditions

When the plate is freely held on the edge y=0 from Fig 2.2 the boundary conditions for that line are as follows:

$$V_y = \left(Q_y + \frac{\partial M_{xy}}{\partial x}\right) = 0 \implies \left(\frac{\partial^3 w}{\partial y^3} + (2-\nu)\frac{\partial^3 w}{\partial x^2 \partial y}\right)_{y=0} = 0 \tag{A1.3a}$$

Applying Kaczkowski's solution to this condition gives:

$$\begin{aligned}&\left\{\left[\left(\frac{m\pi\varphi_m}{a}\right)^3 A_m \sinh\left(\frac{m\pi\varphi_m}{a}y\right) + \left(\frac{m\pi\varphi_m}{a}\right)^3 B_m \cosh\left(\frac{m\pi\varphi_m}{a}y\right) + \left(\frac{m\pi\psi_m}{a}\right)^3 C_m \sinh\left(\frac{m\pi\psi_m}{a}y\right) + \right.\right.\\ &\left.\left.\left(\frac{m\pi\psi_m}{a}\right)^3 D_m \cosh\left(\frac{m\pi\psi_m}{a}y\right)\right]\sin\left(\frac{m\pi}{a}x\right)\right\} -\\ &(2-\nu)\left(\frac{m\pi}{a}\right)^2\left\{\left[\left(\frac{m\pi\varphi_m}{a}\right)A_m \sinh\left(\frac{m\pi\varphi_m}{a}y\right) + \left(\frac{m\pi\varphi_m}{a}\right)B_m \cosh\left(\frac{m\pi\varphi_m}{a}y\right) + \right.\right.\\ &\left.\left.\left(\frac{m\pi\psi_m}{a}\right)C_m \sinh\left(\frac{m\pi\psi_m}{a}y\right) + \left(\frac{m\pi\psi_m}{a}\right)D_m \cosh\left(\frac{m\pi\psi_m}{a}y\right)\right]\sin\left(\frac{m\pi}{a}x\right)\right\} = 0\end{aligned}$$

$$(\varphi_m^3 - (2-\nu)\varphi_m)B_m + (\psi_m^3 - (2-\nu)\psi_m)D_m \tag{A1.3b}$$

The second condition comes from the consideration that the plate section is not symmetric about the line y=0. This means that the even functions can be discarded while keeping the odd functions. From this consideration the following is true.

$$A_m = C_m = 0 \tag{A1.4}$$

The two equations, (A1.3b) and (A1.4), along with the two from the symmetric boundary constitute four conditions that give a system of linear equations which can be solved.

A1.2 Fixed Boundary Conditions

When the plate has a fixed boundary on the line y = 0 in Fig. 2.2 the boundary conditions are as follows:

$$(w)_{y=0} = 0 \tag{A1.5a}$$

$$\left(\frac{\partial w}{\partial y}\right)_{y=0} = 0 \tag{A1.6a}$$

Applying Kaczkowski's solution to the first condition gives:

$$A_m + C_m = 0 \tag{A1.5b}$$

Applying Kaczkowski's solutionto the second condition gives:

$$\left[\left(\frac{m\pi\varphi_m}{a}\right)A_m \sinh\left(\frac{m\pi\varphi_m}{a}y\right) + \left(\frac{m\pi\varphi_m}{a}\right)B_m \cosh\left(\frac{m\pi\varphi_m}{a}y\right) + \left(\frac{m\pi\psi_m}{a}\right)C_m \sinh\left(\frac{m\pi\psi_m}{a}y\right) + \left(\frac{m\pi\psi_m}{a}\right)D_m \cosh\left(\frac{m\pi\psi_m}{a}y\right)\right]\sin\left(\frac{m\pi}{a}x\right) = 0$$

$$\varphi_m B_m + \psi_m D_m = 0 \tag{A1.6b}$$

These two equations along with the two from the symmetric boundary constitute four conditions that give a system of linear equations which can be solved as:

A1.3 Symmetric Boundary Conditions Used by Kaczkowski

The line y = 2βx from Fig. 2.2 can support two different boundary conditions when it is considered in the context of the entire hexagonal plate. This boundary can either be symmetric or anti-symmetric. Here the symmetric condition will be considered. In order to apply the boundary equations, a new coordinate system must be defined.

$$x = s\frac{a}{c} - n\frac{2\beta a}{c}, \quad y = s\frac{2\beta a}{c} + n\frac{a}{c}, \quad where\ c = 2\sqrt{\left(\frac{a}{2}\right)^2 + (\beta a)^2}$$

$$\xi = \sigma - 2\beta\zeta, \quad \eta = 2\beta\sigma + \zeta, \quad \sigma = \frac{s}{c}, \quad \zeta = \frac{n}{c}$$

With these substitutions, the proposed solution becomes

$$w(\sigma,\zeta) = \sum_{m=1,3,5,\ldots}^{\infty}\{\left[A_m \cosh\left(m\pi\varphi_m(2\beta\sigma+\zeta)\right) + B_m \sinh\left(m\pi\varphi_m(2\beta\sigma+\zeta)\right) + C_m \cosh\left(m\pi\psi_m(2\beta\sigma+\zeta)\right) + D_m \sinh\left(m\pi\psi_m(2\beta\sigma+\zeta)\right)\right]\sin\left(m\pi(\sigma - 2\beta\zeta)\right)\} \tag{A1.7}$$

And the Laplacian of the proposed solution becomes:

$$\nabla^2 w(\sigma,\zeta) = \sum_{m=1,3,5,\ldots}^{\infty}\{\left[\Phi A_m \cosh\left(m\pi\varphi_m(2\beta\sigma+\zeta)\right) + \Phi B_m \sinh\left(m\pi\varphi_m(2\beta\sigma+\zeta)\right) + \Psi C_m \cosh\left(m\pi\psi_m(2\beta\sigma+\zeta)\right) + \Psi D_m \sinh\left(m\pi\psi_m(2\beta\sigma+\zeta)\right)\right]\sin\left(m\pi(\sigma-2\beta\zeta)\right)\} \tag{A1.8}$$

Using trigonometric and hyperbolic identities, the solution becomes:

$$\begin{aligned} w = & \\ & \sum_{m=1,3,5,\ldots}^{\infty}\{[A_m(\cosh(m\pi\varphi_m 2\beta\sigma)\cosh(m\pi\varphi_m\zeta) + \\ & \sinh(m\pi\varphi_m 2\beta\sigma)\sinh(m\pi\varphi_m\zeta)) + \\ & B_m(\sinh(m\pi\varphi_m 2\beta\sigma)\cosh(m\pi\varphi_m\zeta) + \\ & \cosh(m\pi\varphi_m 2\beta\sigma)\sinh(m\pi\varphi_m\zeta)) + \\ & C_m(\cosh(m\pi\psi_m 2\beta\sigma)\cosh(m\pi\psi_m\zeta) + \\ & \sinh(m\pi\psi_m 2\beta\sigma)\sinh(m\pi\psi_m\zeta)) + \\ & D_m(\sinh(m\pi\psi_m 2\beta\sigma)\cosh(m\pi\psi_m\zeta) + \\ & \cosh(m\pi\psi_m 2\beta\sigma)\sinh(m\pi\psi_m\zeta))][\sin(m\pi\sigma)\cos(-m\pi 2\beta\zeta) + \\ & \cos(m\pi\sigma)\sin(-m\pi 2\beta\zeta)]\} \end{aligned} \tag{A1.9}$$

And the Laplacian of the solution becomes:

$$\begin{aligned} \nabla^2 w = & -\left(\frac{\pi}{a}\right)^2 \sum_{m=1,3,5,\ldots}^{\infty}\{[\Phi A_m(\cosh(m\pi\varphi_m 2\beta\sigma)\cosh(m\pi\varphi_m\zeta) + \\ & \sinh(m\pi\varphi_m 2\beta\sigma)\sinh(m\pi\varphi_m\zeta)) + \\ & \Phi B_m(\sinh(m\pi\varphi_m 2\beta\sigma)\cosh(m\pi\varphi_m\zeta) + \\ & \cosh(m\pi\varphi_m 2\beta\sigma)\sinh(m\pi\varphi_m\zeta)) + \\ & \Psi C_m(\cosh(m\pi\psi_m 2\beta\sigma)\cosh(m\pi\psi_m\zeta) + \\ & \sinh(m\pi\psi_m 2\beta\sigma)\sinh(m\pi\psi_m\zeta)) + \\ & \Psi D_m(\sinh(m\pi\psi_m 2\beta\sigma)\cosh(m\pi\psi_m\zeta) + \\ & \cosh(m\pi\psi_m 2\beta\sigma)\sinh(m\pi\psi_m\zeta))][\sin(m\pi\sigma)\cos(-m\pi 2\beta\zeta) + \\ & \cos(m\pi\sigma)\sin(-m\pi 2\beta\zeta)]\} \end{aligned} \tag{A1.10}$$

The boundary conditions are given as

$$\left(\frac{\partial w}{\partial\zeta}\right)_{\zeta=0} = 0 \tag{A1.10a}$$

$$\left(\frac{\partial \nabla^2 w}{\partial\zeta}\right)_{\zeta=0} = 0 \tag{A1.11a}$$

Applying the modified proposed solution to the first condition yields:

$$\begin{aligned} \pi \sum_{m=1,3,5,\ldots}^{\infty} m\{[& \varphi_m A_m(\cosh(m\pi\varphi_m 2\beta\sigma)\sinh(m\pi\varphi_m\zeta) + \\ & \sinh(m\pi\varphi_m 2\beta\sigma)\cosh(m\pi\varphi_m\zeta)) + \\ & \varphi_m B_m(\sinh(m\pi\varphi_m 2\beta\sigma)\sinh(m\pi\varphi_m\zeta) + \end{aligned}$$

$$\cosh(m\pi\varphi_m 2\beta\sigma)\cosh(m\pi\varphi_m\zeta)) +$$
$$\psi_m C_m(\cosh(m\pi\psi_m 2\beta\sigma)\sinh(m\pi\psi_m\zeta) +$$
$$\sinh(m\pi\psi_m 2\beta\sigma)\cosh(m\pi\psi_m\zeta)) +$$
$$\psi_m D_m(\sinh(m\pi\psi_m 2\beta\sigma)\sinh(m\pi\psi_m\zeta) +$$
$$\cosh(m\pi\psi_m 2\beta\sigma)\cosh(m\pi\psi_m\zeta))][\sin(m\pi\sigma)\cos(-m\pi 2\beta\zeta) +$$
$$\cos(m\pi\sigma)\sin(-m\pi 2\beta\zeta)] -$$
$$2\beta[A_m(\cosh(m\pi\varphi_m 2\beta\sigma)\cosh(m\pi\varphi_m\zeta) +$$
$$\sinh(m\pi\varphi_m 2\beta\sigma)\sinh(m\pi\varphi_m\zeta)) +$$
$$B_m(\sinh(m\pi\varphi_m 2\beta\sigma)\cosh(m\pi\varphi_m\zeta) +$$
$$\cosh(m\pi\varphi_m 2\beta\sigma)\sinh(m\pi\varphi_m\zeta)) +$$
$$C_m(\cosh(m\pi\psi_m 2\beta\sigma)\cosh(m\pi\psi_m\zeta) +$$
$$\sinh(m\pi\psi_m 2\beta\sigma)\sinh(m\pi\psi_m\zeta)) +$$
$$D_m(\sinh(m\pi\psi_m 2\beta\sigma)\cosh(m\pi\psi_m\zeta) +$$
$$\cosh(m\pi\psi_m 2\beta\sigma)\sinh(m\pi\psi_m\zeta))][\sin(m\pi\sigma)\cos(-m\pi 2\beta\zeta) +$$
$$\cos(m\pi\sigma)\sin(-m\pi 2\beta\zeta)][-\sin(m\pi\sigma)\sin(-m\pi 2\beta\zeta) +$$
$$\cos(m\pi\sigma)\cos(-m\pi 2\beta\zeta)]\} = 0$$

$$\sum_{m=1,3,5,\ldots}^{\infty} m[A_m(\varphi_m \sinh(m\pi\varphi_m 2\beta\sigma)\sin(m\pi\sigma) -$$
$$2\beta\cosh(m\pi\varphi_m 2\beta\sigma)\cos(m\pi\sigma)) +$$
$$B_m(\varphi_m \cosh(m\pi\varphi_m 2\beta\sigma)\sin(m\pi\sigma) -$$
$$2\beta\sinh(m\pi\varphi_m 2\beta\sigma)\cos(m\pi\sigma)) +$$
$$C_m(\psi_m \sinh(m\pi\psi_m 2\beta\sigma)\sin(m\pi\sigma) -$$
$$2\beta\cosh(m\pi\psi_m 2\beta\sigma)\cos(m\pi\sigma)) +$$
$$D_m(\psi_m \cosh(m\pi\psi_m 2\beta\sigma)\sin(m\pi\sigma) -$$
$$2\beta\sinh(m\pi\psi_m 2\beta\sigma)\cos(m\pi\sigma))] = 0 \qquad \text{(A1.10b)}$$

Applying the Laplacian of the modified solution to the second condition gives:

$$-\pi\left(\frac{\pi}{a}\right)^2 \sum_{m=1,3,5,\ldots}^{\infty} m\{[\varphi_m \Phi A_m(\cosh(m\pi\varphi_m 2\beta\sigma)\sinh(m\pi\varphi_m\zeta) +$$
$$\sinh(m\pi\varphi_m 2\beta\sigma)\cosh(m\pi\varphi_m\zeta)) +$$
$$\varphi_m \Phi B_m(\sinh(m\pi\varphi_m 2\beta\sigma)\sinh(m\pi\varphi_m\zeta) +$$
$$\cosh(m\pi\varphi_m 2\beta\sigma)\cosh(m\pi\varphi_m\zeta)) +$$
$$\psi_m \Psi C_m(\cosh(m\pi\psi_m 2\beta\sigma)\sinh(m\pi\psi_m\zeta) +$$
$$\sinh(m\pi\psi_m 2\beta\sigma)\cosh(m\pi\psi_m\zeta)) +$$
$$\psi_m \Psi D_m(\sinh(m\pi\psi_m 2\beta\sigma)\sinh(m\pi\psi_m\zeta) +$$
$$\cosh(m\pi\psi_m 2\beta\sigma)\cosh(m\pi\psi_m\zeta))][\sin(m\pi\sigma)\cos(-m\pi 2\beta\zeta) +$$
$$\cos(m\pi\sigma)\sin(-m\pi 2\beta\zeta)] -$$
$$2\beta[\Phi A_m(\cosh(m\pi\varphi_m 2\beta\sigma)\cosh(m\pi\varphi_m\zeta) +$$
$$\sinh(m\pi\varphi_m 2\beta\sigma)\sinh(m\pi\varphi_m\zeta)) +$$
$$\Phi B_m(\sinh(m\pi\varphi_m 2\beta\sigma)\cosh(m\pi\varphi_m\zeta) +$$
$$\cosh(m\pi\varphi_m 2\beta\sigma)\sinh(m\pi\varphi_m\zeta)) +$$
$$\Psi C_m(\cosh(m\pi\psi_m 2\beta\sigma)\cosh(m\pi\psi_m\zeta) +$$
$$\sinh(m\pi\psi_m 2\beta\sigma)\sinh(m\pi\psi_m\zeta)) +$$
$$\Psi D_m(\sinh(m\pi\psi_m 2\beta\sigma)\cosh(m\pi\psi_m\zeta) +$$

$$\cosh(m\pi\psi_m 2\beta\sigma)\sinh(m\pi\psi_m\zeta))][\sin(m\pi\sigma)\cos(-m\pi 2\beta\zeta)+\cos(m\pi\sigma)\sin(-m\pi 2\beta\zeta)][-\sin(m\pi\sigma)\sin(-m\pi 2\beta\zeta)+\cos(m\pi\sigma)\cos(-m\pi 2\beta\zeta)]\}=0$$

$$\sum_{m=1,3,5,\dots}^{\infty} m[\Phi A_m(\varphi_m\sinh(m\pi\varphi_m 2\beta\sigma)\sin(m\pi\sigma)-2\beta\cosh(m\pi\varphi_m 2\beta\sigma)\cos(m\pi\sigma))+\Phi B_m(\varphi_m\cosh(m\pi\varphi_m 2\beta\sigma)\sin(m\pi\sigma)-2\beta\sinh(m\pi\varphi_m 2\beta\sigma)\cos(m\pi\sigma))+\Psi C_m(\psi_m\sinh(m\pi\psi_m 2\beta\sigma)\sin(m\pi\sigma)-2\beta\cosh(m\pi\psi_m 2\beta\sigma)\cos(m\pi\sigma))+\Psi D_m(\psi_m\cosh(m\pi\psi_m 2\beta\sigma)\sin(m\pi\sigma)-2\beta\sinh(m\pi\psi_m 2\beta\sigma)\cos(m\pi\sigma))]=0 \quad \text{(A1.11b)}$$

A1.4 Symmetric Boundary Conditions from Appendix A2

Using slightly different coordinate transformation and different boundary conditions, i.e. those developed in Appendix A2, slightly different equations for the coefficients are obtained. If the coordinate transformation used is:

$$x=\frac{a}{c}t-\frac{2\beta a}{c}n,\quad y=\frac{2\beta a}{c}t+\frac{a}{c}n,\quad where\ c=2\sqrt{\left(\frac{a}{2}\right)^2+(\beta a)^2}$$

Then the proposed solution becomes

$$w(n,t)=\sum_{m=1,3,5,\dots}^{\infty}\left\{\left[A_m\cosh\left(\frac{m\pi\varphi_m}{c}(n+2\beta t)\right)+B_m\sinh\left(\frac{m\pi\varphi_m}{c}(n+2\beta t)\right)+C_m\cosh\left(\frac{m\pi\psi_m}{c}(n+2\beta t)\right)+D_m\sinh\left(\frac{m\pi\psi_m}{c}(n+2\beta t)\right)\right]\sin\left(\frac{m\pi}{c}(t-2\beta n)\right)\right\} \quad \text{(A1.12)}$$

Applying the identities mentioned above transforms the solution into the following:

$$w=\sum_{m=1,3,5,\dots}^{\infty}\left\{\left[A_m\left(\cosh\left(\frac{m\pi\varphi_m}{c}2\beta t\right)\cosh\left(\frac{m\pi\varphi_m}{c}n\right)+\sinh\left(\frac{m\pi\varphi_m}{c}2\beta t\right)\sinh\left(\frac{m\pi\varphi_m}{c}n\right)\right)+B_m\left(\sinh\left(\frac{m\pi\varphi_m}{c}2\beta t\right)\cosh\left(\frac{m\pi\varphi_m}{c}n\right)+\cosh\left(\frac{m\pi\varphi_m}{c}2\beta t\right)\sinh\left(\frac{m\pi\varphi_m}{c}n\right)\right)+C_m\left(\cosh\left(\frac{m\pi\psi_m}{c}2\beta t\right)\cosh\left(\frac{m\pi\psi_m}{c}n\right)+ \quad \text{(A1.13)}$$

$$\sinh\left(\frac{m\pi\psi_m}{c}2\beta t\right)\sinh\left(\frac{m\pi\psi_m}{c}n\right)\Big) + D_m\left(\sinh\left(\frac{m\pi\psi_m}{c}2\beta t\right)\cosh\left(\frac{m\pi\psi_m}{c}n\right) + \cosh\left(\frac{m\pi\psi_m}{c}2\beta t\right)\sinh\left(\frac{m\pi\psi_m}{c}n\right)\Big)\Big]\Big[\sin\left(\frac{m\pi}{c}t\right)\cos\left(-\frac{m\pi}{c}2\beta n\right) + \cos\left(\frac{m\pi}{c}t\right)\sin\left(-\frac{m\pi}{c}2\beta n\right)\Big]\Big\}$$

The symmetric boundary conditions are:

$$\left(\frac{\partial w}{\partial n}\right)_{y=2\beta x} = 0 \tag{A1.14a}$$

$$V_n = \left(Q_n + \frac{\partial M_{nt}}{\partial t}\right) = 0 \implies \left(\frac{\partial^3 w}{\partial n^3} + (2-\nu)\frac{\partial^3 w}{\partial n \partial t^2}\right)_{y=2\beta x} = 0 \tag{A1.15a}$$

Applying Kaczkowski's solution to the first symmetry condition on n = 0 gives:

$$\sum_{m=1,3,5,\ldots}^{\infty}\Big\{\Big[\left(\frac{m\pi\varphi_m}{c}\right)A_m\left(\cosh\left(\frac{m\pi\varphi_m}{c}2\beta t\right)\sinh\left(\frac{m\pi\varphi_m}{c}n\right) + \sinh\left(\frac{m\pi\varphi_m}{c}2\beta t\right)\cosh\left(\frac{m\pi\varphi_m}{c}n\right)\right) + \left(\frac{m\pi\varphi_m}{c}\right)B_m\left(\sinh\left(\frac{m\pi\varphi_m}{c}2\beta t\right)\sinh\left(\frac{m\pi\varphi_m}{c}n\right) + \cosh\left(\frac{m\pi\varphi_m}{c}2\beta t\right)\cosh\left(\frac{m\pi\varphi_m}{c}n\right)\right) + \left(\frac{m\pi\psi_m}{c}\right)C_m\left(\cosh\left(\frac{m\pi\psi_m}{c}2\beta t\right)\sinh\left(\frac{m\pi\psi_m}{c}n\right) + \sinh\left(\frac{m\pi\psi_m}{c}2\beta t\right)\cosh\left(\frac{m\pi\psi_m}{c}n\right)\right) + \left(\frac{m\pi\psi_m}{c}\right)D_m\left(\sinh\left(\frac{m\pi\psi_m}{c}2\beta t\right)\sinh\left(\frac{m\pi\psi_m}{c}n\right) + \cosh\left(\frac{m\pi\psi_m}{c}2\beta t\right)\cosh\left(\frac{m\pi\psi_m}{c}n\right)\right)\Big]\Big[\sin\left(\frac{m\pi}{c}t\right)\cos\left(-\frac{m\pi}{c}2\beta n\right) + \cos\left(\frac{m\pi}{c}t\right)\sin\left(-\frac{m\pi}{c}2\beta n\right)\Big] - 2\beta\left(\frac{m\pi}{c}\right)\Big[A_m\left(\cosh\left(\frac{m\pi\varphi_m}{c}2\beta t\right)\cosh\left(\frac{m\pi\varphi_m}{c}n\right) + \sinh\left(\frac{m\pi\varphi_m}{c}2\beta t\right)\sinh\left(\frac{m\pi\varphi_m}{c}n\right)\right) + B_m\left(\sinh\left(\frac{m\pi\varphi_m}{c}2\beta t\right)\cosh\left(\frac{m\pi\varphi_m}{c}n\right) + \cosh\left(\frac{m\pi\varphi_m}{c}2\beta t\right)\sinh\left(\frac{m\pi\varphi_m}{c}n\right)\right) + C_m\left(\cosh\left(\frac{m\pi\psi_m}{c}2\beta t\right)\cosh\left(\frac{m\pi\psi_m}{c}n\right) + \sinh\left(\frac{m\pi\psi_m}{c}2\beta t\right)\sinh\left(\frac{m\pi\psi_m}{c}n\right)\right) + D_m\left(\sinh\left(\frac{m\pi\psi_m}{c}2\beta t\right)\cosh\left(\frac{m\pi\psi_m}{c}n\right) + \cosh\left(\frac{m\pi\psi_m}{c}2\beta t\right)\sinh\left(\frac{m\pi\psi_m}{c}n\right)\right)\Big]\Big[-\sin\left(\frac{m\pi}{c}t\right)\sin\left(-\frac{m\pi}{c}2\beta n\right) + \cos\left(\frac{m\pi}{c}t\right)\cos\left(-\frac{m\pi}{c}2\beta n\right)\Big]\Big\} = 0$$

$$\sum_{m=1,3,5,\ldots}^{\infty}\Big\{A_m\Big[\varphi_m\sinh\left(\frac{m\pi\varphi_m}{c}2\beta t\right)\sin\left(\frac{m\pi}{c}t\right) - 2\beta\cosh\left(\frac{m\pi\varphi_m}{c}2\beta t\right)\cos\left(\frac{m\pi}{c}t\right)\Big] + B_m\Big[\varphi_m\sinh\left(\frac{m\pi\varphi_m}{c}2\beta t\right)\sin\left(\frac{m\pi}{c}t\right) - 2\beta\cosh\left(\frac{m\pi\varphi_m}{c}2\beta t\right)\cos\left(\frac{m\pi}{c}t\right)\Big] + C_m\Big[\psi_m\sinh\left(\frac{m\pi\varphi_m}{c}2\beta t\right)\sin\left(\frac{m\pi}{c}t\right) - 2\beta\cosh\left(\frac{m\pi\varphi_m}{c}2\beta t\right)\cos\left(\frac{m\pi}{c}t\right)\Big] + D_m\Big[\psi_m\sinh\left(\frac{m\pi\varphi_m}{c}2\beta t\right)\sin\left(\frac{m\pi}{c}t\right) - 2\beta\cosh\left(\frac{m\pi\varphi_m}{c}2\beta t\right)\cos\left(\frac{m\pi}{c}t\right)\Big]\Big\} = 0 \tag{A1.14b}$$

Applying the solution to the second symmetry condition on n = 0 gives:

$$\sum_{m=1,3,5,\ldots}^{\infty}\left\{\left[\left(\frac{m\pi\varphi_m}{c}\right)^3 A_m\left(\cosh\left(\frac{m\pi\varphi_m}{c}2\beta t\right)\sinh\left(\frac{m\pi\varphi_m}{c}n\right)+\right.\right.$$
$$\sinh\left(\frac{m\pi\varphi_m}{c}2\beta t\right)\cosh\left(\frac{m\pi\varphi_m}{c}n\right)\Big)+\left(\frac{m\pi\varphi_m}{c}\right)^3 B_m\left(\sinh\left(\frac{m\pi\varphi_m}{c}2\beta t\right)\sinh\left(\frac{m\pi\varphi_m}{c}n\right)+$$
$$\cosh\left(\frac{m\pi\varphi_m}{c}2\beta t\right)\cosh\left(\frac{m\pi\varphi_m}{c}n\right)\Big)+$$
$$\left(\frac{m\pi\psi_m}{c}\right)^3 C_m\left(\cosh\left(\frac{m\pi\psi_m}{c}2\beta t\right)\sinh\left(\frac{m\pi\psi_m}{c}n\right)+\sinh\left(\frac{m\pi\psi_m}{c}2\beta t\right)\cosh\left(\frac{m\pi\psi_m}{c}n\right)\right)+$$
$$\left(\frac{m\pi\psi_m}{c}\right)^3 D_m\left(\sinh\left(\frac{m\pi\psi_m}{c}2\beta t\right)\sinh\left(\frac{m\pi\psi_m}{c}n\right)+\right.$$
$$\left.\left.\cosh\left(\frac{m\pi\psi_m}{c}2\beta t\right)\cosh\left(\frac{m\pi\psi_m}{c}n\right)\right)\right]\left[\sin\left(\frac{m\pi}{c}t\right)\cos\left(-\frac{m\pi}{c}2\beta n\right)+\right.$$
$$\left.\cos\left(\frac{m\pi}{c}t\right)\sin\left(-\frac{m\pi}{c}2\beta n\right)\right]-(2\beta)^3\left(\frac{m\pi}{c}\right)^3\left[A_m\left(\cosh\left(\frac{m\pi\varphi_m}{c}2\beta t\right)\cosh\left(\frac{m\pi\varphi_m}{c}n\right)+\right.\right.$$
$$\sinh\left(\frac{m\pi\varphi_m}{c}2\beta t\right)\sinh\left(\frac{m\pi\varphi_m}{c}n\right)\Big)+B_m\left(\sinh\left(\frac{m\pi\varphi_m}{c}2\beta t\right)\cosh\left(\frac{m\pi\varphi_m}{c}n\right)+$$
$$\cosh\left(\frac{m\pi\varphi_m}{c}2\beta t\right)\sinh\left(\frac{m\pi\varphi_m}{c}n\right)\Big)+C_m\left(\cosh\left(\frac{m\pi\psi_m}{c}2\beta t\right)\cosh\left(\frac{m\pi\psi_m}{c}n\right)+$$
$$\sinh\left(\frac{m\pi\psi_m}{c}2\beta t\right)\sinh\left(\frac{m\pi\psi_m}{c}n\right)\Big)+D_m\left(\sinh\left(\frac{m\pi\psi_m}{c}2\beta t\right)\cosh\left(\frac{m\pi\psi_m}{c}n\right)+$$
$$\left.\left.\cosh\left(\frac{m\pi\psi_m}{c}2\beta t\right)\sinh\left(\frac{m\pi\psi_m}{c}n\right)\right)\right]\left[\sin\left(\frac{m\pi}{c}t\right)\sin\left(-\frac{m\pi}{c}2\beta n\right)-\right.$$
$$\left.\cos\left(\frac{m\pi}{c}t\right)\cos\left(-\frac{m\pi}{c}2\beta n\right)\right]-6\beta\left[\left(\frac{m\pi\varphi_m}{c}\right)^2 A_m\left(\cosh\left(\frac{m\pi\varphi_m}{c}2\beta t\right)\cosh\left(\frac{m\pi\varphi_m}{c}n\right)+\right.$$
$$\sinh\left(\frac{m\pi\varphi_m}{c}2\beta t\right)\sinh\left(\frac{m\pi\varphi_m}{c}n\right)\Big)+\left(\frac{m\pi\varphi_m}{c}\right)^2 B_m\left(\sinh\left(\frac{m\pi\varphi_m}{c}2\beta t\right)\cosh\left(\frac{m\pi\varphi_m}{c}n\right)+$$
$$\cosh\left(\frac{m\pi\varphi_m}{c}2\beta t\right)\sinh\left(\frac{m\pi\varphi_m}{c}n\right)\Big)+$$
$$\left(\frac{m\pi\psi_m}{c}\right)^2 C_m\left(\cosh\left(\frac{m\pi\psi_m}{c}2\beta t\right)\cosh\left(\frac{m\pi\psi_m}{c}n\right)+\sinh\left(\frac{m\pi\psi_m}{c}2\beta t\right)\sinh\left(\frac{m\pi\psi_m}{c}n\right)\right)+$$
$$\left(\frac{m\pi\psi_m}{c}\right)^2 D_m\left(\sinh\left(\frac{m\pi\psi_m}{c}2\beta t\right)\cosh\left(\frac{m\pi\psi_m}{c}n\right)+\right.$$
$$\left.\left.\cosh\left(\frac{m\pi\psi_m}{c}2\beta t\right)\sinh\left(\frac{m\pi\psi_m}{c}n\right)\right)\right]\left[-\sin\left(\frac{m\pi}{c}t\right)\sin\left(-\frac{m\pi}{c}2\beta n\right)+\right.$$
$$\left.\cos\left(\frac{m\pi}{c}t\right)\cos\left(-\frac{m\pi}{c}2\beta n\right)\right]-12\beta^2\left[\left(\frac{m\pi\varphi_m}{c}\right)A_m\left(\cosh\left(\frac{m\pi\varphi_m}{c}2\beta t\right)\sinh\left(\frac{m\pi\varphi_m}{c}n\right)+\right.$$
$$\sinh\left(\frac{m\pi\varphi_m}{c}2\beta t\right)\cosh\left(\frac{m\pi\varphi_m}{c}n\right)\Big)+\left(\frac{m\pi\varphi_m}{c}\right)B_m\left(\sinh\left(\frac{m\pi\varphi_m}{c}2\beta t\right)\sinh\left(\frac{m\pi\varphi_m}{c}n\right)+$$
$$\cosh\left(\frac{m\pi\varphi_m}{c}2\beta t\right)\cosh\left(\frac{m\pi\varphi_m}{c}n\right)\Big)+$$
$$\left(\frac{m\pi\psi_m}{c}\right)C_m\left(\cosh\left(\frac{m\pi\psi_m}{c}2\beta t\right)\sin 3\,\mathrm{h}\left(\frac{m\pi\psi_m}{c}n\right)+\right.$$
$$\sinh\left(\frac{m\pi\psi_m}{c}2\beta t\right)\cosh\left(\frac{m\pi\psi_m}{c}n\right)\Big)+\left(\frac{m\pi\psi_m}{c}\right)D_m\left(\sinh\left(\frac{m\pi\psi_m}{c}2\beta t\right)\sinh\left(\frac{m\pi\psi_m}{c}n\right)+$$
$$\left.\left.\cosh\left(\frac{m\pi\psi_m}{c}2\beta t\right)\cosh\left(\frac{m\pi\psi_m}{c}n\right)\right)\right]\left[-\sin\left(\frac{m\pi}{c}t\right)\cos\left(-\frac{m\pi}{c}2\beta n\right)+\right.$$
$$\left.\left.\cos\left(\frac{m\pi}{c}t\right)\sin\left(-\frac{m\pi}{c}2\beta n\right)\right]\right\}=0$$

$$\sum_{m=1,3,5,\ldots}^{\infty}\Big\{A_m\Big[(\varphi_m^3-3\varphi_m(2\beta)^2)\sinh\left(\frac{m\pi\varphi_m}{c}2\beta t\right)\sin\left(\frac{m\pi}{c}t\right)+$$
$$\left((2\beta)^3+3\varphi_m^2(2\beta)\right)\cosh\left(\frac{m\pi\varphi_m}{c}2\beta t\right)\cos\left(\frac{m\pi}{c}t\right)\Big]+B_m\Big[(\varphi_m^3-$$
$$3\varphi_m(2\beta)^2)\cosh\left(\frac{m\pi\varphi_m}{c}2\beta t\right)\sin\left(\frac{m\pi}{c}t\right)+$$
$$\left((2\beta)^3+3\varphi_m^2(2\beta)\right)\sinh\left(\frac{m\pi\varphi_m}{c}2\beta t\right)\cos\left(\frac{m\pi}{c}t\right)\Big]+C_m\Big[(\psi_m^3-\qquad\text{(A1.15b)}$$
$$3\psi_m(2\beta)^2)\sinh\left(\frac{m\pi\psi_m}{c}2\beta t\right)\sin\left(\frac{m\pi}{c}t\right)+$$
$$\left((2\beta)^3+3\psi_m^2(2\beta)\right)\cosh\left(\frac{m\pi\psi_m}{c}2\beta t\right)\cos\left(\frac{m\pi}{c}t\right)\Big]+D_m\Big[(\psi_m^3-$$

$$3\psi_m(2\beta)^2)\cosh\left(\frac{m\pi\psi_m}{c}2\beta t\right)\sin\left(\frac{m\pi}{c}t\right)+$$
$$\left((2\beta)^3+3\psi_m^2(2\beta)\right)\sinh\left(\frac{m\pi\psi_m}{c}2\beta t\right)\cos\left(\frac{m\pi}{c}t\right)\Big]\Big\}=0$$

APPENDIX A2
Development of Basic Plate Equations

Some basic moment-deflection equations:

$$\left.\begin{aligned} M_x &= -D\left(\frac{\partial^2 w}{\partial x^2} + \nu\frac{\partial^2 w}{\partial y^2}\right) \\ M_y &= -D\left(\frac{\partial^2 w}{\partial y^2} + \nu\frac{\partial^2 w}{\partial x^2}\right) \\ M_{xy} &= -M_{yx} = D(1-\nu)\frac{\partial^2 w}{\partial x \partial y} \end{aligned}\right\} \tag{A2.1}$$

$$D = \frac{Eh^3}{12(1-\nu^2)}$$

A2.1 Equilibrium

Summing all of the forces on the element in the x direction gives

$$\Sigma F_x = 0 = Q_x dy - \left(Q_x + \frac{\partial Q_x}{\partial x}dx\right)dy - Q_y dx + \left(Q_y + \frac{\partial Q_y}{\partial y}dy\right)dx - q dx dy$$

$$-\frac{\partial Q_x}{\partial x}dxdy - \frac{\partial Q_y}{\partial y}dxdy - q dxdy = 0$$

$$\frac{\partial Q_x}{\partial x} + \frac{\partial Q_y}{\partial y} + q = 0 \tag{A2.2}$$

Similarly summing the forces in the y direction gives

$$\frac{\partial Q_x}{\partial x} + \frac{\partial Q_y}{\partial y} - q = 0 \tag{A2.3}$$

Summing all of the moments of the element about the x-axis gives

$$\Sigma M_x = 0 = M_y dx - \left(M_y + \frac{\partial M_y}{\partial y}dy\right)dx + M_{yx}dx - \left(M_{yx} + \frac{\partial M_{yx}}{\partial x}dx\right)dy + \left(Q_y + \frac{\partial Q_y}{\partial y}dy\right)dxdy - Q_x dydy + \left(Q_x + \frac{\partial Q_x}{\partial x}dx\right)dydy + q dxdy$$

$$-\frac{\partial M_y}{\partial y}dxdy - \frac{\partial M_{yx}}{\partial x}dxdy + Q_y = 0$$

$$Q_y = \frac{\partial M_y}{\partial y} + \frac{\partial M_{xy}}{\partial x} \tag{A2.4}$$

Similarly summing the moments about the y-axis gives

$$Q_x = \frac{\partial M_x}{\partial x} + \frac{\partial M_{xy}}{\partial y} \tag{A2.5}$$

An equilibrium equation can be expressed solely in terms of the moment derivatives by substituting expressions (---.4) and (---.5) into (---.2) and eliminating Q_x and Q_y.

$$\frac{\partial}{\partial \mathrm{x}}\left(\frac{\partial \mathrm{M_{xy}}}{\partial \mathrm{y}} + \frac{\partial \mathrm{M_x}}{\partial \mathrm{x}}\right) + \frac{\partial}{\partial \mathrm{y}}\left(-\frac{\partial \mathrm{M_{xy}}}{\partial \mathrm{x}} + \frac{\partial \mathrm{M_y}}{\partial \mathrm{y}}\right) + \mathrm{q} = 0$$

$$\frac{\partial^2 M_x}{\partial x^2} + \frac{\partial^2 M_y}{\partial y^2} - 2\frac{\partial^2 M_{xy}}{\partial x \partial y} = -q \tag{A2.6}$$

A2.2 Differential Equation of Transverse Deflection

The differential equation for the transverse deflection of the plate can be obtained by substituting the moment-curvature relationships (A2.1) into the equilibrium equation (A2.6). Here the plate bending stiffness is assumed to be constant.

$$\frac{\partial^2}{\partial x^2}\left[-D\left(\frac{\partial^2 w}{\partial x^2} + \nu\frac{\partial^2 w}{\partial y^2}\right)\right] + \frac{\partial^2}{\partial y^2}\left[-D\left(\frac{\partial^2 w}{\partial y^2} + \nu\frac{\partial^2 w}{\partial x^2}\right)\right] - 2\frac{\partial^2}{\partial x \partial y}\left[D(1-\nu)\frac{\partial^2 w}{\partial x \partial y}\right] = q$$

$$-D\frac{\partial^4 w}{\partial x^4} - D\nu\frac{\partial^4 w}{\partial x^2 \partial y^2} - D\frac{\partial^4 w}{\partial y^4} - D\nu\frac{\partial^4 w}{\partial x^2 \partial y^2} - 2D(1-\nu)\frac{\partial^4 w}{\partial x^2 \partial y^2} = -q$$

$$\frac{\partial^4 w}{\partial x^4} + \frac{\partial^4 w}{\partial y^4} + \left[\nu\frac{\partial^4 w}{\partial x^2 \partial y^2} + \nu\frac{\partial^4 w}{\partial x^2 \partial y^2} + (2-2\nu)\frac{\partial^4 w}{\partial x^2 \partial y^2}\right] = \frac{q}{D}$$

$$\frac{\partial^4 w}{\partial x^4} + 2\frac{\partial^4 w}{\partial x^2 \partial y^2} + \frac{\partial^4 w}{\partial y^4} = \nabla^4 \mathrm{w} = \frac{\mathrm{q}}{\mathrm{D}} \tag{A2.7}$$

This equation for the transverse deflection does not include any mid-plane stress and is essentially for a freely bound plate.

A2.3 Mid-Plane Stress

Mid-plane stress develops directly from the application of forces at the boundary of the plate. Fig. A2.1 shows the forces per unit length of the mid-plane.

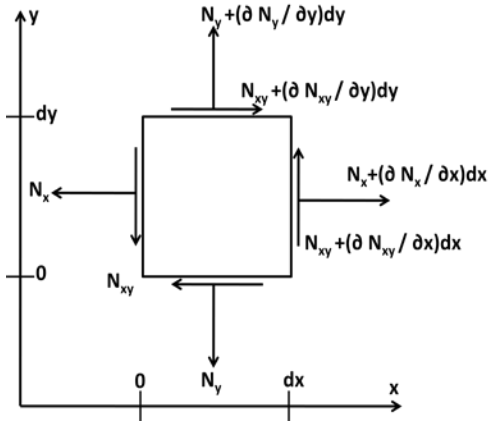

FIGURE A2.1. Forces per unit length of the mid-plane

Equilibrium of the mid-plane forces on element δxδy gives the following equations.

$$\sum F_x = 0 = -N_x dy + \left(N_x + \frac{\partial N_x}{\partial x}dx\right)dy - N_{xy}dx + \left(N_{xy} + \frac{\partial N_{xy}}{\partial y}dy\right)dx$$

$$\frac{\partial N_x}{\partial x}dxdy + \frac{\partial N_{xy}}{\partial y}dxdy = 0$$

$$\frac{\partial N_x}{\partial x} + \frac{\partial N_{xy}}{\partial y} = 0 \qquad \text{(A2.8)}$$

$$\sum F_y = 0 = -N_y dx + \left(N_y + \frac{\partial N_y}{\partial y}dy\right)dx - N_{xy}dy + \left(N_{xy} + \frac{\partial N_{xy}}{\partial x}dx\right)dy$$

$$\frac{\partial N_y}{\partial y}dxdy + \frac{\partial N_{xy}}{\partial x}dxdy = 0$$

$$\frac{\partial N_y}{\partial y} + \frac{\partial N_{xy}}{\partial x} = 0 \qquad \text{(A2.9)}$$

If a force function, Φ, is introduced the conditions (A2.8) and (A2.9) are satisfied and the quantities N_x, N_y, and N_{xy} can be calculated.

$$\frac{\partial N_x}{\partial x}+\frac{\partial N_{xy}}{\partial y}=0=\frac{\partial^2 \Phi_1}{\partial x\partial y}+\frac{\partial^2 \Phi_1}{\partial x\partial y} \implies N_x=\frac{\partial \Phi_1}{\partial y}, N_{xy}=-\frac{\partial \Phi_1}{\partial x}$$

$$\frac{\partial N_y}{\partial y}+\frac{\partial N_{xy}}{\partial x}=0=\frac{\partial^2 \Phi_2}{\partial x\partial y}+\frac{\partial^2 \Phi_2}{\partial x\partial y} \implies N_y=\frac{\partial \Phi_2}{\partial x}, N_{xy}=-\frac{\partial \Phi_2}{\partial y}$$

$$N_{xy}-N_{xy}=0=-\frac{\partial \Phi_1}{\partial x}+\frac{\partial \Phi_2}{\partial y} \implies \Phi_1=\frac{\partial \Phi}{\partial y}, \Phi_2=\frac{\partial \Phi}{\partial x}$$

$$\left.\begin{aligned} N_x &= \frac{\partial^2 \Phi}{\partial y^2} \\ N_y &= \frac{\partial^2 \Phi}{\partial x^2} \\ N_{xy} &= -\frac{\partial^2 \Phi}{\partial x\partial y} \end{aligned}\right\} \tag{A2.10}$$

If the strains in the mid-plane are due solely to the mid-plane forces then the following are true according to the Theory of Elasticity.

$$\left.\begin{aligned} \frac{\partial u}{\partial x} &= \frac{(N_x-\nu N_y)}{Eh} \\ \frac{\partial v}{\partial y} &= \frac{(N_y-\nu N_x)}{Eh} \\ \frac{\partial u}{\partial y}+\frac{\partial v}{\partial x} &= \frac{2N_{xy}(1+\nu)}{Et} \end{aligned}\right\} \tag{A2.11}$$

The compatibility condition requires the following to be true.

$$\frac{\partial^2}{\partial y^2}\left(\frac{\partial u}{\partial x}\right)+\frac{\partial^2}{\partial x^2}\left(\frac{\partial v}{\partial y}\right)-\frac{\partial^2}{\partial x\partial y}\left(\frac{\partial u}{\partial y}+\frac{\partial v}{\partial x}\right)=0$$

Which can be expressed as:

$$\frac{\partial^2}{\partial y^2}\left(\frac{(N_x-\nu N_y)}{Eh}\right)+\frac{\partial^2}{\partial x^2}\left(\frac{(N_y-\nu N_x)}{Eh}\right)-\frac{\partial^2}{\partial x\partial y}\left(\frac{2N_{xy}(1+\nu)}{Et}\right)=0$$

$$\frac{\partial^2}{\partial y^2}\left(\frac{1}{Eh}\frac{\partial^2\Phi}{\partial y^2}\right)-\nu\frac{\partial^2}{\partial y^2}\left(\frac{1}{Eh}\frac{\partial^2\Phi}{\partial x^2}\right)+\frac{\partial^2}{\partial x^2}\left(\frac{1}{Eh}\frac{\partial^2\Phi}{\partial x^2}\right)-\nu\frac{\partial^2}{\partial x^2}\left(\frac{1}{Eh}\frac{\partial^2\Phi}{\partial y^2}\right)+\frac{2(1+\nu)}{Eh}\frac{\partial^4\Phi}{\partial x^2\partial y^2}=0$$

or when h is constant over the plate:

$$\frac{\partial^4\Phi}{\partial x^4}+\frac{\partial^4\Phi}{\partial y^4}+2\frac{\partial^4\Phi}{\partial x^2\partial y^2}=\nabla^4\Phi=0 \tag{A2.12}$$

A2.4 Z Component Mid-Plane Forces

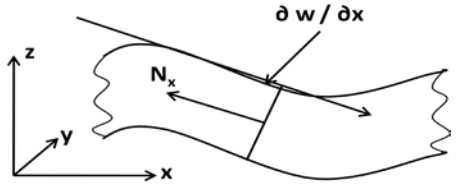

FIGURE A2.2. A plate section under deflection. The mid-plane force exhibits a z-component.

It can be seen from Fig A2.2 that the mid-plane forces have a z-component, which can be written by inspection as

$$@x = 0 \implies -N_x \frac{\partial w}{\partial x} dy - N_{xy} \frac{\partial w}{\partial y} dy$$

$$@x = dx \implies N_x \frac{\partial w}{\partial x} dy + \frac{\partial}{\partial x}\left(N_x \frac{\partial w}{\partial x}\right) dxdy + N_{xy} \frac{\partial w}{\partial y} dy + \frac{\partial}{\partial x}\left(N_{xy} \frac{\partial w}{\partial y}\right) dxdy$$

$$@y = 0 \implies -N_y \frac{\partial w}{\partial y} dx - N_{xy} \frac{\partial w}{\partial x} dx$$

$$@y = dy \implies N_y \frac{\partial w}{\partial y} dx + \frac{\partial}{\partial y}\left(N_y \frac{\partial w}{\partial y}\right) dxdy + N_{xy} \frac{\partial w}{\partial x} dx + \frac{\partial}{\partial y}\left(N_{xy} \frac{\partial w}{\partial x}\right) dxdy$$

The resultant force in the z direction (including a force applied to the face of the plate) can be written as

$$\sum F_z = q' = -N_x \frac{\partial w}{\partial x} dy - N_{xy} \frac{\partial w}{\partial y} dy + N_x \frac{\partial w}{\partial x} dy + \frac{\partial}{\partial x}\left(N_x \frac{\partial w}{\partial x}\right) dxdy + N_{xy} \frac{\partial w}{\partial y} dy + \frac{\partial}{\partial x}\left(N_{xy} \frac{\partial w}{\partial y}\right) dxdy$$
$$- N_y \frac{\partial w}{\partial y} dx - N_{xy} \frac{\partial w}{\partial x} dx + N_y \frac{\partial w}{\partial y} dx + \frac{\partial}{\partial y}\left(N_y \frac{\partial w}{\partial y}\right) dxdy + N_{xy} \frac{\partial w}{\partial x} dx + \frac{\partial}{\partial y}\left(N_{xy} \frac{\partial w}{\partial x}\right) dxdy$$

$$\frac{\partial}{\partial x}\left(N_x \frac{\partial w}{\partial x} + N_{xy} \frac{\partial w}{\partial y}\right) dxdy + \frac{\partial}{\partial y}\left(N_y \frac{\partial w}{\partial y} + N_{xy} \frac{\partial w}{\partial x}\right) dxdy = q'$$

$$N_x \frac{\partial^2 w}{\partial x^2} + 2N_{xy} \frac{\partial^2 w}{\partial x \partial y} + N_y \frac{\partial^2 w}{\partial y^2} = q' \tag{A2.13}$$

$$\frac{\partial^2 \Phi}{\partial x^2} \frac{\partial^2 w}{\partial x^2} - 2 \frac{\partial^2 \Phi}{\partial x \partial y} \frac{\partial^2 w}{\partial x \partial y} + \frac{\partial^2 \Phi}{\partial y^2} \frac{\partial^2 w}{\partial y^2} = q'$$

Combining (A2.7) and (A2.13) gives an expression for the deflection of a plate that includes mid-plane forces.

$$D\nabla^4 w = q + q' \implies D\nabla^4 w = q + N_x \frac{\partial^2 w}{\partial x^2} + 2N_{xy} \frac{\partial^2 w}{\partial x \partial y} + N_y \frac{\partial^2 w}{\partial y^2} \quad \text{(A2.14)}$$

If the plate is on an elastic foundation while it experiences deflection then there will be a restoring pressure acting on the plate due to the foundation.

$$q = q_{res} - Kw \quad \text{(A2.15)}$$

Where K is the foundation/Winkler stiffness. This gives the following

$$D\nabla^4 w = q_{res} + Kw + N_x \frac{\partial^2 w}{\partial x^2} + 2N_{xy} \frac{\partial^2 w}{\partial x \partial y} + N_y \frac{\partial^2 w}{\partial y^2} \quad \text{(A2.16)}$$

When the plate the plate is vibrating the elastic reaction of the plate produces an acceleration on each element of the plate.

$$F_{accel} = -\mu \frac{\partial^2 w}{\partial t^2} \quad \text{(A2.17)}$$

Where μ is the area mass. If we substitute the acceleration force for q_{res}

$$D\nabla^4 \mathrm{w} + \mathrm{Kw} + \mu \frac{\partial^2 w}{\partial t^2} = \mathrm{N_x} \frac{\partial^2 \mathrm{w}}{\partial x^2} + 2\mathrm{N_{xy}} \frac{\partial^2 \mathrm{w}}{\partial x \partial y} + \mathrm{N_y} \frac{\partial^2 \mathrm{w}}{\partial y^2} \quad \text{(A2.18)}$$

For a vibrating plate a solution of the above differential equation can be assumed to exhibit simple harmonic motion.

$$w(x, y, t) = w(x, y) \sin\big(\omega(t - t_0)\big) \quad \text{(A2.19)}$$

Using this assumed solution in the above equation gives the following

$$D\nabla^4 w(x,y) \sin\big(\omega(t-t_0)\big) + Kw(x,y) \sin\big(\omega(t-t_0)\big) - \mu\omega^2 w(x,y) \sin\big(\omega(t-t_0)\big) = N_x \frac{\partial^2 w(x,y)}{\partial x^2} \sin\big(\omega(t-t_0)\big) + 2N_{xy} \frac{\partial^2 w(x,y)}{\partial x \partial y} \sin\big(\omega(t-t_0)\big) + N_y \frac{\partial^2 w(x,y)}{\partial y^2} \sin\big(\omega(t-t_0)\big)$$

$$D\nabla^4 w - \mathrm{N_x} \frac{\partial^2 \mathrm{w}}{\partial x^2} - 2\mathrm{N_{xy}} \frac{\partial^2 \mathrm{w}}{\partial x \partial y} - \mathrm{N_y} \frac{\partial^2 \mathrm{w}}{\partial y^2} - (\mu\omega^2 - \mathrm{K})\mathrm{w} = 0 \quad \text{(A2.20)}$$

A2.5 Boundary Conditions

The development of the boundary conditions of a plate for the cases of a plate freely held and a plate clamped along its periphery is as follows:

Clamped, Fixed, or Built-in Edge. With this type of edge, all edge displacements are zero

$$(w)_{y=0} = 0 \tag{A2.21}$$

and the tangent lines on the edge in the x and y directions must be the same as the undeformed plate, namely zero.

$$\left(\frac{\partial w}{\partial y}\right)_{y=0} = 0 \tag{A2.22}$$

Free Edge. A free edge is completely unstressed, therefore a free edge cannot support vertical shearing forces, bending moments, or twisting moments.

$$(M_y)_{y=0} = 0, \quad (M_{xy})_{y=0} = 0, \quad (Q_y)_{y=0} = 0$$

Kirchoff showed that only two conditions were necessary and that the above three conditions could be expressed as two conditions.

$$(M_y)_{y=0} = 0 \implies \left(\frac{\partial^2 w}{\partial y^2} + \nu \frac{\partial^2 w}{\partial x^2}\right)_{y=0} = 0 \tag{A2.23}$$

$$(V_y)_{y=0} = \left(Q_y + \frac{\partial M_{xy}}{\partial x}\right)_{y=0} = 0 \implies \left(\frac{\partial^3 w}{\partial y^3} + (2-\nu)\frac{\partial^3 w}{\partial x^2 \partial y}\right)_{y=0} = 0 \tag{A2.24}$$

Symmetric/Sliding Edge. A symmetric edge is free to move in the vertical and tangential direction but cannot move in the normal direction. Since the edge is symmetric all displacements must be the same on both sides of the boundary. This can be expressed as:

$$\left(\frac{\partial w}{\partial n}\right)_{n=0} = 0 \tag{A2.25}$$

This edge also cannot support any moment that would cause displacement of the edge in the normal direction or any shear because shear is not symmetric.

$$V_n = \left(Q_n + \frac{\partial M_{nt}}{\partial t}\right)_{n=0} = 0 \implies \left(\frac{\partial^3 w}{\partial n^3} + (2-\nu)\frac{\partial^3 w}{\partial n \partial t^2}\right)_{n=0} = 0 \tag{A2.26}$$

Appendix A3
Matlab Code

```
%=========================================================================
%-----------    Analytical Hexagonal Plate Vibration    -------------------
%
%   This program uses the equation discussed in the paper "Stabilitat und
% Eigenschwingungen einer Platte von der Form eines regelmaBigen Polygons"
% to solve for the vibrational displacements w(x,y,f).

clear, clc

%---------------
% input
%---------------
data = csvread('triangle nodes.csv');
    %node locations
x = data(:,1);
y = data(:,2);
%figure,plot(x,y,'.')

h = 4*0.0254;               %(m)
a = h/tand(60);             %(m)
    %length of the side of the hexagon
r = (h/2)/sind(60);         %(m)
t = 3/4*0.0254;             %(m)
    %thickness of the plate
rho = 3058.4;               %(kg/m^3)
    %density of SiC
mu = rho*t;                 %(kg/m^2)
    %area density of the plate
E = 428.28e9;               %(Pa)
    %Young's modulus of SiC
nu = 0.166;
    %Poison's ratio of SiC
K = E;                      %(Pa)
    %This is the Winkler stiffness applied to the face of the plate
    %A decent approximation for this force in this problem is the elastic
    %stiffness of the carbon fiber/epoxy layer
N = E;
    %This is the clamping pressure applied to the sides of the plate
    %A decent approximation for this pressure in this problem is the
    %elastic stiffness of the carbon fiber/epoxy spacers
D = E*t^3/(12*(1-nu^2));
    %the bending stiffness

%f = 6.961/(2*pi*a^2*sqrt(mu/D));
%f = 182665.347;
    %Frequency of vibration

BC = 1;
    %BC = 0 if Kaczkowski's free BC's are used
    %BC = 1 if Kaczkowski's fixed BC's are used
```

```
    %BC = 2 if the boundary is free
    %BC = 3 if the boundary is fixed

%%
%---------------
% calculations
%---------------
if (BC == 0 || BC == 2)
    K = 0;  N = 0;
        %completely free plate
elseif (BC == 1 || BC == 3)
    K = 0;
        %fixed BC's but no force on the plate face
end

omega = 2*pi*f;
Lambda = N*a^2/(2*pi^2*D);
Omega = (mu*omega.^2-K)*a^4/(pi^4*D);
m = [1];
    %index
xi = x/a;   eta = y/a;
Phi = Lambda-sqrt(Lambda^2+Omega);
Psi = Lambda+sqrt(Lambda^2+Omega);
phi_m = sqrt(1-Phi./m.^2);    psi_m = sqrt(1-Psi./m.^2);

%%
%---------------
%BC coeffs
%---------------
beta = 0.866;
c=2*sqrt((a/2)^2+(beta*a)^2);
t = 0:0.001:c;
for j = 1:size(m,2)
    ch_phi = cosh((m(j)*pi*phi_m(j)*2*beta*t)/c);
    sh_phi = sinh((m(j)*pi*phi_m(j)*2*beta*t)/c);
    ch_psi = cosh((m(j)*pi*psi_m(j)*2*beta*t)/c);
    sh_psi = sinh((m(j)*pi*psi_m(j)*2*beta*t)/c);
    S = sin((m(j)*pi*t)/c);
    C = cos((m(j)*pi*t)/c);
    a31 = phi_m(j)*sh_phi.*S-2*beta*ch_phi.*C;
    a32 = phi_m(j)*ch_phi.*S-2*beta*sh_phi.*C;
    a33 = psi_m(j)*sh_psi.*S-2*beta*ch_psi.*C;
    a34 = psi_m(j)*ch_psi.*S-2*beta*sh_psi.*C;
    a41 = (phi_m(j)^3-
3*phi_m(j)*(2*beta)^2)*sh_phi.*S+((2*beta)^3+3*phi_m(j)^2*2*beta)*ch_phi.*C;
    a42 = (phi_m(j)^3-
3*phi_m(j)*(2*beta)^2)*ch_phi.*S+((2*beta)^3+3*phi_m(j)^2*2*beta)*sh_phi.*C;
    a43 = (psi_m(j)^3-
3*psi_m(j)*(2*beta)^2)*sh_psi.*S+((2*beta)^3+3*psi_m(j)^2*2*beta)*ch_psi.*C;
    a44 = (psi_m(j)^3-
3*psi_m(j)*(2*beta)^2)*ch_psi.*S+((2*beta)^3+3*psi_m(j)^2*2*beta)*sh_psi.*C;

    if BC == 0
        for i = 1:size(t,2)
            coefA = [1 0 0 0;
```

```
                0 0 1 0;
                m(j)*a31(i) m(j)*a32(i) m(j)*a33(i) m(j)*a34(i);
                m(j)*Phi*a31(i) m(j)*Phi*a32(i) m(j)*Psi*a33(i)
m(j)*Psi*a34(i)];
            det(coefA);

            [D,S,V] = svd(coefA);
            coef_svd = V(:,size(coefA,2));
            a_m_svd(i) = coef_svd(1);
            b_m_svd(i) = coef_svd(2);
            c_m_svd(i) = coef_svd(3);
            d_m_svd(i) = coef_svd(4);
                %these coefficients are functions of the edge coordinate t
            if coefA*coef_svd == zeros(4,1)
                A_m(j) = a_m_svd(i);
                B_m(j) = b_m_svd(i);
                C_m(j) = c_m_svd(i);
                D_m(j) = d_m_svd(i);
            end
        end
        firstline = '{\bf Non-constant Coefficients for m=}';
        secondline = '{\bf Kaczkowski Free BC}';
        thirdline = '{\bf Using Singular Value Decomposition}';
        figure, plot(t,a_m_svd, t,b_m_svd, t,c_m_svd, t,d_m_svd)
            title({[firstline,num2str(m(j))];secondline;thirdline})
            xlabel('{\bf Edge length (m)}'),ylabel('{\bf Coefficient
value}')
            legend('{\bf A_m}','{\bf B_m}','{\bf C_m}','{\bf D_m}')

        %    A_m = 0;
        %    B_m = 1;
        %    C_m = 0;
        %    D_m = -phi_m./psi_m;
    elseif BC == 1
        for i = 1:size(t,2)
            coefA = [1 0 1 0;
               0 phi_m(j) 0 psi_m(j);
               m(j)*a31(i) m(j)*a32(i) m(j)*a33(i) m(j)*a34(i);
               Phi*a31(i) Phi*a32(i) Psi*a33(i) Psi*a34(i)];
           det(coefA)

            [D,S,V] = svd(coefA);
            coef_svd = V(:,size(coefA,2));
            a_m_svd(i) = coef_svd(1);
            b_m_svd(i) = coef_svd(2);
            c_m_svd(i) = coef_svd(3);
            d_m_svd(i) = coef_svd(4);
                %these coefficients are functions of the edge coordinate t
            %if coefA*coef_svd == zeros(4,1)
                A_m(j) = a_m_svd(1);
                B_m(j) = b_m_svd(1);
                C_m(j) = c_m_svd(1);
                D_m(j) = d_m_svd(1);
            %end
        end
```

```
        firstline = '{\bf Non-constant Coefficients for m=}';
        secondline = '{\bf Kaczkowski Fixed BC}';
        thirdline = '{\bf Using Singular Value Decomposition}';
        figure, plot(t,a_m_svd, t,b_m_svd, t,c_m_svd, t,d_m_svd)
            title({[firstline,num2str(m(j))];secondline;thirdline})
            xlabel('{\bf Edge length (m)}'),ylabel('{\bf Coefficient
value}')
            legend('{\bf A_m}','{\bf B_m}','{\bf C_m}','{\bf D_m}')

        %    a_m = 1;
        %    b_m = 1;
        %    c_m = -a_m;
        %    d_m = -phi_m./psi_m;
    elseif BC == 2
        for i = 1:size(t,2)
            coefA = [phi_m(j)^2-nu 0 psi_m(j)^2-nu 0;
                0 phi_m(j)^3-(2-nu)*phi_m(j) 0 psi_m(j)^3-(2-nu)*psi_m(j);
                a31(i) a32(i) a33(i) a34(i);
                a41(i) a42(i) a43(i) a44(i)];

            [D,S,V] = svd(coefA,0);
            coef_svd = V(:,size(coefA,2));
            a_m_svd(i) = coef_svd(1);
            b_m_svd(i) = coef_svd(2);
            c_m_svd(i) = coef_svd(3);
            d_m_svd(i) = coef_svd(4);
                %these coefficients are functions of the edge coordinate t
        %if coefA*coef_svd == zeros(4,1)
            A_m(j) = a_m_svd(1);
            B_m(j) = b_m_svd(1);
            C_m(j) = c_m_svd(1);
            D_m(j) = d_m_svd(1);
        %end

        end
        firstline = '{\bf Non-constant Coefficients for m=}';
        secondline = '{\bf RAL Free BC}';
        thirdline = '{\bf Using Singular Value Decomposition}';
        figure, plot(t,a_m_svd, t,b_m_svd, t,c_m_svd, t,d_m_svd)
            title({[firstline,num2str(m(j))];secondline;thirdline})
            xlabel('{\bf Edge length (m)}'),ylabel('{\bf Coefficient
value}')
            legend('{\bf A_m}','{\bf B_m}','{\bf C_m}','{\bf D_m}')

    elseif BC == 3
        for i = 1:size(t,2)
            coefA = [1 0 1 0;
                0 phi_m(j) 0 psi_m(j);
                a31(i) a32(i) a33(i) a34(i);
                a41(i) a42(i) a43(i) a44(i)];

            [D,S,V] = svd(coefA,0);
            coef_svd = V(:,size(coefA,2));
            a_m_svd(i) = coef_svd(1);
            b_m_svd(i) = coef_svd(2);
```

```
            c_m_svd(i) = coef_svd(3);
            d_m_svd(i) = coef_svd(4);
                %these coefficients are functions of the edge coordinate t
            %if coefA*coef_svd == zeros(4,1)
                A_m(j) = a_m_svd(1);
                B_m(j) = b_m_svd(1);
                C_m(j) = c_m_svd(1);
                D_m(j) = d_m_svd(1);
            %end
        end
        firstline = '{\bf Non-constant Coefficients for m=}';
        secondline = '{\bf RAL Fixed BC}';
        thirdline = '{\bf Using Singular Value Decomposition}';
        figure, plot(t,a_m_svd, t,b_m_svd, t,c_m_svd, t,d_m_svd)
            title({[firstline,num2str(m(j))];secondline;thirdline})
            xlabel('{\bf Edge length (m)}'),ylabel('{\bf Coefficient
value}')
            legend('{\bf A_m}','{\bf B_m}','{\bf C_m}','{\bf D_m}')

    end
end

%%
E_m = 0;    F_m = 1;
    %antisym-sym => E_m=0, F_m=1
    %sym-antisym => E_m=1, F_m=0
    %sym-sym
    %antisym-antisym
%%%
w = 0;
for j = 1:size(m,2)
    w1 = A_m(j)*cosh(m(j)*pi*phi_m(j).*eta);
    w2 = B_m(j)*sinh(m(j)*pi*phi_m(j).*eta);
    w3 = C_m(j)*cosh(m(j)*pi*psi_m(j).*eta);
    w4 = D_m(j)*sinh(m(j)*pi*psi_m(j).*eta);
%%%
    %w1 = A_m(j)*cos(m(j)*pi*phi_m(j).*eta);
    %w2 = B_m(j)*sin(m(j)*pi*phi_m(j).*eta);
    %w3 = C_m(j)*cos(m(j)*pi*psi_m(j).*eta);
    %w4 = D_m(j)*sin(m(j)*pi*psi_m(j).*eta);
    w_i = (w1+w2+w3+w4).*(E_m*cos(m(j)*pi*xi) + F_m*sin(m(j)*pi*xi));
%%%
    w = (w+w_i);
end

%%
%---------------
% results
%---------------
for j = 1:size(f,2)
xlin = linspace(min(x),max(x),100);
ylin = linspace(min(y),max(y),100);
    %Recreates uniformly spaced data
[X,Y] = meshgrid(xlin,ylin);
    %generates uniformly spaced grid
```

```
W = griddata(x,y,w,X,Y,'cubic');
    %interpolate the values of the function at the uniformly spaced points

%figure,surf(X,Y,abs(W)),title('Hexagon Vibration (Triangle portion)')
%    xlabel('x (m)'),ylabel('y (m)'),zlabel('z')
%    shading interp

old = [x,y];
rotate_60 = [cosd(60) sind(60); -sind(60) cosd(60)];
rotate_120 = [cosd(120) sind(120); -sind(120) cosd(120)];
old_rotate_60 = old*rotate_60;
old_rotate_120 = old*rotate_120;
    %rotates [x,y] so the results can be formed into a hexagon

%figure,plot(x,y,'.', a-x,y,'.', x,h-y,'.', a-x,h-y,'.')
%    hold all
%    plot(a+old_rotate_60(:,1),old_rotate_60(:,2),'.',
a+old_rotate_60(:,1),h-old_rotate_60(:,2),'.')
%    plot(r+(a/2)+old_rotate_120(:,1),(h/2)+old_rotate_120(:,2),'.',
r+(a/2)+old_rotate_120(:,1),(h/2)-old_rotate_120(:,2),'.')
%    plot(-old_rotate_60(:,1),old_rotate_60(:,2),'.', -old_rotate_60(:,1),h-
old_rotate_60(:,2),'.')
%    plot(-(a/2)-old_rotate_120(:,1),(h/2)+old_rotate_120(:,2),'.', -(a/2)-
old_rotate_120(:,1),(h/2)-old_rotate_120(:,2),'.')
%    grid on
%    hold off
    %plot the rotated matrices

xlin60 = linspace(min(old_rotate_60(:,1)),max(old_rotate_60(:,1)),100);
ylin60 = linspace(min(old_rotate_60(:,2)),max(old_rotate_60(:,2)),100);
xlin120 = linspace(min(old_rotate_120(:,1)),max(old_rotate_120(:,1)),100);
ylin120 = linspace(min(old_rotate_120(:,2)),max(old_rotate_120(:,2)),100);
    %creates uniformly spaced data for the rotated matrices
[X60,Y60] = meshgrid(xlin60,ylin60);
[X120,Y120] = meshgrid(xlin120,ylin120);
    %generates uniformly spaced grid for the rotated matrices
W60 = griddata(old_rotate_60(:,1),old_rotate_60(:,2),w,X60,Y60,'cubic');
W120=griddata(old_rotate_120(:,1),old_rotate_120(:,2),w,X120,Y120,'cubic');
    %interpolate the values of the function at the uniformly spaced points
    %for the rotated matrices

X1 = [X,X;a-X,a-X];
Y1 = [Y,h-Y;Y,h-Y];
W1 = real([W,W;W,W]);
    %form square matrices with reflected triangles for the original data
X2 = [a+X60,a+X60;-X60,-X60];
Y2 = [Y60,h-Y60;Y60,h-Y60];
W2 = real([W60,W60;W60,W60]);
X3 = [r+(a/2)+X120,r+(a/2)+X120;-(a/2)-X120,-(a/2)-X120];
Y3 = [(h/2)+Y120,(h/2)-Y120;(h/2)+Y120,(h/2)-Y120];
W3 = real([W120,W120;W120,W120]);
    %form square matrices with reflected triangles for the rotated data
X4 = [X1,X2;X3,0*X1];
Y4 = [Y1,Y2;Y3,0*Y1];
W4 = [W1,W2;W3,0*W1];
```

```
    %assemble hexagon from reflected triangles

figure,surf(X4,Y4,W4)
    xlabel('{\bf x (m)}'),ylabel('{\bf y (m)}'),zlabel('{\bf z}')
    shading interp
if BC == 0
    title({'{\bf Transverse Hexagon Vibration}';'{\bf Kaczkowski Free
BC}';['{\bf Frequency = }',num2str(f),'{\bf Hz}']})
elseif BC == 1
    title({'{\bf Transverse Hexagon Vibration}';'{\bf Kaczkowski Fixed
BC}';['{\bf Frequency = }',num2str(f),'{\bf Hz}']})
elseif BC == 2
    title({'{\bf Transverse Hexagon Vibration}';'{\bf RAL Free BC}';['{\bf
Frequency = }',num2str(f),'{\bf Hz}']})
elseif BC == 3
    title({'{\bf Transverse Hexagon Vibration}';'{\bf RAL Fixed BC}';['{\bf
Frequency = }',num2str(f),'{\bf Hz}']})
end
end
```